L'Imageur diffractif de Fresnel : Validation le ciel depuis le sol et l'observation spatial pour à Haute Résolution Angulaire

Truswin Raksasataya

Université de Toulouse

THÈSE

En vue de l'obtention du

DOCTORAT DE L'UNIVERSITÉ DE TOULOUSE

Délivré par :
Université Toulouse 3 Paul Sabatier (UT3 Paul Sabatier)

Discipline ou spécialité :

Instrumentation Spatiale

Présentée et soutenue par :
Truswin Raksasataya

le : 20 Decembre 2010

Titre :

Fresnel Diffractive Imagery Arrays : Ground-based validation and space applications

---

JURY

Dr. Christophe Peymirat	Professeur, CESR	President
Dr. Arnaud Liotard	Ingénieur, Thales Alenia Space	Examinateur
Dr. Pierre-Gilles Tizien	Ingénieur, CNES	Examinaeur

Ecole doctorale :
Sciences de l'Univers, de l'Environnement et de l'Espace (SDU2E)

Unité de recherche :
Laboratoire d'astrophysique de Toulouse et Tarbes (LATT)

Directeur(s) de Thèse :

Dr. Laurent Koechlin Astronome,OMP

Rapporteurs :

Dr. Farrok Vakili	Astronome, OCA	Rapporteur
Dr. Roger Ferlet	Astronome, IAP	Rapporteur

‘‘ We are not building an instrument to detect something we know what it looks like, but we are building it to detect something that we never know that it ever exists’’, Space instrumentation

Laurent KOECHLIN

Acknowledgements

Through the years in this thesis, this part is one of the hardest writing parts in my thesis. I do not know how to start writing this. I have learnt many things and done many things, but one certain thing that I surely know is all of this would never be possible, without the support and encouragement of a lot of people.

First, I would like to thank my director-supervisor. For Laurent KOECHLIN, I could not find any words to express how grateful I want to thank you. I owe you more than what I have gain during four years in l'observatoire Midi Pyrénés, . I can still remember what you told me when we first talk about space instruments research. It is now on the first page. You have been my professor, my mentor, my colleague, my friend and a never-ending of moral support and encouragement. You have given yourself so much to help me succeed. If I will have to be a supervisor someday, I wish that I could be a half the advisor that you have been to me.

I would also like to thank the rest of my thesis committee for their support. Roger FERLET and Farrok VAKILI provided me with invaluable advice, comments on my research, and being my rapporter. It is a pleasure to thanks Dr. Christophe Peymirat, who always takes care of me since my study in master for being my president de Jury. I would particularly like also to thank Arnaud Liotard who had taken care of me as my co-supervisor.

I would also like to express my thanks to Ana Ines de Castro, Paul Deba and Denis Serre who are always be a good friends, commentator and colleagues. I particularly show my gratitude to Jean Pierre RIVET, who always be a great host in Nice and for taken care of me and my thesis work.

I would like to thanks everyone in l'observatoire Midi Pyrénés, who always helps me every time that it is needed, particulary Herve Cafantan for giving me advices and my friends in laboratory, who making my life in here feel comfortable.

Here, its all my friends in Toulouse. You make me feel at home and I thank you all for let me enjoy my time here. I have never thought that i will stay here this long. Since I first came to Toulouse, you made me feel comfortable and had a great time.

Finally, I would like to indicate this gratitude to my family, who always understand and support me along this journey.

Remerciements

C'est avec mon mal écriture Francaise mais c'est quand même avec mon enthousiasme le plus sincére, respectif et le plus vif que je voudrais rendre mérite á tous ceux qui m'ont aidé á mener cette thése : J'adresse mes plus vifs remerciements Ĺ mon directeur de thése, Monsieur Laurent KOECHLIN pour avoir accepté de diriger ma thése et pour sa compréhension et son soutien intellectuel et moral ainsi que pour le temps qu'il a consacré aux travaux fastidieux de relecture pendant la période de préparation de cette thése. Je lui suis trés reconnaissant et je le respecte beaucoup pour sa gentillesse, sa grande disponibilité, sa patience, ses conseils courag et et ses altitudes pour travailler en thése et pour ma vie. Ce travaile ne sera pas complete sans lui.

Je tiens aussi á remercier Monsieur le Professeur Christophe PEYMIRAT qui j'ai fait mes études en Master et qui m'a fait l'honneur d'être Président de ce jury. Je tiens également á remercier Monsieur le Professeur Roger FERLET et Monsieur Farroke VALKILI pour avoir accepté d'évaluer mon travail. Je leur adresse toute ma gratitude pour leurs conseils importants et judicieux. Je tiens également á remercier Monsieur Arnaud LIOTARD qu'est ma co-director chez Thales Alenia space.

Je tiens á manifester ma profonde reconnaissance pour la gentillesse que Monsieur Jean-Pierre Rivet m'a accordé pour la correction de ce travail et pour de travail que j'ai fait pendant mes temps en Nice.

Mes remerciements vont aussi á mes amis á l'observatoire Midi Pyrénées. Finalement, je voudrais remercier de tout mon coeur mes parents et mes proches pour leurs encouragements et leur soutien durant mes études en France, sans lesquels je n'aurais pas pu être ici en train d'écrire ces remerciements.

Contents

Présentation générale

Un nouveau concept optique est validé dans cette thèse : l'utilisation d'un Imageur Diffractif de Fresnel comme instrument spatial. Il est basé sur la focalisation diffractive par anneaux de Soret ("Fresnel zone plate"), et particulièrement adapté pour la haute résolution angulaire et la haute dynamique en astrophysique.

La focalization diffractive a été testée dans notre laboratoire en 2007 [Serre D., 2007] par des mesures optiques. Un premier prototype a été construit en 2006 pour tester la focalisation et différentes fonctions dans le domaine visible : à 600 nm de longueur d'onde. Les résultats ont montré qu'il est possible d'utiliser la focalisation diffractive pour former des images à haute résolution et haute dynamique : 10^{-6}.

La prochaine étape a été réalisée lors de cette thèse par la construction du prototype génération II et par son utilisation sur le ciel. Dans ma thèse, je décris comment on a fait la transition entre les prototypes génération I utilisé dans un laboratoire, et génération II, fait pour l'observation du ciel. Vous pourrez trouver décrits dans la suite : la conception, la réalisation, l'intégration et les résultats des observations.

Pour passer des générations I à II, des modifications ont été faites sur deux parties du prototype : les "module grille primaire" et "module récepteur". Pour la grille primaire, le nombre de zones de Fresnel est passé de 116 à 696, et le côté a été agrandi de 80 à 200 mm. Sur cette nouvelle grille primaire, nous avons fait des optimisations afin d'obtenir une plus grande dynamique et plus de transmission (luminosité). La dernière version de la grille a moins de barres de maintien (1 sur 3). Des modifications du module récepteur ont aussi été faites pour s'adapter aux nouvelles caractéristiques de la grille primaire.

Les validations sur le ciel de l'imageur du Fresnel ont porté sur deux points : la haute dynamique et la haute résolution angulaire. Les observations ont été faites à l'observatoire de la Côte D'Azur, de juillet 2009 à mars 2010. Les cibles astrophysiques ont été choisies dans ces deux directions : d'une part pour la haute dynamique, avec des écarts de luminosité entre des étoiles proches, graduellement augmentés pour trouver la limite en dynamique ; d'autre part pour la haute résolution angulaire, sur des cibles de plus en plus serrées, la séparation entre les étoiles a été mesurée. Avec des binaires serrées à grand écart de magnitude, on peut tester à la fois la résolution et la dynamique. De telles cibles sont des étoiles doubles comme Sirius AB, ayant 11 magnitudes d'écart en bande I (centrée sur 800 nm), et une séparation de 8" . Nous avons aussi tenté d'imager Procyon AB, qui est un système binaire de séparation 2" avec 12 magnitudes de différence, mais sans succès. Les mesures sur ces cibles ont permis de préciser la limite en résolution angulaire et dynamique.

Un autre type de cibles que nous avons observées sont des objets du système solaire, entre autres Mars et ses satellites. Ils sont difficiles à détecter car ces satellites sont très petits et leurs orbites sont proches du disque étendu et brillant de la planète.

La validation présentée dans cette thèse montre les performances et les caractéristiques

de l'Imageur du Fresnel. Les résultats obtenus ont permis de savoir comment fonctionne ce type d'instrument dans la réalité en observant directement le ciel, et vont aider à préparer une mission spatiale future.

Part I

General introduction to Fresnel Imager concept

Chapter 1

Introduction

Fresnel Diffractive Imagery Arrays (FDIAs) belong to a new concept of instruments using a diffractive focusing array. FDIAs has advantages in high resolution and high dynamic range in space observation.(Koechlin L., Serre D., et al, 2005)[10]

To develop Fresnel Diffractive Imagery Arrays for space applications after laboratory conception in 2007 (Serre D., 2007) [3], ground-based validations are pursued to verify and demonstrate the concepts, performance, characteristics and functions of the instrument for sky observation.

Before it is launched to operate in space, the Fresnel imagery has to be carefully studied and tested in all the aspects that can be tested test on Earth, in order to guarantee the functions and results in space operation. This thesis contains the studies of Fresnel Diffractive Arrays prototype generation II, ground-based validation for sky observation and some parts of this thesis are prepared for future space missions.

In the last part, I will conclude by assessing the result and the performance based on ground-based observation. This will allow us to predict the instrument's behaviour in space conditions.

I will also describe the modules and the functions that have been studied and prepared for ground validation since the summer of 2009. I describe the conception of optics, propagation simulation, integration, optimization and results. This thesis refers and links to other articles of Laurent Koechlin, Denis Serre and Paul Deba. It includes some material from collaborations with CNES and NUVA (Network for ultra-Violet Astronomy).

1.1 Why a Fresnel Imager ?

The Fresnel Diffractive Imager is an instrument with a new focussing concept for future space observation. Since Fresnel diffractive arrays are made of thin foil, this quasi-weightless focussing instrument can be built in meters large dimensions. The larger aperture means the better angular resolution, and more deep sky objects. Therefore, Fresnel imager is proposed as an alternative for future space observation missions.

This concept of diffractive focussing has been applied in optics; but diffractive focussing with arrays for space application is a new concept. Then, this is a pioneer for the next generation of diffractive focussing instruments.

1.1.1 How it helps science

This thesis presents some of the first results of a Fresnel diffractive array Imager for astrophysics. It demonstrates the conditions and functions of the instrument for sky observation.

With larger size of arrays up to 20-m in UV or 30-meter in the visible, it can resolve deep sky objects at respectively 1.5 to 3.5 mas resolution, see chapter 6. This is expected to have an impact on discoveries made with direct imaging in space.

1.1.2 How the Fresnel imager compares with other focussing devices

Fresnel Imaging systems can be compared to other telescopes for angular resolution. Our 200 mm aperture Fresnel imager is equal to classical telescopes having the same aperture. However, the weight of 200 mm Fresnel array itself is only a few grams.

Another benefit of Fresnel Imaging system is high dynamic range imaging. The dynamic range has reached $10^{-}8$ in numerical simulations (no air turbulence). With our prototypes of 80 mm and 200 mm, it has reached 10^{-6} in laboratory on artificial sources, and 2.5 10^{-6} on the sky.

From the above comparisons, the Fresnel imager can be seen as a lightweight optical instrument which, when it is used at large aperture, will provide a high angular resolution and high dynamic range.

1.1.3 The difficulties encountered, and resolved, in this thesis work

The difficulties that I have encountered concern the character and peculiar behavior of this instrument, and the observation of the astrophysical targets. Since Fresnel imaging involves a new concept of astrophysical instrument: it is the first Fresnel focussing instrument used for such sky observation, many problems have had to be detected, understood, and resolved. Some examples are: the alinements, being given the long focal length of the prototype (18 meters), the residual aberrations (coma) of the chromatic correction blazed Fresnel lens, the underestimated stiffness requirement of the mechanical structure (not only the 18m telescope tube, but also the 2m optical rail of the receptor module).

1.2 Principle of light focalisation

Focalisation converts incoming light from a plane wave to a focal point. It is required to construct images. Focalisation of light usually means refraction by an optical lens or reflection by a concave mirror.

1.2.1 Principle of refraction

Focalization by refraction is a classical method using an optical element, such as a lens, to focus light onto a focal plane. Light travels as a plane wave before reaching the medium. The curved surface refracts light into a convergent wavefront. Figure 1.1 shows the wavefront travelling through an optical lens and converging to a focal point. (Perez J. P., 2004)[14] Refraction is used in many imaging systems.

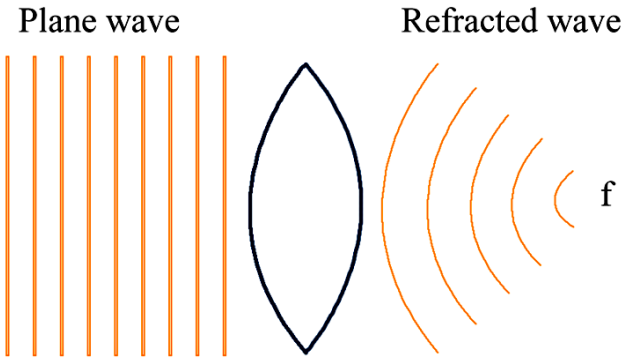

Figure 1.1: Focalization by refraction on a curved surface optics changes a plane wave into a spherical wave to form an image at the focal point.

1.2.2 Principle of diffraction.

Diffraction in light waves was discovered by Huygen in 1678 and developed further by Augusten Fresnel in 1829. Diffraction occurs when light wave is limited in cross-section by a diaphragm.

Diffraction patterns are controlled by the dimensions and the shape of the aperture. For example, the diffraction pattern of a circular aperture is shown in figure 1.3 and that of a rectangular aperture is shown in figure 1.4. Figure 1.2 describes the basic experiment where diffracted waves are created by a double slits aperture. In all the above cases, the amplitude of the light wave is added in in-phase positions and cancelled out in out-phase positions. (Perez J. P., 2004)[14]

1.3 Fresnel diffractive focalisation

In the Fresnel Imager arrays, diffraction is used to focus light. When light propagates from a distant source through Fresnel arrays, it passes through the open parts of a given Fresnel arrays zone and diffracts, but it is blocked by the opaque parts of the same zone. Figure 1.5 shows how light travels through the open parts of a Fresnel zone and then to focal point. The electric field (amplitude) in a light wave can be described as

$$E = A\exp(i\omega t - kx) \tag{1.1}$$

while $k = 2\pi/\lambda$

From figure 1.5, we define the wave emerging from the opened part of the first zone as E_1, and E_2 from the second zone and etc. Thus there is an optical path difference of λ between two different apertures in consecutive zones. An optical path difference of λ corresponds to phase shift of 2π. The phase shift allows diffracted light to be coherently added at the focal point. The total electric field at the focal point is a sum of diffracted wave from each Fresnel zones. Thus, we can rewrite the output wave as

$$E_f = \sum E_k \tag{1.2}$$

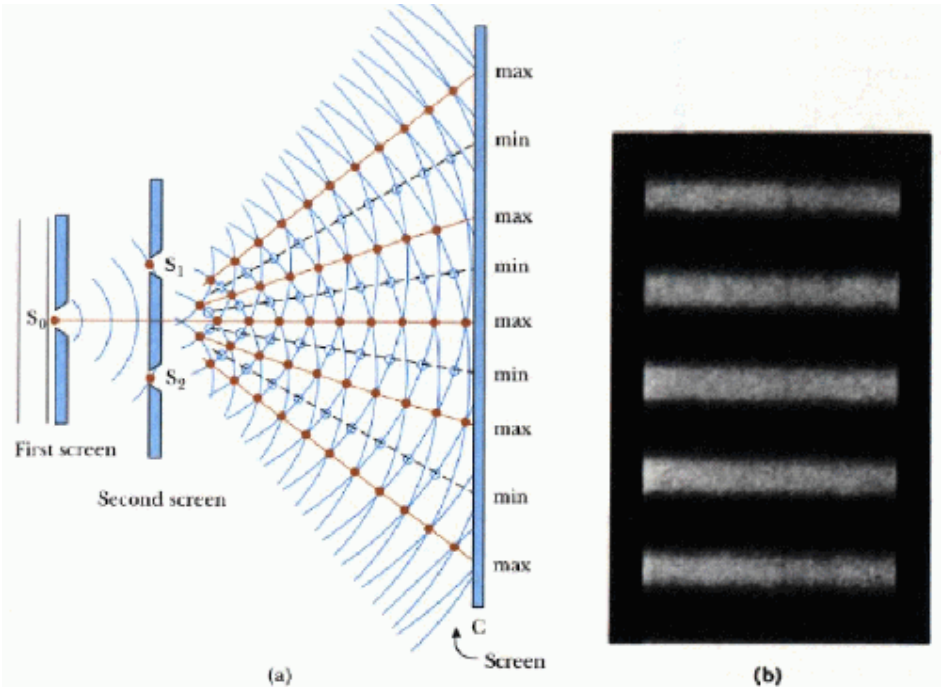

Figure 1.2:
Diffraction of wave by a double slit: first experiment by Thomas Young in the early 1800s. The red nodes and lines represent amplitude of in-phase position from a secondary wavelet and the blank blue anti-nodes represent the out-phase position, where the waves cancel each other out.

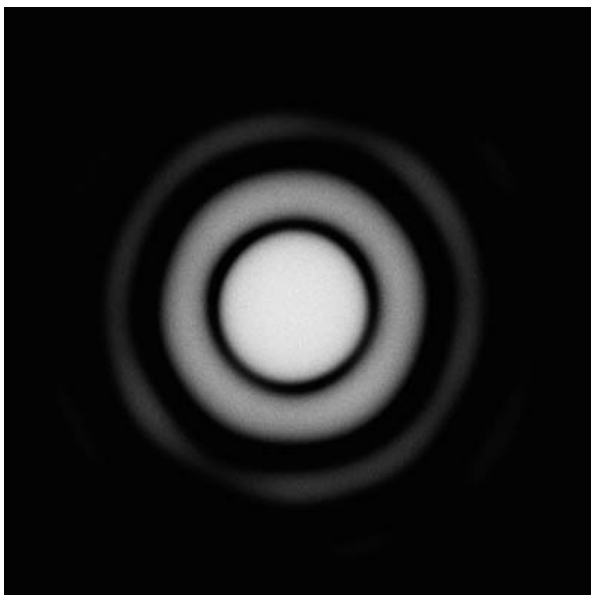

Figure 1.3: Diffraction pattern from a circular aperture

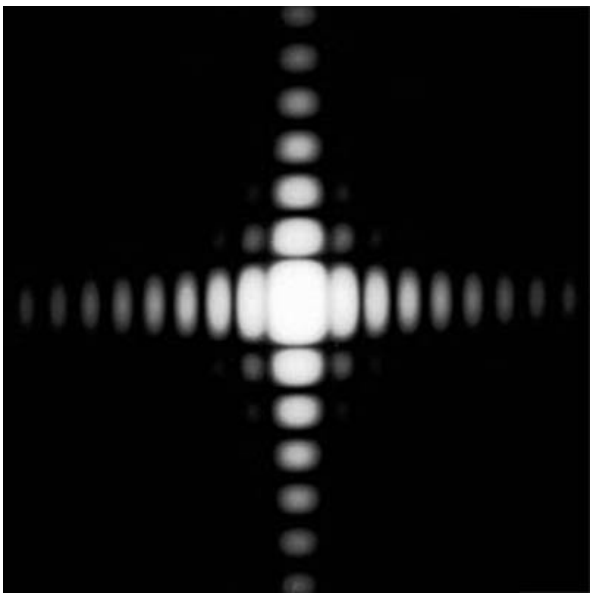

Figure 1.4: Diffraction pattern from a rectangular aperture.

where

$$E_1 = A\exp(i(\omega t - \frac{2\pi x}{\lambda})) \tag{1.3}$$

$$E_k = A\exp(i(\omega t - \frac{2\pi x}{\lambda} + 2\pi(k-1))) \tag{1.4}$$

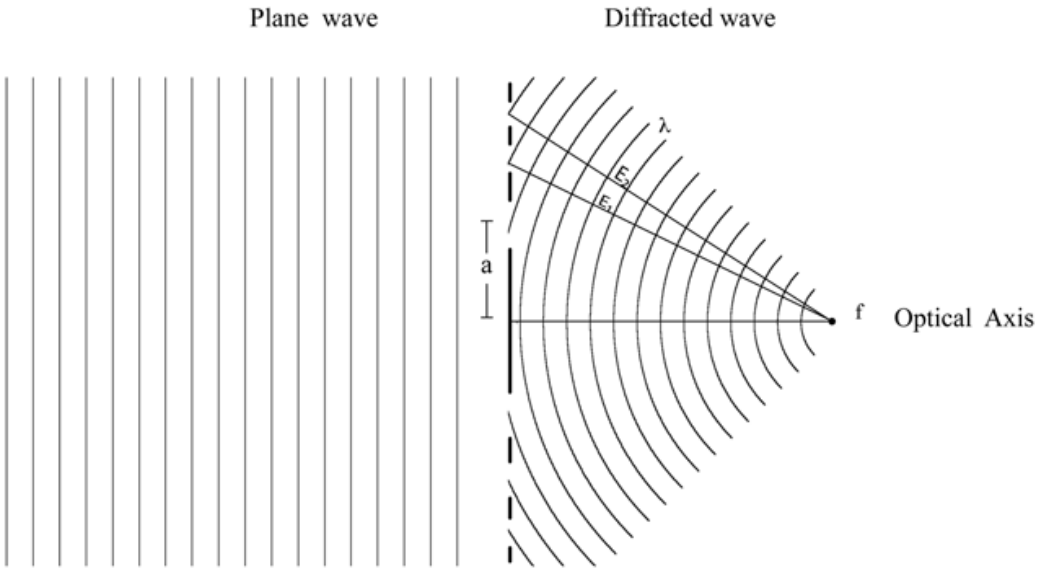

Figure 1.5: A plane wave propagates through the apertures in Fresnel zones. The optical paths (E_1 and E_2) difference between two Fresnel zones is λ. The diffracted light by arrays aperture converges to a focal point (f)

This concept has been applied since 1875 as a Soret or Fresnel zone plate (FZP)(Soret J. L., 1875)[22]. It is used in the optical domain as a focusing device, which is shown in fig 1.6. Today, FZP is used in a number of applications such as antenna design for millimetre waves (Minin I.V. and Minin I.O., 2000)[12].

In classic implementation, a Fresnel zone plate in optics is built the following way: its opaque regions are made from dark material covering the surface of transparent supports. This means drawing the Fresnel zones on the optical surface according to the position of Fresnel zones. The following relation yields to the Fresnel zone radii (a).

$$a^2 + f^2 = (f + k\lambda)^2 \tag{1.5}$$

$$a^2 = 2k\lambda f + (k\lambda)^2 \tag{1.6}$$

where a is the distance of a Fresnel zone from the associated optical axis to determine the radius "a" of the Frensel zone index k in the array.

if $k\lambda \ll f$, then we can write equation 1.6 as

$$a \simeq \sqrt{2k\lambda f} \tag{1.7}$$

where

f = focal length
k = Fresnel index zone
λ = wavelength

From eq.1.7, we have two associated parameters; central wavelength and focal distance, which allows us to determine Fresnel zones radii on the FZP.

1.4 Fresnel array design

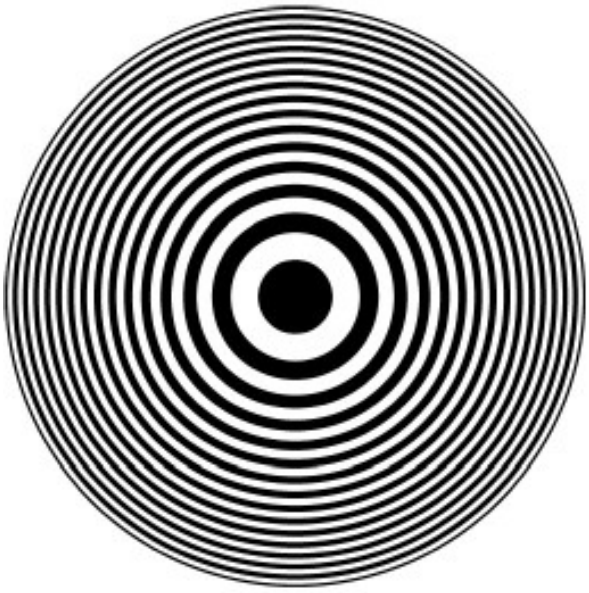

Figure 1.6: Circular geometry form of array (original Fresnel Zone Plate in 1875)(Soret, 1875)[22].

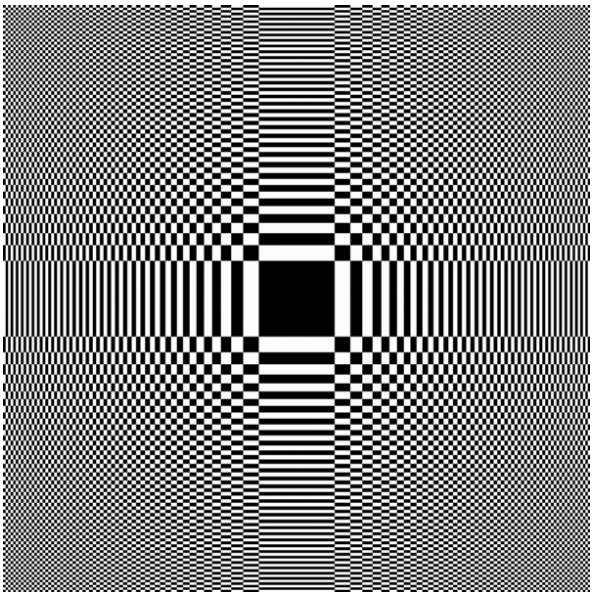

Figure 1.7: Orthogonal geometry form of arrays, by Laurent Koechlin et al., developing Fresnel array in orthogonal geometric form from Soret's Fresnel zone plate in 2005.

The concept of Fresnel arrays , developed by Laurent Koechlin, Denis Serre and Paul Duchon in 2005, is a transformation of Fresnel zone plates from circular geometry to an orthogonal geometry.(Koechlin L. Serre D., Duchon P.)[10]

The orthogonal geometry in Fresnel arrays design supports a rigid mechanical structure of array and reinforces it. Another advantage, which is most useful in space, is the use of void subapertures. This void aperture layout in geometrical arrays is made by using orthogonal bars to maintain Fresnel zones structure and to define the opened aperture at the same time. As a result, there is no optical material in transparent zones.

In space applications, this void subaperture will permit light to pass through the Fresnel arrays , diffract and converge to a focal point without being affected spectrally nor by phase aberration. These advantages mean less weight and a lower cost in building large apertures for space-borne observations in the future.

Fresnel arrays are described by a transmission function having "1" or "0" value respectively for a void aperture and opaque area. Equation 1.8 is a transmission function of a Fresnel array as a function of a: the position of the optical axis at the center.

$$
\begin{aligned}
&g(a) = 1 \\
&\qquad \text{if} \quad \sqrt{a^2 + f^2} \in [(k + \tfrac{f}{m\lambda} + \tfrac{1}{4})m\lambda; (k + \tfrac{f}{m\lambda} + \tfrac{3}{4})m\lambda\,[\\
&g(a) = 0 \qquad \text{otherwise} \\
&\qquad h(a) = 1 - g(a)
\end{aligned}
\tag{1.8}
$$

where

f = focal distance of Fresnel array
k = Fresnel zones index
λ = central wavelength
m = diffraction order; in this case, $m = 1$

To transform the circular Fresnel zone plate into orthogonal form, a transmission law $T(x, y)$ of 2D arrays has been developed from g and h functions as :

$$
\begin{aligned}
T_c(x, y) &= h(x)g(y) + g(x)h(y) \\
T_o(x, y) &= h(x)h(y) + g(x)g(y)
\end{aligned}
\tag{1.9}
$$

where x and y are orthogonal;

T_c and T_o yield similar arrays in phase opposition (Koechlin L. Serre D., Duchon P.)[10]. One can choose one of these functions to determine the opaque and void areas on Fresnel arrays. We use diffraction at order one, which means that we use the wave front that is obtained by a wavelength shift from a given zone to the next. Figure 1.6 and 1.7 shows the circular and orthogonal geometries.

1.5 Fresnel Imaging System

Fresnel Imaging System (FIS) is the actual implementation of the concept either in space or as a ground-based prototype. It is different to other classical Image Systems since it uses diffractive focussing, which is created by thousands of subapertures. An orthogonal geometry array creates a highly confined central lobe in the Point-Spread-Function (PSF): there are a central lobe and four spikes see in figure 1.8. The spikes limit four quadrants in the image field, in which there is a very low background level.

Figure 1.8 shows the circular and orthogonal comparative design. The orthogonal and circular geometry have the same opaque and void parts with respect to Fresnel zone index.

1.5.1 Fresnel Modules

The Fresnel Imaging System (FIS) is the addition of two main modules that are required to perform the vital tasks of collecting light, focusing light, correcting chromatism and constructing images. The two main modules are classified as : Fresnel arrays module or Primary module, and Fresnel receptor module or secondary module shown in figure 1.9.

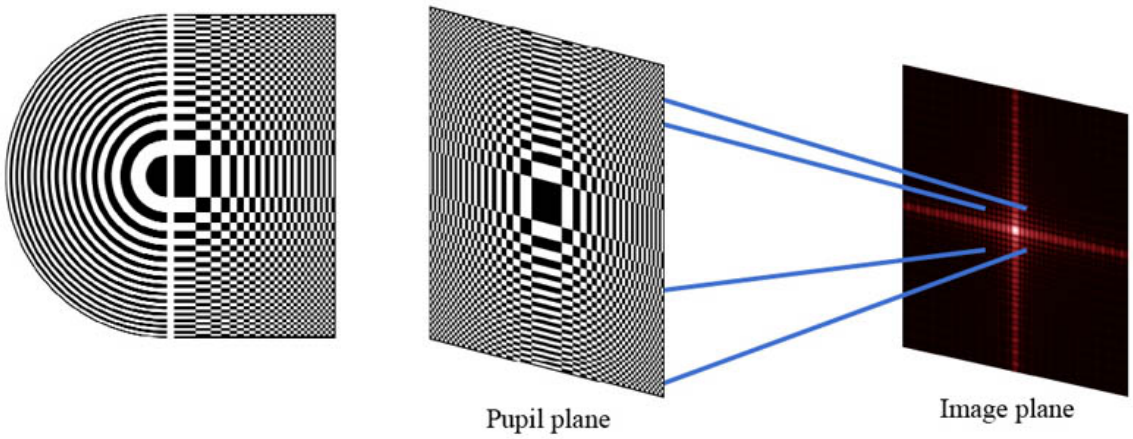

Figure 1.8: Left : circular-othogonal comparative designs, Right : The image given from a point source, Point-Spread-Function (PSF)

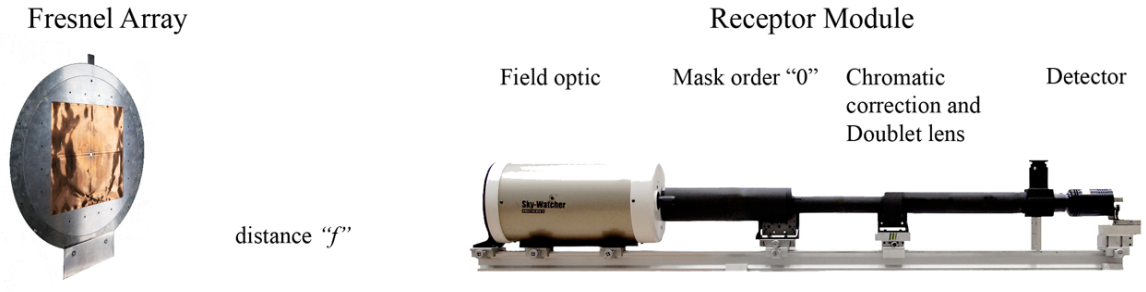

Figure 1.9: Fresnel Imager System contains Fresnel Array module and Receptor module.

Fresnel Primary module.

The primary module contains the Fresnel array and acts as a diffractor. It focuses light onto the receptor module. The primary module is defined by parameters such as dimension, number of zones and pattern of Fresnel array, that impose the value of parameters to the secondary module such as its position and internal design.

Fresnel Secondary module

The secondary module or receptor module is a collector and correction module, which is placed at the focal plane; for instance, 18 m downstream in prototype generation II as shown in figure 1.9. The focal plane position, at the distance "f" between the modules, is defined by the chosen observation wavelength and other relevant parameters.

Field optics presented as a Maksutov telescope in figure 1.9, collects light from primary array, which is placed in the image plane: distance "f" from the main aperture plane. Light travelling through field optics is focused onto a pupil plane. The field optics conjugates the main array and the pupil plane.

Order "0" mask is used in order to minimise parasite light from the main array that would come from diffraction orders different from “+1”. A mask is placed on the focal plane of the field optics. This mask will enhance the contrast by blocking the light from order "0" of the primary array, which is a parallel beam focused by the field optics.

Chromatic Correction lens (Blazed Fresnel lens at order -1) reorders diffracted light from order “1” of the main array. This results in the equivalent of an order “0”, which we call “+1, -1”(Serre D., 2007)[3] . The beam is now achromatic but no longer convergent. However, the beam has beem compressed, so small optics can be used downstream.

Doublet lens is placed next to the blazed lens to converge wave order “ $+1, -1''$ to the final image plane. It has a focal length of 350 mm, that focuses the light and creates the final image onto a detector.

1.6 Optical parameters

This section will introduce parameters that are necessary to determine the Fresnel Imaging system specifications. As a Fresnel Imager system has a wide a range of parameters, some of them must be defined as initial conditions.

1.6.1 Focal length

The focal length (f) of the primary array is determinant to position the secondary module with respect to the primary module (Serre D. 2007)[20], (D. Serre, P. Deba, and L. Koechlin)[19]. It can be expressed as follows:

$$f = \frac{C^2}{8\lambda k_{max}} \tag{1.10}$$

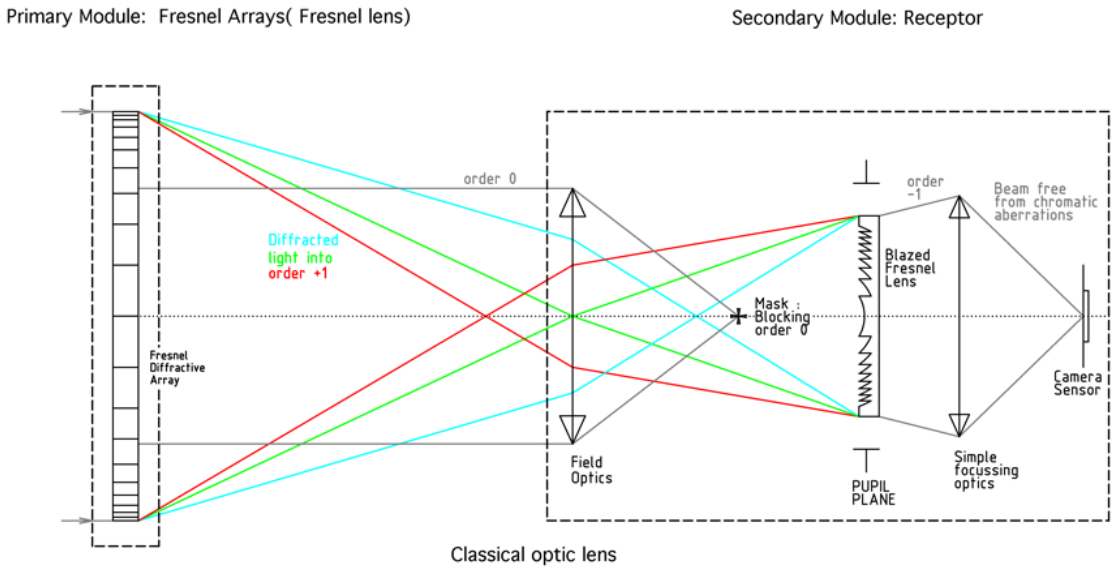

Figure 1.10: Fresnel image system diagram by Paul Deba, describing the primary module as a Fresnel array container collecting and focusing light to the secondary module for chromatic correction and image formation.

where

$$\begin{aligned} C &= \text{diameter of the Fresnel array} \\ k_{max} &= \text{total number of zones in the Fresnel array} \end{aligned}$$

In the study of prototype generation II, we chose the focal length: 18 m as there is an existent refractor tube to support it. The wavelength of 800nm was selected due to optimal observation conditions at this wavelength. The last parameter, k_{max} is limited by the smallest current engraving technology. As a consequence of these constraints, the square section of the primary modules is set at 200 mm.

1.6.2 Wavelength domain limitation

The wavelength domain is limited by the diameter of the field optics in secondary modules. Wavelength domain is described as $\Delta\lambda$:

$$\frac{\Delta\lambda}{\lambda} = \sqrt{2}\frac{D}{C} \tag{1.11}$$

Field optics (of diameter D), which is a classical optical system, is placed at the focal plane of primary array in order to receive a focused image.

1.6.3 Angular resolution

The angular resolution R of a Fresnel imager can be high, depending upon wavelength and the size of the main array: it behaves like a classical square aperture of the same size.

$$R = \frac{\lambda}{C} \tag{1.12}$$

With a 200 mm aperture and an 800 nm wavelength, the angular resolution defined in 1.12 equals 0.8 arcsec. In a nominal space mission, we definitely have a larger aperture (meter size), and consequently a higher angular resolution. Other parameters associated with Fresnel optics have been described in other publications. (Serre D., 2007)[21] (Serre D. et al,2007)[18].

Chapter 2

Photometry and high dynamic range.

This section will describe how photons behave when they travel from the light source to the final image plane in the Fresnel Imaging system(FIS). We assume that the light emitted from the source follows the black body spectrum. Calculation of light transmission through the instrument is made to assess FIS performances.

In an ideal instrument, light would travel through the optical elements with perfect transmission. This means there is no absorption, unwanted reflection, diffusion etc. In a practical optic system, not all photons are transmitted through the device. Physical phenomena such as absorption, diffraction etc., occur in the instruments, due to the medium and imperfect optics. Our study on Fresnel photometry will assess the instrument's limitations, and calculate realistic targets for space as well as ground-based testing. The computed number of photons, which reach the detector to construct the image in a Fresnel system, drives the signal-to-noise ratio that indicates image quality.

2.1 Luminosity and limiting magnitude

To determine the number of photons reaching a detector, it is necessary to know the number of photons coming from the light source, and the global efficiency of the Fresnel optical system.

Terms that will be mentioned in this section are brightness and luminosity. These parameters determine the energy that the source emits towards the observer.

Luminosity is a quantity of energy that an object radiates per unit of time (Watt). For example, the luminosity of the sun is 3.846×10^{26} Watt. Assuming a given wavelength, luminosity is also related to a number of photons emitted per second. In the following, we will refer to brightness: the power received per unit surface (W/m^2). For example, the sun delivers a brightness of 1000 W/m^2 at ground level.

$$B = \frac{L_S}{4\pi d_s^2} \tag{2.1}$$

where

B = brightness $[W/m^2]$ of an object at distance d_s
L_s = luminosity radiating from the object
d_s = distance from the object to the observer

The brightness can also be expressed in terms of apparent magnitude: in astrophysical usages, physicists use magnitude to describe the brightness of a star.

$$m_a = -2.5 \log \frac{B}{B_v} \tag{2.2}$$

where

m_a = magnitude of stars
B = brightness of stars,
B_v = brightness of Vega.

For instance, the sun has its magnitude of -27.
We can obtain the relation between energy and brightness using this equation:

$$E_{total} = B \times t \times S \tag{2.3}$$

where

t = exposure time,
S = aperture area.

2.2 Energy and photons

It is important to understand the concept of energy and how it is treated in optical systems. The brightness arriving at the front-end of an optical system is determined by the distance of the light source and its brightness as stated in equation 2.1. Now, we determine the number of photons that are coming into the system for a given wavelength. From the Plank relation, we have the energy of a photon,E_p:

$$E_p = \frac{hc}{\lambda} \tag{2.4}$$

where

h = Planck's Constant ; 6.6261×10^{-34} Js
c = speed of light; 299792458 m s^{-1}
λ = wavelength

A given waveband contains different λ. Here, to determine the number of photons, we consider a limited bandwidth centered around λ and we make the approximation that λ is constant.

Equation 2.4 can be used to determine the number of photons at a certain wavelength. We can determine the number of photons (N_p) by:

$$N_p = \frac{E_{total}}{E_p} \tag{2.5}$$

The number of photon from equation 2.5 is calculated at the entrance of the instrument.

2.3 Transmission efficiency of the optical system

This process is meant to assess the efficiency of the optical system. Transmission efficiency will determine the number of photons that reach the image compared to the number which is at the entrance.

Absorption, diffusion etc. reduce the number of photons and cause degradation of signal-to-noise ratio. In a Fresnel diffractive array, the transmission can be expressed in two parts, primary and secondary modules. The rate of transmission depends on the performance of these two modules.

In the primary module, the transmission is related to the designed layout of the Fresnel array. The original Fresnel zone plate splits the incoming light wave into several beams, the different diffraction orders [0, +1, -1, +2, -2...+n, -n]. The void and opaque parts in each zone respectively block or transmit the incoming wave. In figure 2.2, the opaque area on array surface has blocked the light, which would have been in phase in phase opposition at the focal point for order different than zero. The maximum focused light into order "1 " of a Fresnel array is about 10% of transmission efficiency.

In the receptor module, the efficiency of transmission is determined like for classical instruments. The transmission of the receptor module is based on the transmission of each optical element. This means that it is necessary to assess the efficiency of field optics devices, corrective lens, focusing lens and dichroic lens. The total efficiency of transmission of a complete system then can be determined as,

$$T_{total} = T_{GP} \times T_{FO} \times T_{LC} \times T_{DL} \times T_{DC} \tag{2.6}$$

where

T_{total} = total of transmission
T_{GP} = transmission of primary array
T_{FO} = transmission of field optics
T_{LC} = transmission of chromatism correction lens
T_{DL} = transmission of doublet lens
T_{DC} = transmission of dichroic mirror

This transmission will be compromised in optimization process with adpodization profile for contrast enhancement to determine the best parameter for Fresnel arrays, see chapter 3. The efficiency of light transmission may be smaller than in classical systems of identical aperture, but Fresnel design will allow larger apertures in space than classical systems.

2.3.1 Primary array

The primary array's efficiency of transmission (T_{GP}) gives the percentage of focused light onto the primary image plane, compared to the incoming light. Numerical simulation of light propagation through a Fresnel array by Denis Serre (Serre D., 2007)[3] shows that we can achieve 6-8 % transmission. Since the number of photons in FIS is essential for an imaging system, it is carefully studied and deliberately optimised to get the most efficient array transmission. For each of our new design of arrays, we have numerically simulated the percentage of transmission. The T_{GP} has been improved with new design patterns of primary array layout.

Specifications	Field optic
Optical Design	Maksutov-Cassegrains
Mirror	150mm
Focal Length	1800 nm
Diaphragm	45 mm

Table 2.1: Characteristics of Field optic in Fresnel imagery, The diaphram diameter limits the beam.

2.3.2 Field optics

The field optics is a classical Maksutov telescope designed for sky observation. For Fresnel prototype generation II, it is modified to have a diaphragm of 45 mm as a diameter of the field in the primary focal plane. Efficiency of transmission of field optics (T_{FO}) is the proportion of light passing through the Maskutov telescope. T_{FO} is 79 %.

2.3.3 Order zero mask

The order zero mask is a 2mm diamter disc. It obturates 0.33 % of the order 1 beam. The resulting transmission is then, 99.7%.

2.3.4 Chromatic correction lens

This chromatic correction lens designed by Denis Serre and Paul Deba D. Serre, P. Deba, and L. Koechlin)[19] corrects the diffracted light passing through by operating at order -1 and reorders the light wave to create order '+1-1'.

This chromatic lens is theoretically estimated to have T_{LC} = 98 % over the useful wave band. The transmission rate will decrease as much as the observed wavelength is shifted away from the central wavelength. This lens is not coated against reflection, therefore the transmission efficiency is 94%.

2.3.5 Focusing doublet

To construct an image in the final image plane, a doublet lens is positioned a short distance after the chromatic correction lens. It converges the wave from the chromatic correction lens to the focal point. The doublet lens is custom-made. The transmission efficiency of this doublet lens is about 96 %.

2.3.6 Dichroic plate

The dichroic plate is either transparent or reflective depending on the wavelength. It is used to separate incoming light into two channels at different wavelengths. Like a beam splitter, it dispatches light to the science channel and the navigation channel: each with its own

detectors. One of those channels will receive near infra-red ($\lambda > 742$ nm) and the other channel will be more centered on the visible band ($\lambda < 742$ nm).(Koechlin L. et al, 2010)[11]

Depending on the science targets, we used one band for science and another for navigation or the opposite, to get the best image. Figure 2.1 shows the bandpass of our dichroic plate. The near infra-red band is represented by the green region, which is raised to 98 % above 742 nm. On reflective side, the blue region represents the visible band, which drops to 2 % above 740 nm.

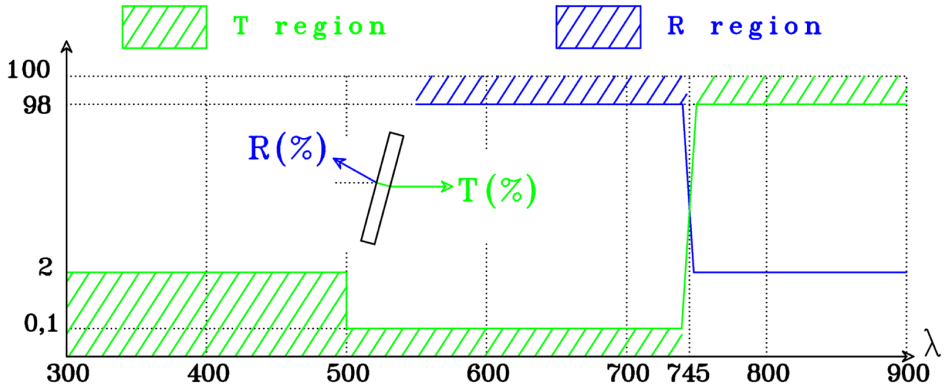

Figure 2.1: Designed bandpass of dichroic plate, the two channels are separated at 745 nm; the blue line corresponds to the visible channel; the green line corrreponds to the IR Channel. (Designed by Paul Deba.)

2.4 Photometry and exposure time

To predict the number of photons at detector level from the previous section, we have the necessary parameters that determine the efficiency of light transmitted into the system. Now, we determine the number of photons falling on the detector by applying equation 2.5. The number of photons that passes through the Fresnel system can be expressed in terms of transmission as

$$N_d = \frac{B \times t \times S}{hc/\lambda} \times T_{GP} \times T_{FO} \times T_{LC} \times T_{DL} \times T_{DC} \tag{2.7}$$

where

t = exposure time
S = aperture area

If we know the magnitude of a source, by using equation 2.5, we can calculate the expected amount of photons on our detector. Table 2.2 shows the numbers of photons, arriving at detector from different sources. In this calculation, the quantum efficiency of the detector (Q_E) is assumed to be 60% at a selected waveband.

2.4.1 Exposure times

In astrophysical imaging, we have to know the exposure time required for the targets that we observe. Then, equation 2.7 is applied to calculate the exposure time that yields a sufficient

Source	Initial photons	time (s)	T_{GP}	T_{FO}	T_{LC}	T_{DL}	T_{DC}	Q_E	N_d
Sun	4.44×10^{19}	1	0.06	0.79	0.94	0.96	0.98	0.6	1.1×10^{18}
Sirius A	1.56×10^{9}	1	0.06	0.79	0.94	0.96	0.98	0.6	2.6×10^{7}
Sirius B	9.8×10^{4}	1	0.06	0.79	0.94	0.96	0.98	0.6	1.6×10^{3}

Table 2.2: Compared number of photons detected from two different sources (from catalogue data) for a 0.04 m^2 Fresnel array, assuming a 15% reflective bandwidth centered at 680 nm. source: Washington Double stars Catalog, interpolatted between R and I band

number of photons to create a usable image. Therefore, exposure time t_{exp} can be rewritten as:

$$t_{exp} = \frac{N_d \times hc}{B \times S \times \lambda} \times \frac{1}{T_{GP} \times T_{LO} \times T_{LC} \times T_{DL} \times T_{DC} \times T_{QE}} \tag{2.8}$$

Equation 2.8 is an exposure time calculation as a function of the required number of photons, the wavelength, and the aperture area of the instrument. For instance, for an image of Sirius B captured with the condition N_d = 140, an exposure time of *83* milliseconds is required, which is the exposure time that we have used to detect Sirius B.

2.5 High dynamic range in Fresnel Imager

One of the main features of a Fresnel Imager is high dynamic range imaging. The designed patterns in a Fresnel array influences a diffraction pattern in images. As explained in chapter 1., diffraction in Fresnel Imager causes a very compact focusing on the central lobe and the four spikes of the point spread function. Therefore, there is less energy scattered into the rest of the image.

The specifications of a Fresnel Array are the keys to diffraction pattern and PSF. The number of Fresnel zones, aperture dimension, apodisation, designed pattern of the arrays etc. are vital parameters leading to the dynamic range. High dynamic range in Fresnel imagery is defined by: ratio of the background level over the central lobe.

2.5.1 Fresnel Arrays and dynamic range

The characteristics of images constructed by a Fresnel array are consequences of the design pattern as shown in chapter 1, i.e. round and rectangular layout of transmission pattern. The original Soret's zone plate (Soret, 1875)[22] is shown in figure 2.2. It is the original circular geometry used since 1875. When the number of Fresnel zones is high, the diffraction pattern from a point source is almost the same as with a round solid aperture, shown in figure 1.3. Since 2005, it has been remodelled into an orthogonal geometry (square format), which can provide high-contrast images, high-angular resolutions and mechanical cohesion (Koechlin L. et al, 2005)[10].

The Fresnel array, which has been transformed, has a number of sub apertures, the dimensions of which get narrower down by the border of the array as shown in figure 2.4. In the image of a point source (PSF) figure 2.3, the background level in each quadrants is re-

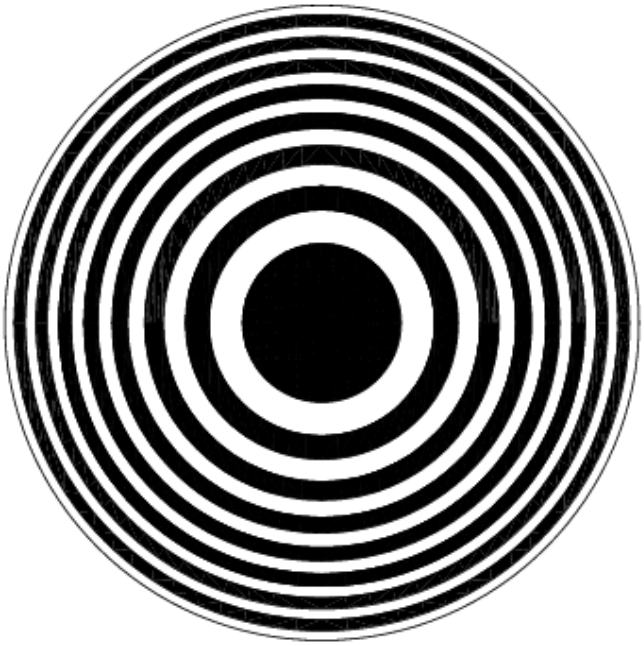

Figure 2.2: Soret Fresnel Zone Plate 1875

ferred to as b-region, shown in blue. In an a-region, shown in red, are the background levels sampled that are used for the dynamic range assessment.

The orthogonal layout in figure 1.7 was merged into the circular design of figure 2.2 in order to form the bars as a structure to frame the subapertures. This has been in use since laboratory testing. Figure 2.4 shows such a Fresnel array made in 2006, which was made at 80×80 mm. It contains 116 Fresnel zones from center to the corner. The array in figure 2.4, was also modified by applying apodization to improve image contrast. The apodization scheme will be explained in the next chapter.

2.5.2 Numerical simulations on dynamic range, and measurements

The dynamic range of Fresnel Imager is studied to assess the instrument's capabilities and limitations. Numerical wave propagation and image simulations have been made to measure the relation between the dynamic range of image and parameters in a Fresnel array. This study is made by using different patterns of arrays layout and observing the characteristics of the output images.

In the section above, I explained the high dynamic range in Fresnel array design, see fig. 2.3. In this section, I will show the diffractive image from Fresnel array simulation.

Central lobe of PSF

The central lobe of the PSF is shown in figure 2.5, where low light levels are enhanced. It is compact and rapidly decreases as a function of the distance from the center of the field. The central lobe concentrates 60% of the energy spreading over the image plane at order 1. The rest is mostly in the four spikes.

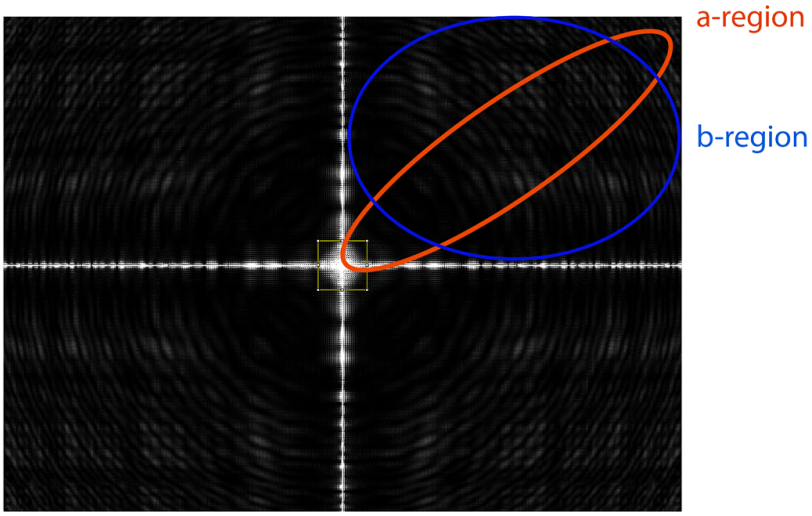

Figure 2.3: PSF obtained by numerical simulation. Our new Fresnel Design (Orthogonal transformation) extends the contrast between central lobe and background level in quadrants, as *b* region. The areas where the contrast is sampled for dynamic range assessment are in the *a* region.

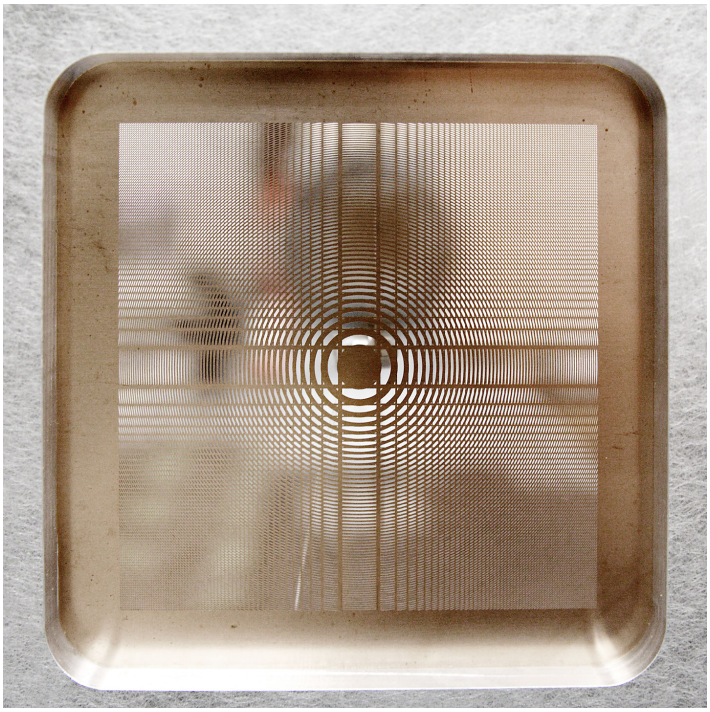

Figure 2.4: 80 × 80 mm Fresnel Array in orthogonal form by Laurent Koechlin et al in 2006, used for Test-bed in laboratory.

To determine the contrast level, we measure the intensity of the central lobe, and use the standard deviation in the background (outside the spikes and the lobe), see next section. To measure the image's properties, we use a 100×100 pixel square at the center of the image, which is shown in figure 2.5. In the output of the simulation program, the maximum level in one pixel is normalised to 4×10^9.

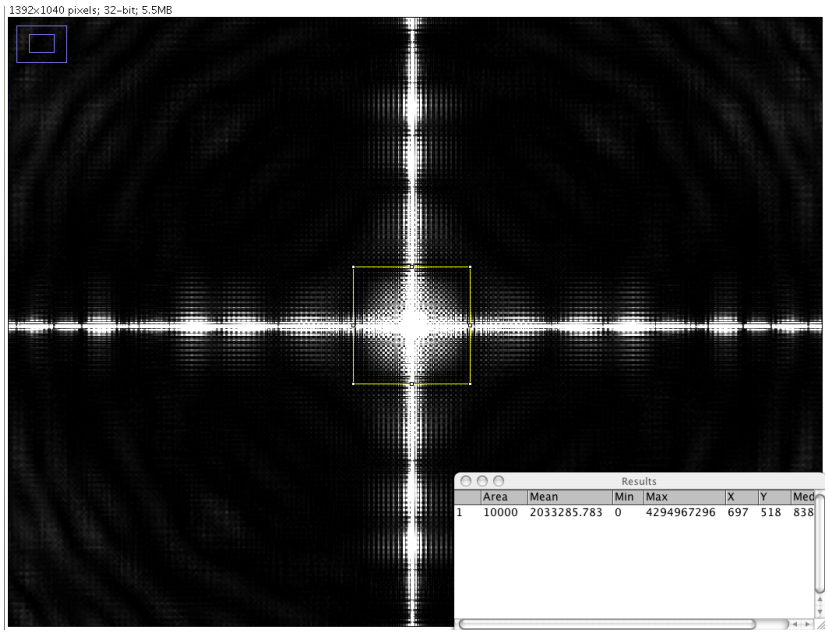

Figure 2.5: Central lobe measurement on the image obtained by Fresnel imager simulator for dynamic range determination. (Image contrast has been enhanced to display the faint levels of the PSF)

Spikes, quadrants, background.

The PSF in figure 2.6 presents four spikes spreading out of the central lobe. These four spikes divide the image field into four symmetrical quadrants. By sampling the equivalent size 100 by 100 pixels at a distance of 200 pixels from the central lobe, we measured standard deviation of the background level. As shown in figure 2.6, very little energy is distributed in the four quadrants.

This measurement is used to determine the dynamic range in the PSF as a function of the distance from the central lobe. The intensity in the area covered by the four spikes is strong compared to the background but weak compared to the central lobe, approximately 10^{-3} in both comparisons. The spikes region is not suitable to high-contrast imaging.

2.5.3 Fresnel diffractive Imagery arrays and High Dynamic Range (HDR)

At this step, we use our measurements to calculate the dynamic range (DR) at different distances from the central lobe. We find the dynamic range by determining the ratio between the standard deviation and the maximum value in the central lobe in the background level:

$$DR = \frac{Std}{I_{Max}} \tag{2.9}$$

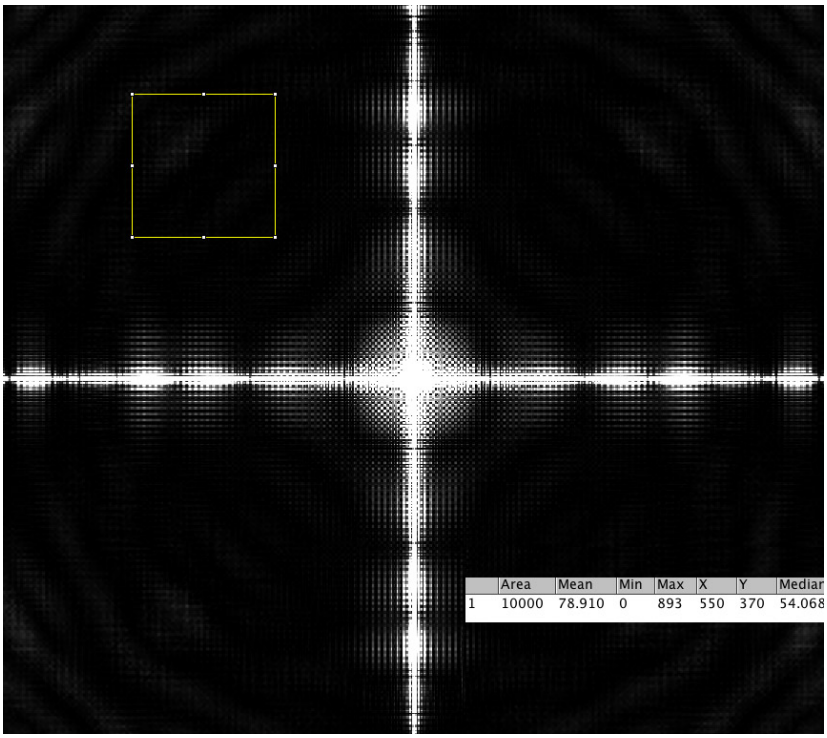

Figure 2.6: Background measurement on the same field as the figure 2.5. (Image contrast has been enhanced to display the faint levels of the PSF)

In figure 2.6, we measure a dynamic range of 1.8×10^{-8}. This value from a numerical simulation is an upper limit in the raw images that we will use in order to estimate the instrument capability.

Part II

Prototype generation II

Chapter 3

Optimization for prototype generation II, ground-based observation

Figure 3.1: *" Grand Equatorial"* dome in observatoire de la Côte d'Azur, built in 1887.

Since 2005 the Fresnel diffractive imager has been developed and tested at the laboratoire d'Astrophysique Toulouse-Tarbes (LATT) at Observatoire Midi Pyreńeés by Laurent Koechlin, Paul Deba and Denis Serre. A laboratory test-bed, prototype generation I, was made and the concept was successfully demonstrated in 2007 by Denis Serre(Serre D., 2007)[3]. The results, in generation I, have proven that the concept of Fresnel diffractive focalisation satisfied and fulfilled the requirements at small scale. The promising potential

of high-angular resolution and dynamic range for space observation drives this concept to further developments. In a new step to convince the astrophysical community, we are now trying a larger-scale test with astrophysical targets. As the concept of Fresnel imagery is developed for space mission at high-angular resolution and high dynamic range, it is difficult and expensive to test a prototype in space. A testing on Earth is more feasible. Hence the idea of ground-based Fresnel for sky-observation. The long focal length of Fresnel arrays is a decisive factor; so we had to find a long focal instrument to hold and control the orientation of the prototype. Fortunately, there is a long tube refractor in *" Grand Equatorial"* dome, located in Nice, see figure 3.1. In figure 3.2, this 18-meter refractor, built in 1887, is maintained to be functional for visitors and occasional observations. Our prototype generation II has been modified to operate on this refractor mount. To observe real astrophysical targets and observe the sky in real conditions, Fresnel imager in generation II has been enlarged. The modifications are made to both the Fresnel array and to the receptor modules to improve the performance.

In this chapter, we will present the improvements that we made to Fresnel Imager prototype generation II. The first sections will show the modifications of the primary array; in particular the parameters that we optimized and the constraints and difficulties that we encountered. In the following section, I will describe the essential improvements of receptor modules to illustrate the devices that have been integrated and optimized in prototype generation II. The modifications in the receptor module are in relation to those we made to the Fresnel array module.

Figure 3.2: The 76cm diameter refractor's tube in the *" Grand Equatorial"* dome, at the Observatoire de la Côte d'Azur, on which prototype generation II will be installed.

3.1 Primary array module

For ground-based observation, an optimization of the primary array is required to improve performance. The 80×80-mm array in generation I is not sufficient to collect the light from

Specifications	Prototype generation II	Prototype generation I
Wavelength	800 nm	600 nm
Bandpass	640- 960 nm	480 - 800 nm
Focal distance	17.96 m	22.99 m
Array size	200 mm	80 mm
Fresnel zones	696 Zones	116 Zones
Resolution (arcsec)	0.8	1.5
Field Optic diameter	45 mm	35 mm
Number of sub-apertures	241,860	26,680

Table 3.1: Prototype I & II specifications compared.

astrophysical sources, therefore, the first improvement is building up a larger array. As I explained previously, the first difficulty in ground-based prototype is focal length. The long focal refractor, shown in figure 3.2, is used as a support to manoeuvre both Fresnel Imager modules. Therefore, focal length is limited by the 19-meter tube. The next parameter in this prototype is wavelength adapted to the conditions of sky observation. The last parameter is the minimum diameter of subapertures that the manufacturer can provide. This manufacture constrains our Fresnel zone number, see equation 1.11. Based on these constraints, the dimension of the primary array in prototype generation II is enlarged to 200 $\times$ 200 mm maximum. This dimension increases the ability to observe: the larger aperture boosts the instrument's sensitivity and resolution. With the present limit in engraving technology (20 μm laser beam), the maximum number of Fresnel array zones increased to 696, compared to 116 zones in generation I (Serre D., 2007)[3]. This 6-fold improvement, compared to the first generation, should have improved the dynamic range in similar conditions. However; as we observe through atmospheric seeing, the performances are not comparable, but we are still able to reach a dynamic around 10^{-5}. The central wavelength is shifted from 600 nm to 800 nm in order to minimise atmospheric turbulence effects and diffusion by the atmosphere. Others functions such as tip-tilt, new designed arrays and an enlarged Fresnel blazed lens have also upgraded the performance of the instrument. Changing the focal distance from 22.99 to 17.96 m, was imposed by the size of the 19-meter-long telescope tube. Table 3.1 shows the improvements of parameters and features in prototype generation II compared to those in generation I.

3.1.1 Primary array optimizations

To optimize a Fresnel array for sky observations, modifications of Fresnel's primary array in prototype generation II are made in three main areas.

1. resolution
2. transmission efficiency

3. dynamic range

These optimizations are the most important parts for our demonstration of the Fresnel imager system. There are relevant parameters, concerning array improvement. However, they are constrained by limiting conditions such as available length of the refractor tube, minimum size of the main array's sub-apertures (20 um) and wavelength used (800 nm).

Resolution

Angular resolution in prototype generation II has improved thanks to the larger aperture of the Fresnel array. It is adapted to resolve interesting astrophysical targets, such as close binary stars and fine detail on planetary surface. With a 2.5 times larger aperture in Fresnel prototype II, the resolution should be 2.5 times better than with prototype generation I. As a matter of fact, that instrument is made to observe in Near Infra-Red (NIR) at 800 nm. The angular resolution went from 1.5 arcsec in prototype generation I to 0.8 arcsec in generation II, see equation 1.12. This two fold improvement in resolution is a trade-off with wavelength, which is our constraint for sky observation with less atmospheric turbulence and diffusion.

Transmission efficiency

Transmission efficiency in prototype II is improved as the collector area is 2.5^2 times larger than in prototype I. The geometry of the bars that hold the Fresnel Array structure is optimized to allow more light to travel to the focal plane. This will lessen the exposure time required to detect a given number of photons, which increases the limiting magnitude by 2.6.

Optimization of transmission efficiency is a delicate problem. As explained in chapter 1, the focused Fresnel diffractive light wave is relatively faint, compared to classical optics systems. Only approximatively 7 % of the incoming wave is diffracted into order 1, which is usable to construct an image, althought about 50 % of input light passes through the Fresnel array; this percentage contributes to light in order 0, order 1, order 2 etc. Only order "1" will be focused onto the field optics afterwards. Therefore, transmission efficiency is a critical issue of the Fresnel array, which must be tackled in prototype generation II. As is shown in figure 3.3, the opaque area includes the opaque parts from the Fresnel zone plate and in addition the orthogonal bars. These bars were set to maintain the structure of the array. They also block the light wave that comes into the Fresnel array. Merging orthogonal bars into the Fresnel zone is also a trade-off between transmission and strength of array structure. The efficiencyiy of transmission will certainly increase if there are thin bars all over a Fresnel array. Nevertheless, this has a limit as it affects the mechanical stiffness of the array. Determining minimum bars to maintain the stiffness of solid structure is a compromise. By numerically simulating image formation, the best compromise we found was to apply one orthogonal bar in every third Fresnel zone and a bar width corresponding to $0.12 \times$ the pseudo period of the local Fresnel zone. [3]

In figure 3.4, the design of the new array has fewer bars than the previous array in figure 3.3. The orthogonal bars are connected to opaque part of every third Fresnel zone. This design may be less stiff than the one in prototype generation I, but it is enough to maintain the solidity of the Fresnel array.

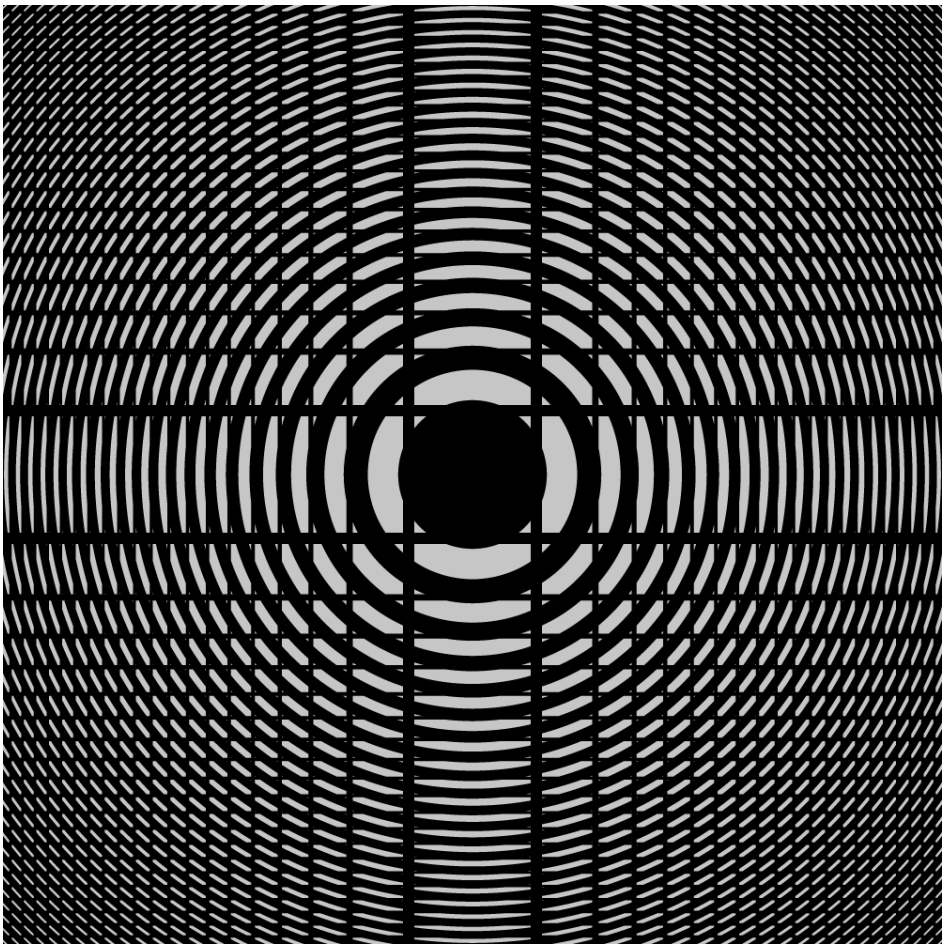

Figure 3.3: Fresnel Array design, to diffract light in order 1, and to focus the beam. This layout uses a bar at every Fresnel zone to reinforce and hold the structure of the array. This array design is used in the test-bed of prototype generation I.

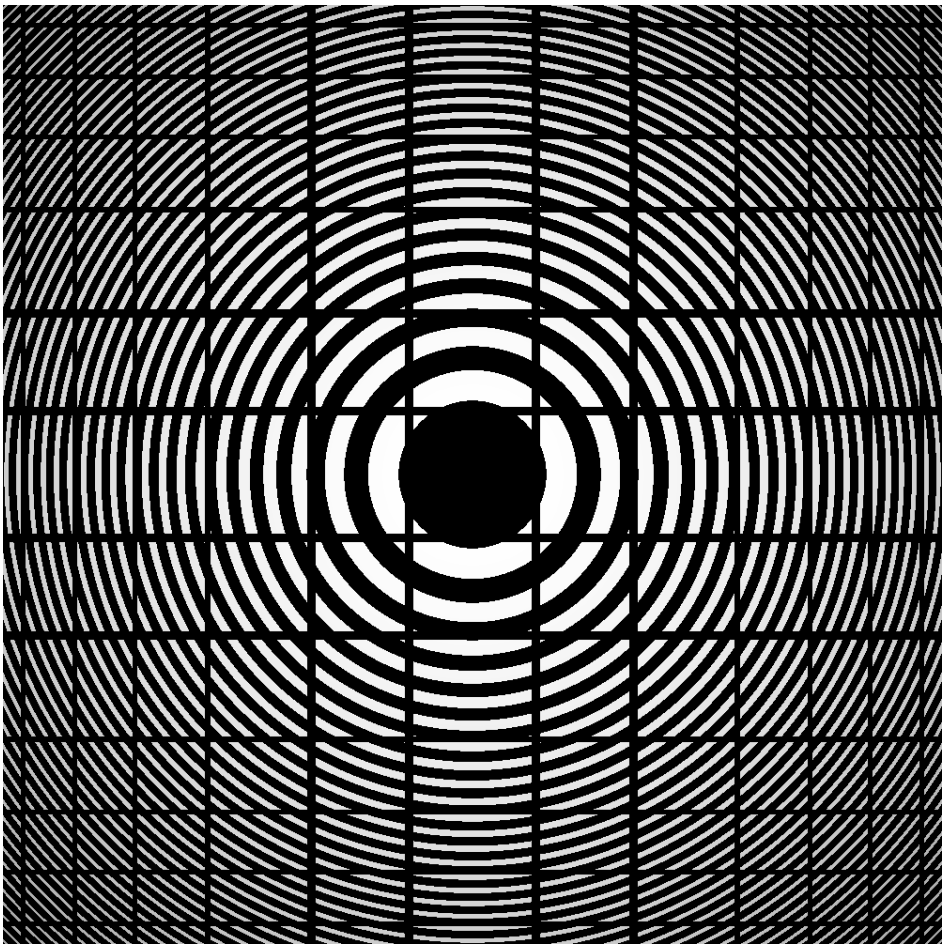

Figure 3.4: Fresnel Array layout, used to diffract and focus light order 1, designed to have fewer bars than the original [one bar in every three Fresnel zone improves the PSF].

Dynamic range

Dynamic range is improved by Fresnel array layout modifications. The layout of the new bars reduces spikes luminosity and background noise. This, combined with the increased number of Fresnel zones, boosts the dynamic range by a large number.

Dynamic range of Fresnel array in prototype generation II is increased as the number of Fresnel zones and aperture is raised. Another key factor to both transmission and dynamic range is apodization profile.

Apodization and Sampling of numerical PSF Apodization is a general method to improve dynamic range by removing the "feet" of the PSF and we apply it to a Fresnel diffractive array layout. It will lower the second lobe and reduce the background level in the field. It enhances signal-to noise ratio in certain cases; such as binary star observation. An apodization function is chosen to produce a better dynamic range around the central lobe of the PSF. The proportion of $void/opaque$ area in a given Fresnel zone is reduced when it goes from the center to the edge of the array. This also means that efficiency of transmission will be decreased as it leaves the central zone. Different apodization functions have been tested in order to get the best dynamic curve for Fresnel arrays in generation II. The functions used for apodization can be cos , $\cos^2$ or prolate. (Serre D., 2007)[3]

The 1D apodization functions can be expressed as:

$$Apod_{cos}(x) = \cos[\frac{2x}{C} acos(a_0)] \tag{3.1}$$

$$Apod_{cos^2}(x) = \cos[\frac{2x}{C} acos(\sqrt{a_0})]^2 \tag{3.2}$$

The total transmission rate of the main array drops from 5.84 % to 5.72 % when we use $\cos^2$ instead of cos although best dynamic range is obtained by cos^2 and the lower limit in transmission for an apodization function is 0.11.

The 2D Apodization in orthogonal coordinates can be written as

$$Apod(x, y) = Apod_x(x) Apod_y(y) \tag{3.3}$$

By applying equation 3.3 to the orthogonal function of the Fresnel array, T_c, the modified transmission is expressed as

$$T_{ap}(x, y) = T_c(x, y) Apod(x, y) \tag{3.4}$$

Applying this appodization to modulate the width of the transmission zone, we obtain Fresnel arrays shown in figures 3.3 and 3.4. As you can see, the apodisation function does not go down to zero at the edge of aperture. It stops at $a_0 = 0.1$ since we cannot cut an aperture smaller than the laser beam, used in the machine tool, 20 μm-laser.

Dynamic range measurement In order to assess the dynamic range of the Fresnel array, we numerically simulate the wave propagation from the Fresnel array to the first focal plane. Our simulation calculates the PSF at given initial conditions such as wavelength, Fresnel array structure, dimension, focal plane position etc. By measuring the simulated output image, we calculate the dynamic range as explained in chapter 2. We tested different designs

and optimized parameters in order to compare and find the highest dynamic range from this optimisation. The contribution of apodization is shown in figures 3.5 - 3.8. The PSF profile curves shown are a comparison of dynamic ranges with different profiles.

The apodization, which is obtained by modulating the width of each Fresnel zone, is optimized to increase transmission and decrease disturbance to the PSF. The PSF profiles, presented in red, green and blue, are tested to find the best dynamic range within 50 resels of the center of the field. The red curve, issued from a 10% edge transmission apodization, is the finest and gives the largest dynamic range at 5 resels: 10^{-5}. The dynamic range can drop quicker within 10 resels around the central lobe, but they perform very identically at a distance of 10-20 resels. With a 200 by 200 mm Fresnel array, we chose $a_0 = 0.11$ (transmission at the edge of the array, as $a_0 = 0.1$ would require to engrave minimum apertures sizes smaller than 20 μm, which the manufacturer cannot provide. The width of the holding bars correspond to 6% of the Fresnel zone to which they are tangent.

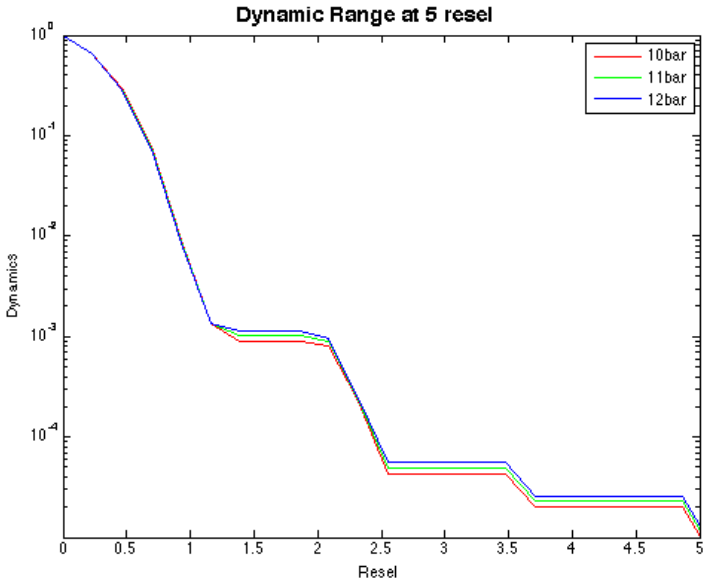

Figure 3.5: Dynamic range for 5 resels from the central lobe of the PSF: the red curve corresponds to an edge apodisation ratio of 0.10, green to 0.11 and blue to 0.12.

The results of different apodizations functions are shown in figures 3.5 - 3.6 and figure 3.10. These dynamic range curves correspond to sampled resels in the diagonal from the center of the image, showing the proportion of local intensity to maximum intensity at the central lobe. The best dynamic range measurements in the PSF are shown in figure 3.8. It plots the contrast from the center towards the edge of the image for a length of 50 resels [$\frac{1}{8}$ of the field].

The relative bar width at 6% of its corresponding Fresnel zone gives the highest transmission rate for the array. The apodization improves the dynamic range although it reduces the transmission rate in Fresnel array.

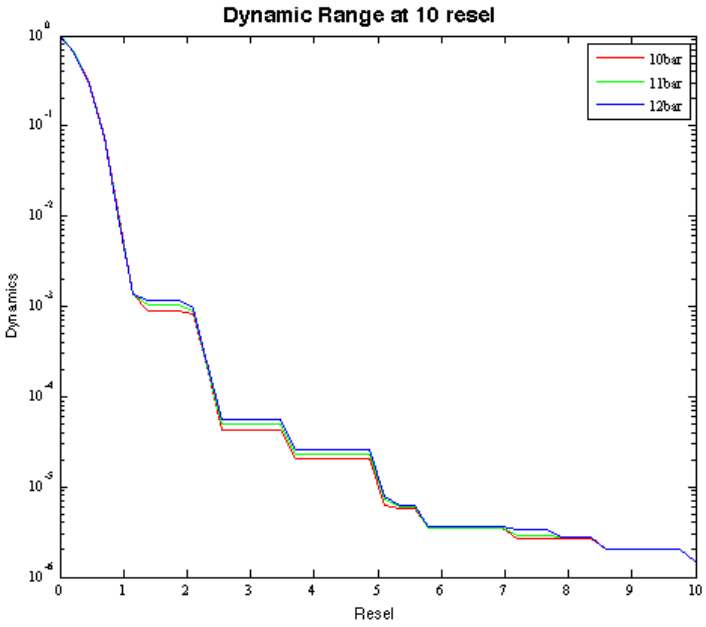

Figure 3.6: Dynamic range studies for 10 resels from the central lobe of the PSF: the red curve corresponds to an edge apodisation ratio of 0.10, green to 0.11 and blue to 0.12.

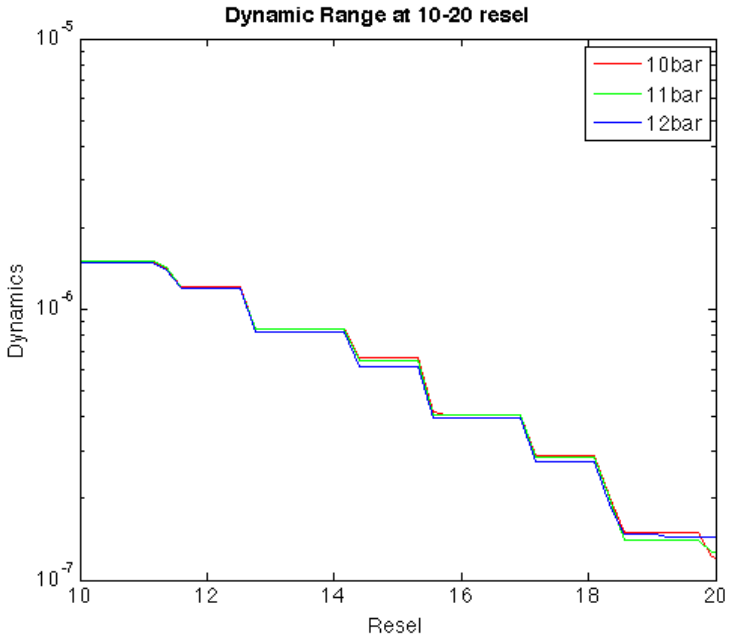

Figure 3.7: Fresnel dynamic range from 10 to 20 resels in the diagonal direction from the central lobe of the PSF.

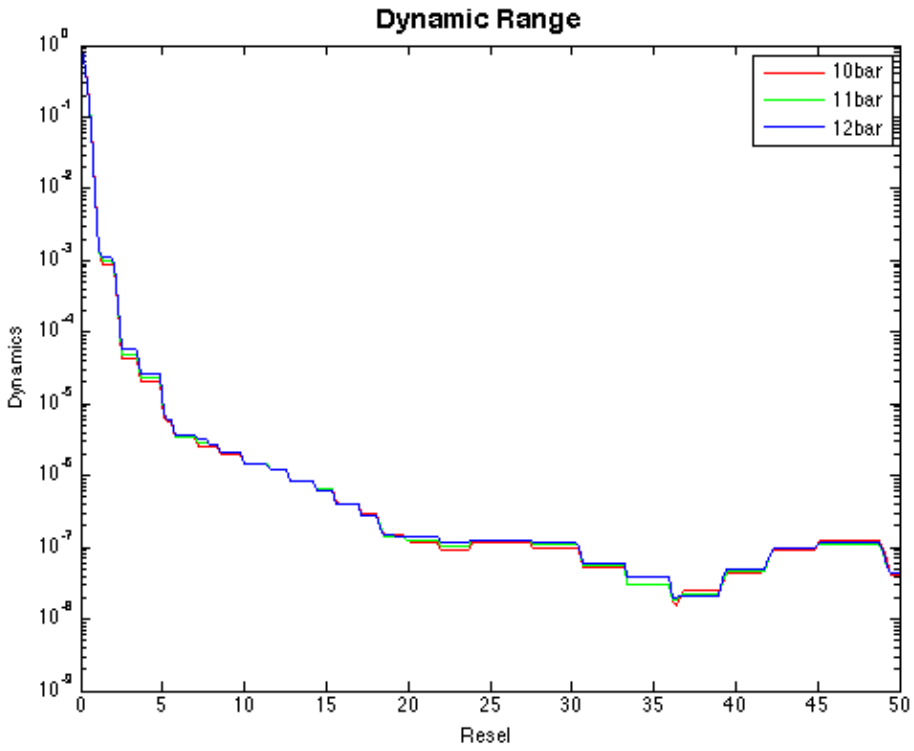

Figure 3.8: f

or three different a_0 values, 0.1, 0.11, 0.12 and orthogonal bars tangent to everyzone. Dynamic range for 50 resels from the central lobe of the PSF for three different a_0 values, 0.1, 0.11, 0.12 and orthogonal bars tangent to every zone.

3.1.2 Primary array fabrication.

The result of the optimization process is a list of specifications used to make a Fresnel array in prototype generation II. This array is to test on sky observation for validation. The results from validation will be used to modify the next version of the Fresnel array. At present, the parameters, which give the best performance in dynamic range and transmission are shown in table 3.2.

Finally, we obtain the parameters that give us the best performance regarding transmission and dynamic range compromise. After this procedure was completed, we sent the array parameters for construction. Once carved, it is used in Fresnel prototype generation II.

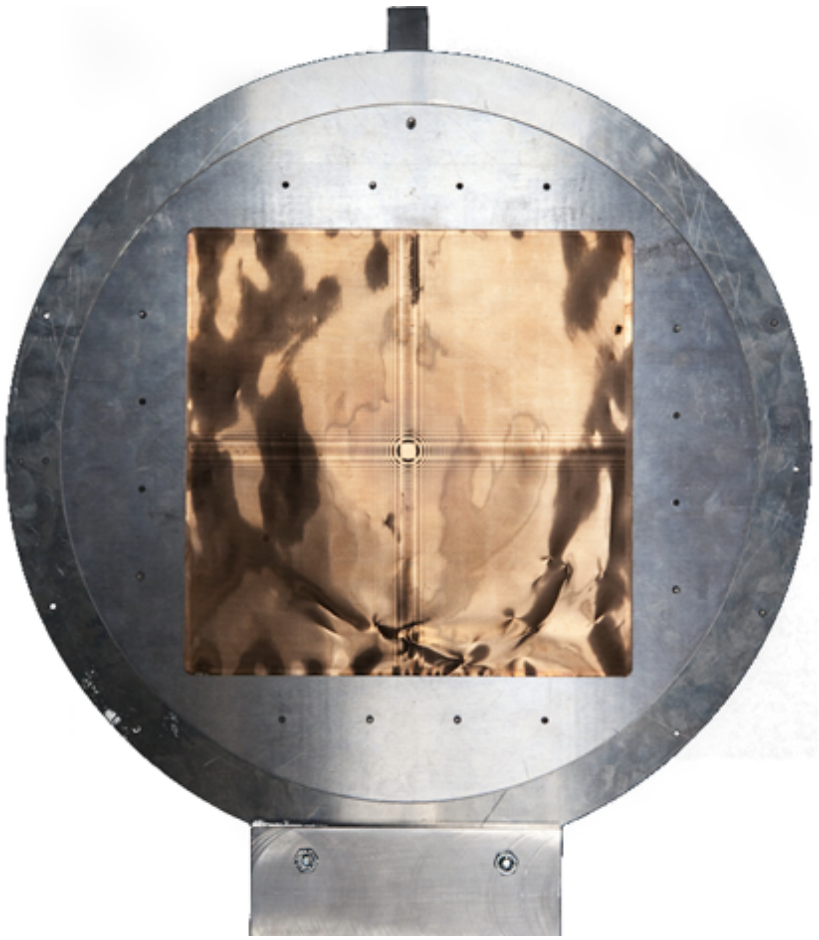

Figure 3.9: Fresnel Array in Generation II prototype, this array is 20 by 20 cm made of a thin metal foil with approximately 250000 apertures. It is held by a mechanical support allowing rotation around its optical axis in order to orient the spikes correctly in the image plane.

Apodisation reduces the size of the sub apertures at the edge of the array. At current technology level, the cutting machine used for engraving has a 20μm-diameter beam. Therefore the size of the sub apertures has to be larger than 20μm. This limits the apodisation parameter to 0.11, which we use for the current array.

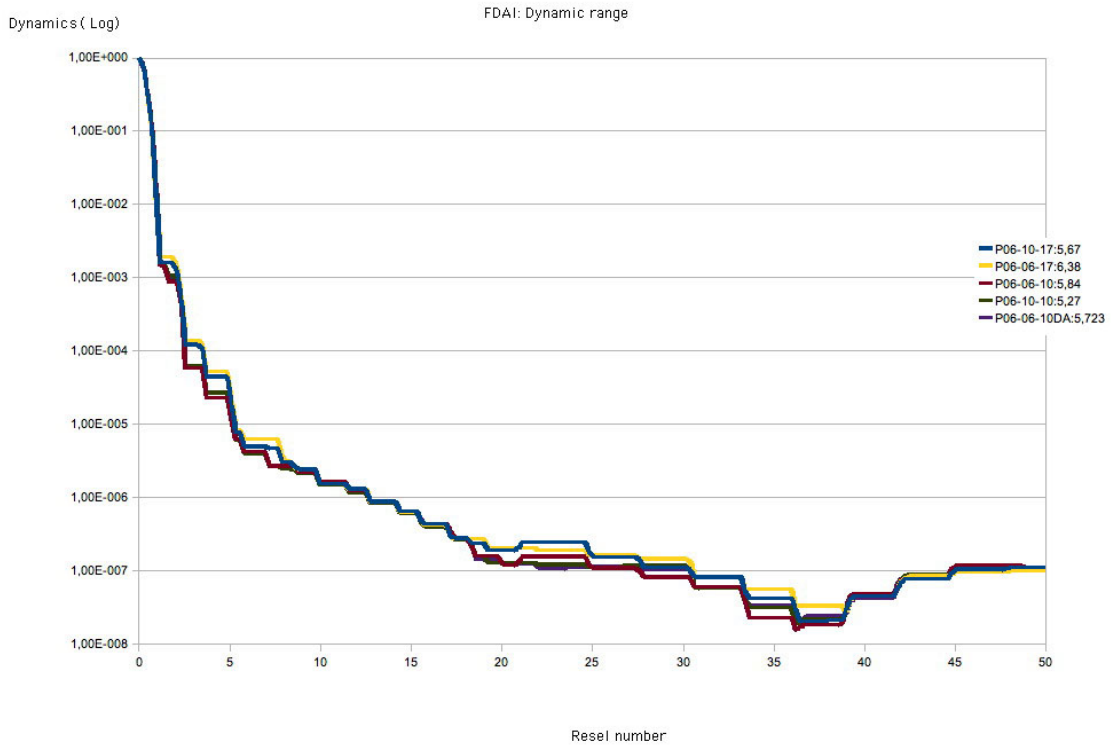

Figure 3.10: Dynamic range from arrays with different apodization parameters and different bar widths. The last numbers on the middle right of the figure correspond to the overall efficiency into order one(5.67, 6.38). The best curve is the red one at 6% bar width and $a_0 = 0.10$. The profile in the bottom is double cosine function.

Specifications	Prototype generation II
Array size	200 mm
Array zones	696 Zones
Transmission	5.95%
dynamic at 10 resel	10^{-6}
dynamic at 20 resel	10^{-7}
dynamic at 50 resel	10^{-7}
Bar width max	0.06
Bar width min	0.06
Apodisation function	$\cos^2$
Apo Max	0.25
Apo Min	0.11

Table 3.2: Main array's specifications and performances (From numerical simulation)

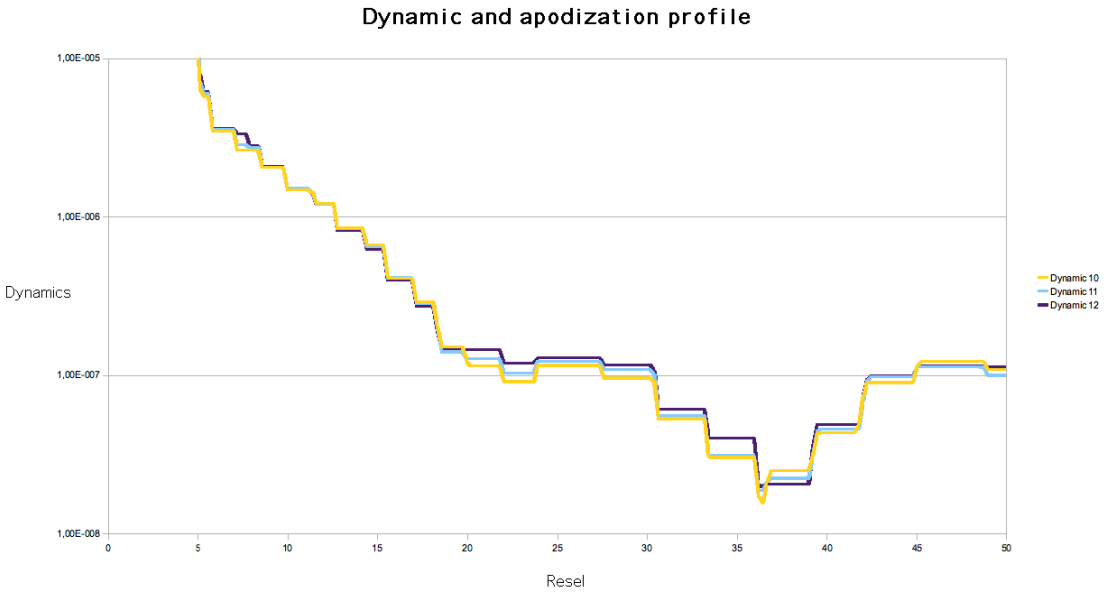

Figure 3.11: Comparision of dynamic range curves with different values of edge transmission(a_0).

3.2 Receptor Module

The receptor module in prototype generation II is modified to support improved features from the primary array. The receptor module is placed on the image plane of the Fresnel Array 18 meters down stream at the other end of the refractor tube. It is installed on a 2-meter optical rail. Receptor devices in prototype generation II are upgraded to operate in conjunction with the new array specifications. This section will describe the modification and optimization process applied to receptor module.

3.2.1 Field optics

The field optics in prototype generation II still use a Maksutov telescope, the same as that in generation I. This field optics have a nominal focal length of 1800 mm, with a nominal aperture of 150 mm. The modifications made in this generation, to keep up with the new Fresnel array, are a larger diaphragm of the field optic, which increases the linear field at prime focus from 30 to 45mm. Consequently, this 45-mm diaphragm of the field optics also increases the bandpass of focused light into receptor module, as described in chapter 1. The unvignetted bandpass is limited to 690-900 nm.

3.2.2 Order zero mask

The order 0 mask is used to block the light from order 0 that has been focused by the field optics. Its support is modified to let through an enlarged beam (from order “1”). Order “0” mask in prototype generation II has a 2-mm diameter. It is made of a thin opaque disk held by four Kevlar wires. (Koechlin L. et al., 2010)[11] This small mask allows the beam from order “1” to pass around as it has a 40-mm diameter at this position. Figure 3.12 shows the order “0” mask placed inside its tube.

Figure 3.12: Order 0 mask used to eliminate order 0.

3.2.3 Chromatic correction lens

In order to correct chromatism in the Fresnel Imaging system, the blazed lens is built to support improvements to the Fresnel array. Since the new Fresnel array has increased the number of Fresnel zones to 696, the chromatic correction lens needed to be modified to serve the additional Fresnel zones. The new blazed lens is made to correct 702 Fresnel zones. It is engraved on a 100-mm fused silica disc and fits a 58-mm diameter beam in the pupil plane.

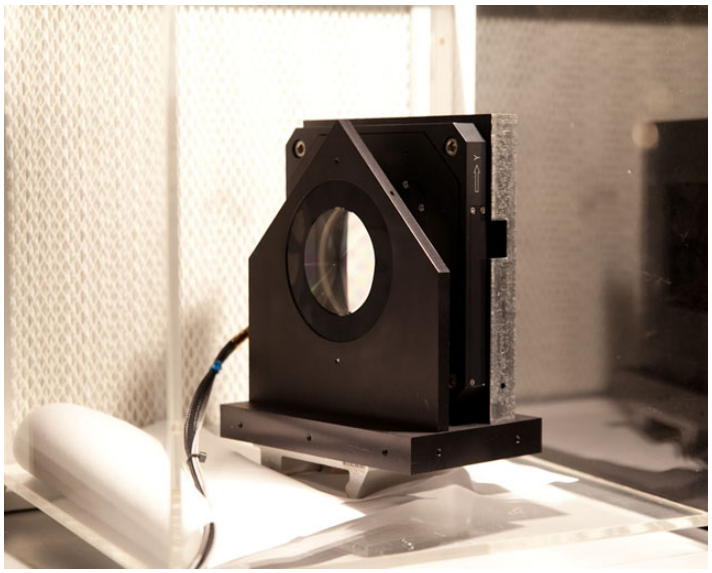

Figure 3.13: Cell holding the Fresnel correction lens (triangle), and the doublet lens (square PZT actuator).

3.2.4 Doublet lens

The doublet lens and chromatic correction lens are placed in the same box, shown in figure 3.14. This box is baffled to protect those optical elements against dust and stray light. It can be manually tilted and shifted for alignment actions to bust ghosts or other optical defects. It is supported by a tip-tilt actuator for atmosphere turbulence compensation. This compensation is required for long-exposure acquisitions.

3.2.5 Dichroic beam splitter

The dichroic beam splitter dividing the beam into two different channels, one for guiding, and one for sciences, has been installed in front of the EMCCD cameras. In figure 3.15, the box contains the dichroic plate and holds the EMCCD cameras. It is baffled to protect against interference from external light.

3.2.6 Detectors

Module detectors are EMCCD cameras, from *Andor*. The detectors are installed on the same box as a dichroic beam splitter as shown in figure 3.15. One of the detectors is used

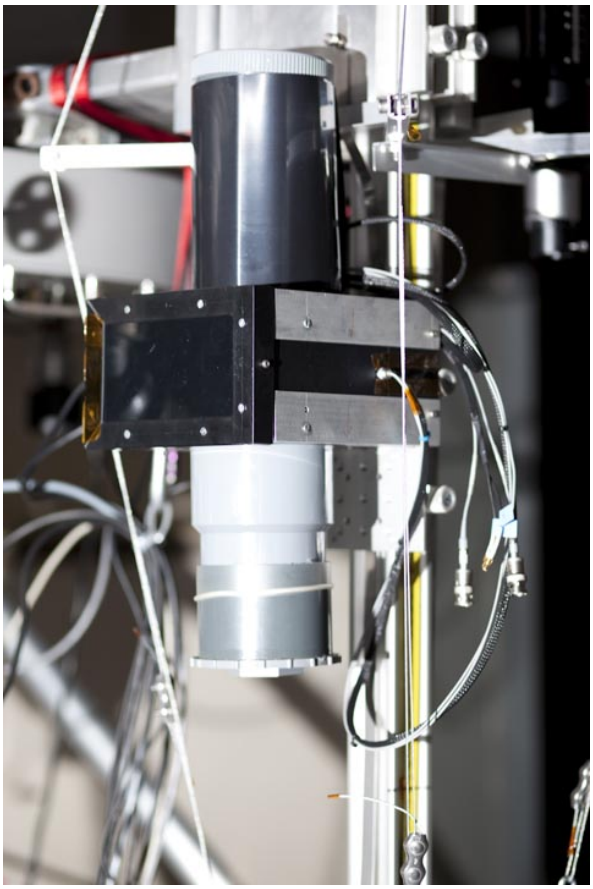

Figure 3.14: Baffled box containing the doublet lens, held by the tip-tilt actuator and the chromatics correction Fresnel lens.

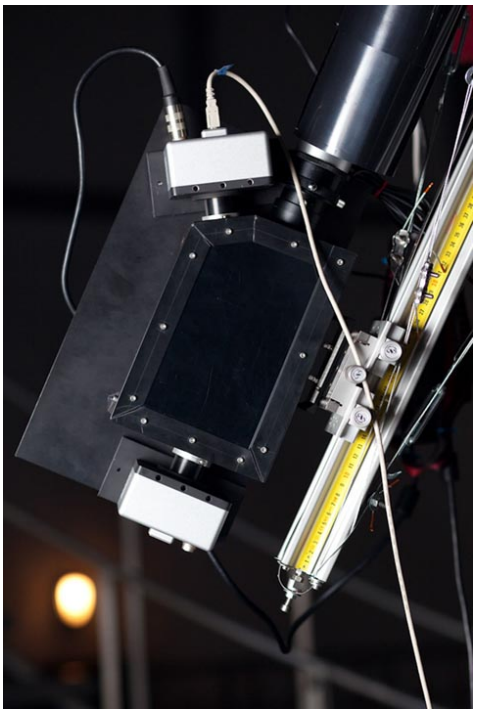

Figure 3.15: baffeld box containing the dichroic beam splitter, on which the navigation and observation cameras are placed at the final image plane.

for navigation. The other one is used for image acquisition. These channels can be swapped if necessary, depending on the astrophysical targets.

Chapter 4

Fresnel diffractive imager's ground-based observation

In the previous chapter, we described how the Fresnel Imager System functions and what key components are part of the prototype generation II. This chapter will be split in two parts. The first part will explain the astrophysical targets, which have been imaged during observation at Observatiore de la Côte d'Azur, in Nice, France. There are several types of targets, such as stars, planets, satellites and nebulae. The second part deals with result images from our observation.

Targets for Fresnel sky observation are chosen to assess and validate the performance of the instrument. Ground-based validation has two important objectives. First, to evaluate the characteristics and operational modes of the Fresnel imaging system in a real situation of sky observation. Second, to assess the quality of astrophysical images observed with a Fresnel diffraction Imager. Observing real astrophysical targets has never been done before with the Fresnel array concept. A picture of the building was made with a classical Fresnel zone plate (holographic lens), but without chromatic correction.(Faklis D. et al, 1989)[5]

This chapter will show the preparation phase for Fresnel observations and the results images from our observations. The first section will describe the categories of targets, how the targets are selected, and what assessments are expected from their observation. The second section of this chapter will show targets' data and the result images from observation, according to the categories.

4.1 Sky targets for Fresnel Observation

As the Fresnel Imager has advantages in high angular resolution and high dynamic range (Serre D., 2007)[21], our selected targets are based on these two aspects. In this case, we divide our targets into two main categories.

High dynamic ranges The targets in this category are objects, which have several points of interests in the field and large differences in brightness. These differences are chosen sufficiently high to demonstrate the instrument's capabilities. For example: a binary system, in which one of the stars is much brighter than the other. The difference in brightness between them is a test for the dynamic range of the Fresnel imager. This type of targets are binary

stars systems, such as Sirius AB or planet-satellite systems, such as the satellites of Mars Phobos and Deimos or the satellites of Saturn.

Angular resolution Our second category of our targets aims to test the angular resolution and field of view. Our instrument with a 200 mm × 200 mm aperture can theoretically resolve a 0.8" angular separation. The field of view is limited by the 4.5 cm field stop at the entrance of the receptor module. Associated with an 17.89-meters focal length of the Primary array, this results in 490 arcsec in field of view. The field of view is further reduced a little due to the size of the CCD in the camera. The dimension of the CCD camera is 8 × 8 mm. It is placed at the final focal plane, where the resulting focal length is 5.30 meter This results to a field of 310" by 310"

Then, selected targets in this category are closely separated objects, such as close binary stars, the moon's surface and planetary surfaces. For example, Mars.

Sensitivity limit Another group of targets in Fresnel observation is intended to test the sensitivity limit. Targets in this group are faint objects or deep sky objects such as Nebulae (M42) or faint stars.

4.2 Evolution of Fresnel Ground-based prototype II

This section will review the validation processes and results at each stage of integration. From chapter 3, we used the results of optimization to build the Fresnel prototype generation II. Both modules were installed in the *Grand Equatorial* dome for the first time in July 2009. The primary module is mounted on the top right side of the tube as shown in figure 4.1. The receptor module is placed on the other end of refractor tube, shown on the left side in figure 4.1. The 24-meter diameter dome has a temperature gradient of 1 °C from top to ground level. In the winter, the temperature inside the dome can drop to 2° C and it is much more stable than outside. Since we started to assemble our prototype, we have tested each component for instrument integration. It has been optimized gradually to assure that each component's functionalities have been well integrated. The Prototype generation II is assembled on the same basis as generation I. The optical rail and its support were fixed on the refractor tube by a non-destructive method to preserve this scientific antique. We started to modify prototype version 1 with some new components. The resulting equipment has been dubbed generation 1.5.1 and evolved to version 2. We tested each configuration step by observing astrophysical targets to study the improvement of the system during integration before installing new components. The improvements of components in modules directly influence the resolution and dynamic range of the instrument. Therefore, each state of integration has different characteristics. Then, we test the instrument at each step: the angular resolution. It is enhanced in each configuration and will be tested to validate the performance of integration. The airy radius, which drives the resoltuion, is given by: $R_{airy} = \lambda / C_{gr}$, for a square aperture size of C_{gr}. As described in chapter 3, a completed Fresnel ground-based prototype's specification is listed at table 4.1

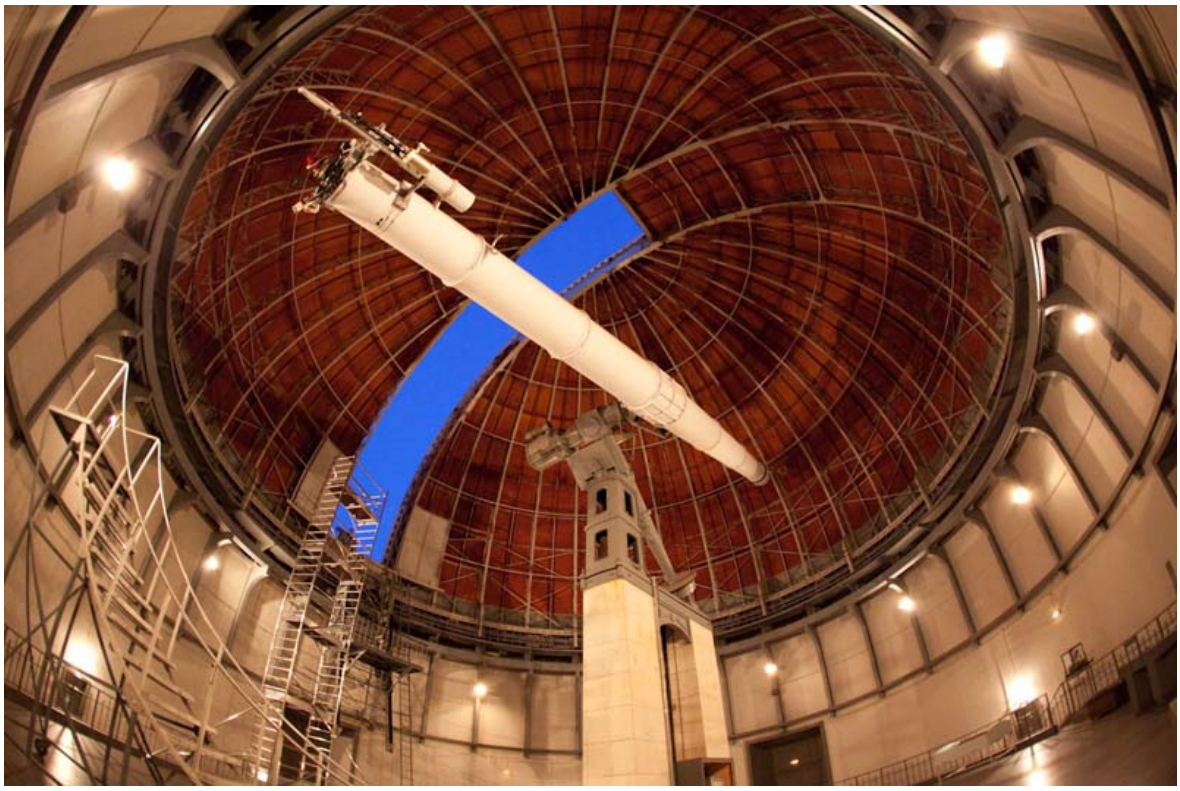

Figure 4.1: Refractor and *Grand Equatorial* dome at Observatoire de la Côte d'Azur: the refractor is 19 meters long and the refractor dome is 24 meters in diameter. The Fresnel array can be distinguished on the right at the far end of the tube. The receptor module on its optical rail can be seen on the left at the close end below the white finder.

Gen. 2 specs	
Fresnel Array size	200 mm
Number of Fresnel zones	696
Central wavelength	800 nm
Unvignetted bandpass	650-950 nm
Primary focal length	17.96 m
Field diameter at prime focus	45 mm
Angular field of view	500"
Angular Airy radius	0.825"
detector pixel size	8 μm
Focal length at detector	5.375 m
pixels per Airy radius	1.9

Table 4.1: Summary of Fresnel Imager testbed generation 2 specifications, as planned before the 2009 test runs.

4.2.1 Optimization and prototype Improvements

Ground-based prototypes are designed to operate on the 19-meter mount of the refractor at Observatoire de la Côte d'Azur in Nice. During installation, one component is assembled at each step. Optimisation of the Fresnel imager is done step by step to guarantee operation.

Stage : 1.5.1

In July 2009, Fresnel Imager "1.5.1", a transition stage from prototype I to II was installed. At this stage, only some components of the Fresnel prototype were moved to a new configuration. A 200-mm array replaces the 80-mm array of prototype I, but the old corrective Fresnel lens, order zero mask, doublet and camera remain. Therefore, the field of view and resolution are smaller than described in table 4.1. In this stage, we had not implemented the tip-tilt yet, so atmospheric turbulence affected the quality of images. This 1.5.1 setup was used in July 2009, for a two-week observation run.

Stage : 1.5.2

In September 2009, a new diffractive blazed lens was added to the ground-based prototype and secondary focusing lens was added in the receptor module. The new Fresnel corrective lens is engraved on a 100-mm diameter fused silica plate. The 702 Fresnel zones fill a 58-mm diameter disk on the silica plate. The new doublet, placed after the diffractive blazed lens, has a 64-mm diameter. The detector is still the Sony Starlight SXVH9 from prototype generation I. At this stage we had not yet installed the tip-tilt module. It will be installed in version 2.0.

Stage: Fresnel version II

Integration This version of our prototype has integrated all the components and completes our primary and secondary module modifications. It has been optimized to the best condition

for sky observation. Tip-tilt is integrated and tested. This version of our prototype has the specifications presented in table 4.1.

Sky observations The prototype generation II was installed and started observation in January 2010. It makes the first complete ground-based validation of a Fresnel imager. Using a 200 × 200 mm array, the large aperture is a major change in this version. Our test targets and the resulting images will be detailed in this section.

4.2.2 Development characteristics

Fresnel Image Sampling In order to determine the potential and limitations of the instrument, we compare the optical resolution at close to optimal sampling scale.(Koechlin, L. Serre, D. and Duchon, P., 2005) [10] In chapter 3, we stated that we adjusted the optics in the secondary module so that the sampling is 2.6 pixel for one resel in *Andor* camera, which has 1002 by 1004 pixels. This sampling determines the angular scale in the final image plane in arcsecond per pixel: 0.307±0.02. From chapter 3, we have a plot of a numerical Fresnel Imager's PSF, which can illustrate the dynamic ranges. In figure 4.2, the curve was obtained from the same numerical simulation as in chapter 3, figure 3.10, but smoothed over a larger 5-pixel kernel. This curve is made to show the limit of the dynamic ranges that the Fresnel Imager can possibly achieve. It shows the brightness ratio (here expressed as the difference in magnitude) between the central lobe of PSF and the background level in the field as a function of distance from the central lobe. In the case of binary stars, this means that the companion would be detectable if its separation and magnitude differences plot it above the curve and undetectable if they fall into the lower side of the curve. In the following parts of this chapter, we will review the characteristics of each target, and position them with respect to angular separation and difference in magnitude. The observation procedure will be described in association with each object. In prototype generation 1.5.1, (July 2009) the resolution was only 1.8 arcesecond for one resel (ρ) with a sampling of 4 pixels/resel. In prototype generation II, the resolution is increased to 0.8 arcsecond for one resel (ρ), sampled at 2.6 pixels/resel. The angular resolution is given by: parallel to the x and y axes of the array,

$$\rho = \frac{\lambda}{C_{Gr}} \tag{4.1}$$

On the diagonal,

$$\rho = \sqrt{2}\frac{\lambda}{C_{Gr}} \tag{4.2}$$

ρ = resel in arcsecond
λ = wavelength
C_{Gr} = diameter of Fresnel array aperture

4.3 Images Obtained

This section will show targets information and observation results. Targets that have been selected will be depicted in validation phases according to each category. Targets images

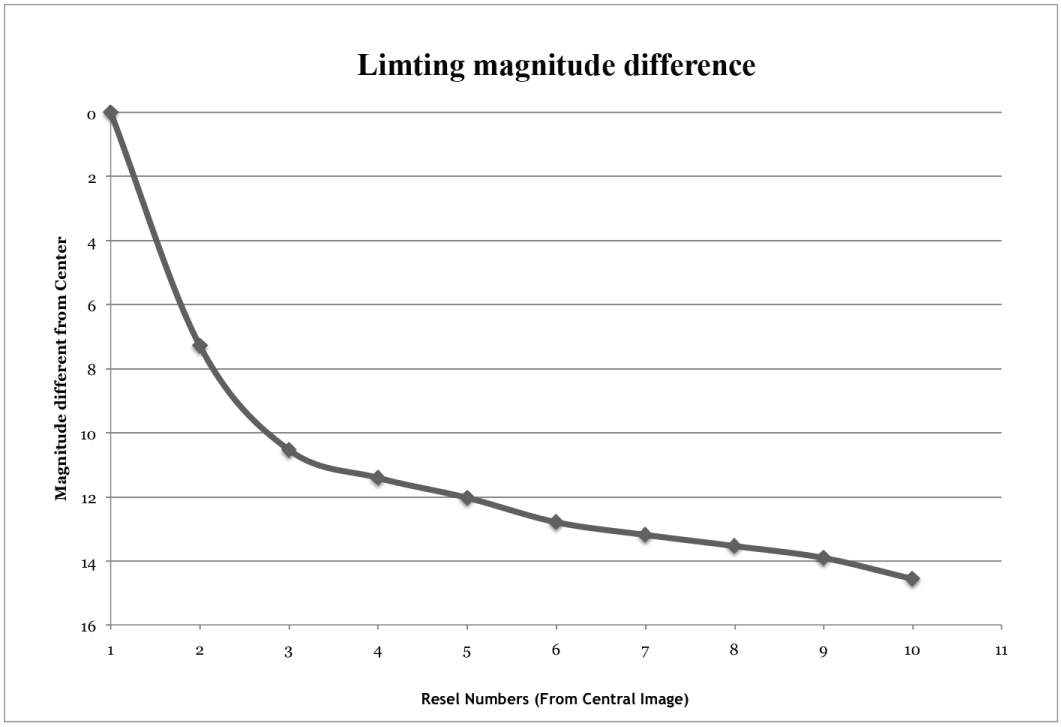

Figure 4.2: Maximum magnitude difference attainable at a given distance from the center of the PSF. (Obtained by sampling the numerically simulated PSF) similar to figure 3.10.

from different stages of evolutioni will be compared in order to demonstrate the performance of instrument at different and installation and optimization stages.

The first images from our Fresnel ground-based observation were acquired in July 2009. The images are validated according to the evolution stage of prototype. The results, which are presented in the following section, are referred to by their stage of optimisation.

4.3.1 Single star observation

This part shows images from single star observation. This type of targets will show strong spikes from the central star.

Category 0 : Field testing This catalog is not included in our priority but it was important images. It is a collection of our early targets that we observed to test optical alignment.

Vega As a test for the first light, we chose one of the brightest stars in summer,V= 0. Figure 4.3 was acquired with Fresnel 1.5.1 when we first installed and tuned the optical components.

Deneb The image of Deneb (V=1.2) shows noticeable energy in four orthogonal spikes from the central lobe. However, this energy in the spikes is not as high as we expected from the numerical simulation (Serre D., 2007)[20].

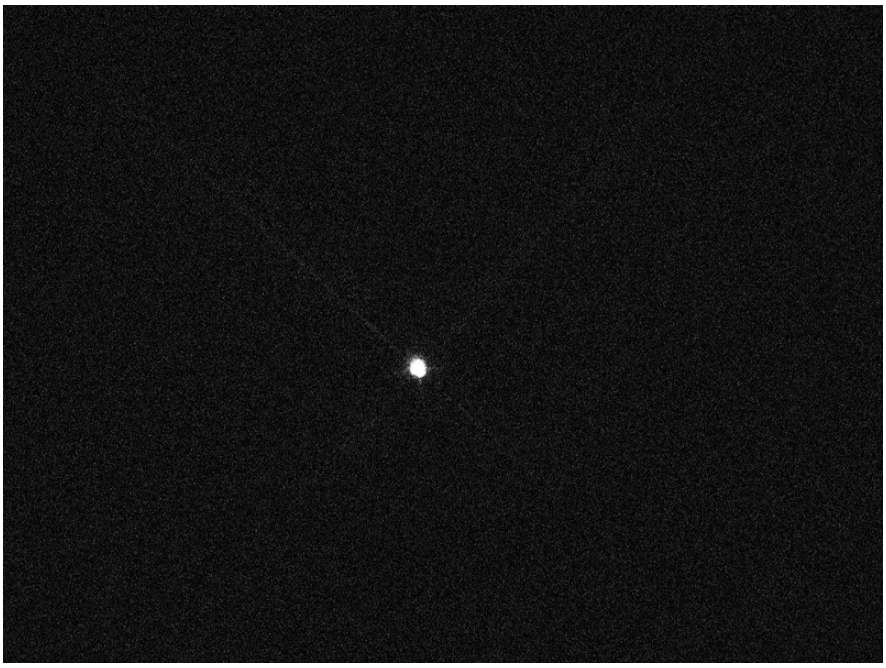

Figure 4.3: Vega at 100ms exposure time, from stage 1.5.1 Prototype

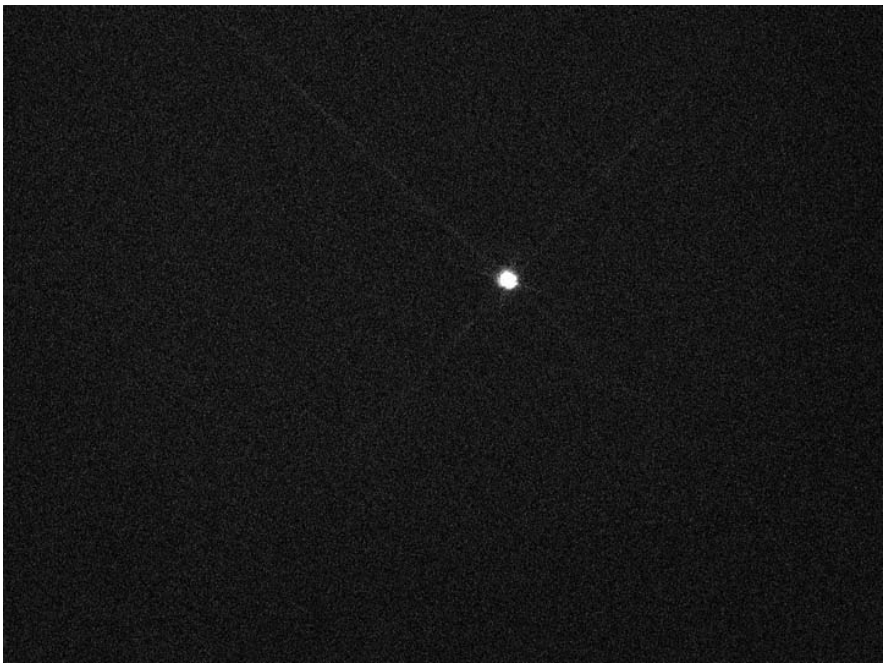

Figure 4.4: Deneb at 1s of exposure time, with no saturation

System		Magnitude	Separation
Alpherat		2.2	
BD+28 4B		11.8	138"

Table 4.2: Characteristics of α Andromedae and BD+28 4B, its neighbor

α Andromedae shown in figure 4.5, α Andromedae was observed in October 2009 with prototype 1.5.2. In the field of view, there is another star: BD+28 4B, which has a 9.6 magnitude difference at 138" separation. These are not a gravitationally linked couple.

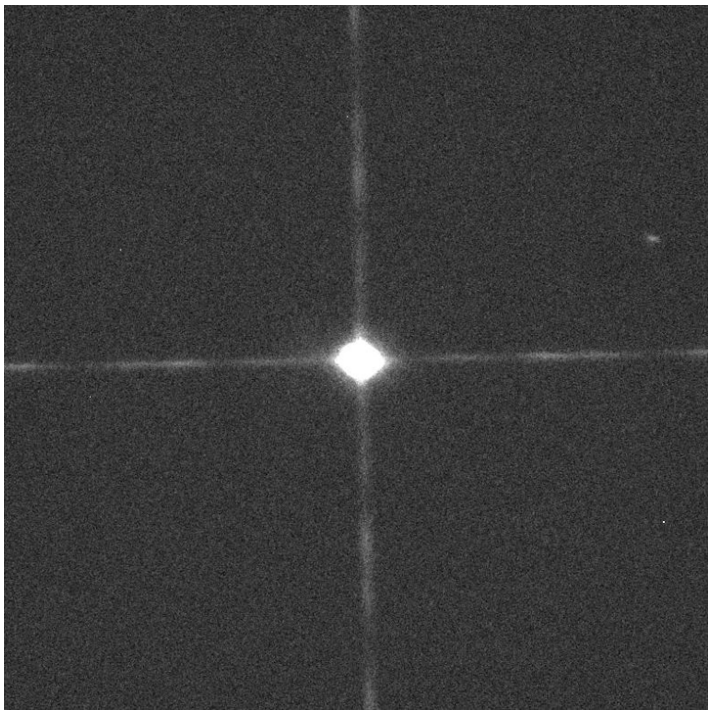

Figure 4.5: Image α Andromedae appearing with BD+28 4B separated by 138"

Category I : High Dynamic Range Targets

The first category of the dynamic range test targets that will be shown first are stars systems. It is multiple stars, which have at least a companion rotating around the central star itself.

4.3.2 multiple stars

υ Cyg or STT433 ABC is a triple star with companions at 15.3" and 21.8". Figure 4.6 and table 4.3 illustrate the dynamic range of Fresnel Imager 1.5.2. The spikes appearing in the image are stronger, due to the 300-seconds exposure time, which was used to catch the companion stars. In this image, the center of the PSF is saturated.

System		Magnitude	Separation
STT 433	A	4.4	
	B	10	15.3"
	C	9.9	21.8"

Table 4.3: Characteristics of triple star STT433 and its companions

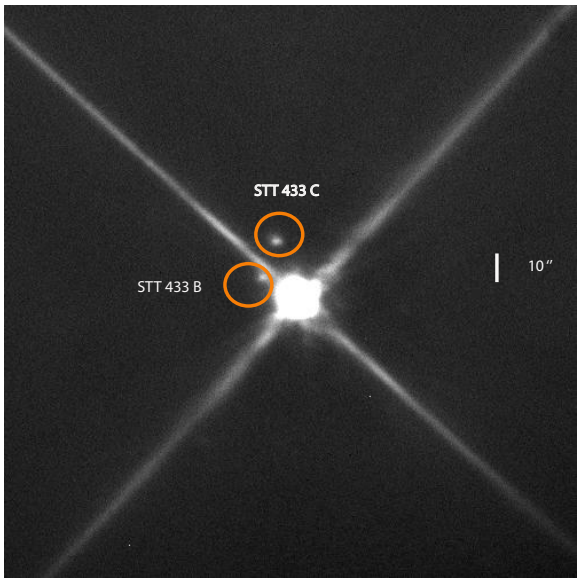

Figure 4.6: STT 433 and its companions B and C

System		Magnitude	Separation
STF2726	A	4.2	
	B	8.7	6.4"

Table 4.4: Characteristics of STF2726 binary system.

STF2726, also known as 52 Cyg is a binary system. It has a companion at 6.4" with a 4.5 magnitudes difference. We detected STF 2726 in July 2009 during the optimization of prototype 1.5.1. Figure 4.7 shows its image with a companion on the right. This image is a good example of spikes positioning by the rotation of the Fresnel arrays. As we position the spikes at 45 ° from the companion, the companion is in the highest dynamic ranges region of the PSF.

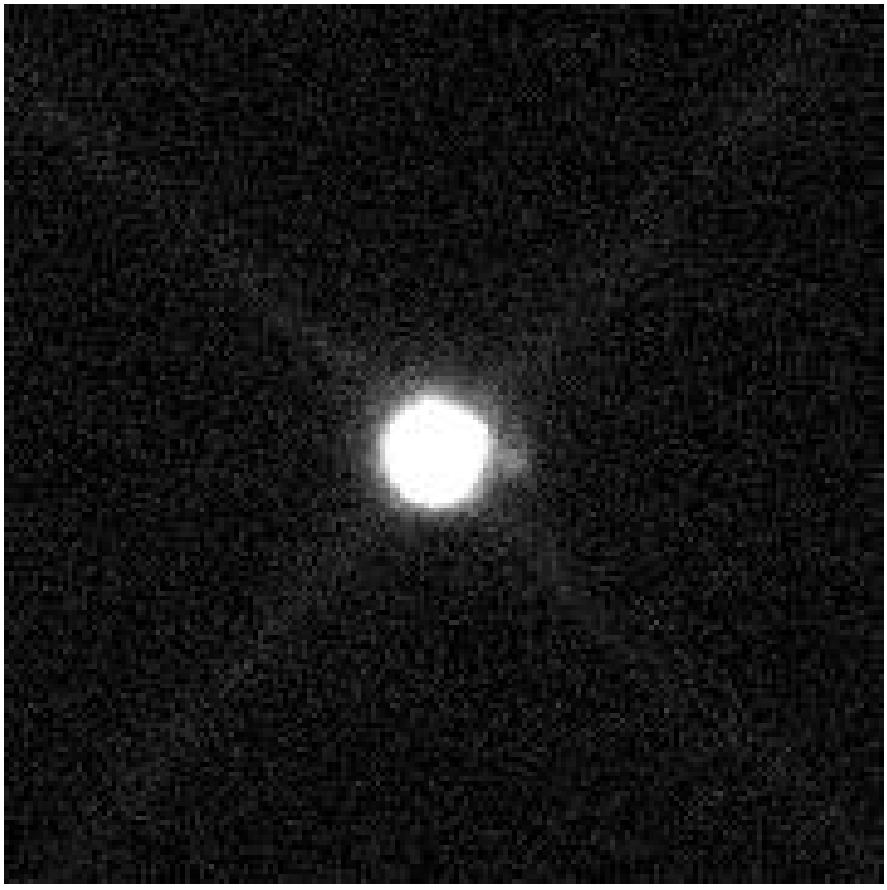

Figure 4.7: STF 2726, 52 Cygni

ϵ **Tri** ε Trianguli alias STF 201, was observed with prototype 1.5.2. Table 4.5 shows the characteristics of the stars.

BU496 BU 496 was observed in October 2009. It has a 6.8 magnitude central star and 12.8 companion at 5.7". It is observed with prototype generation 1.5.2.

System		Magnitude	Separation
Eps Tri	A	5.5	16pix
	B	11	4.7"

Table 4.5: Characteristics of ϵ Trianguli

Figure 4.8: STF201(ϵ Tri) and its companion, 5.5 ΔM at 4.7".

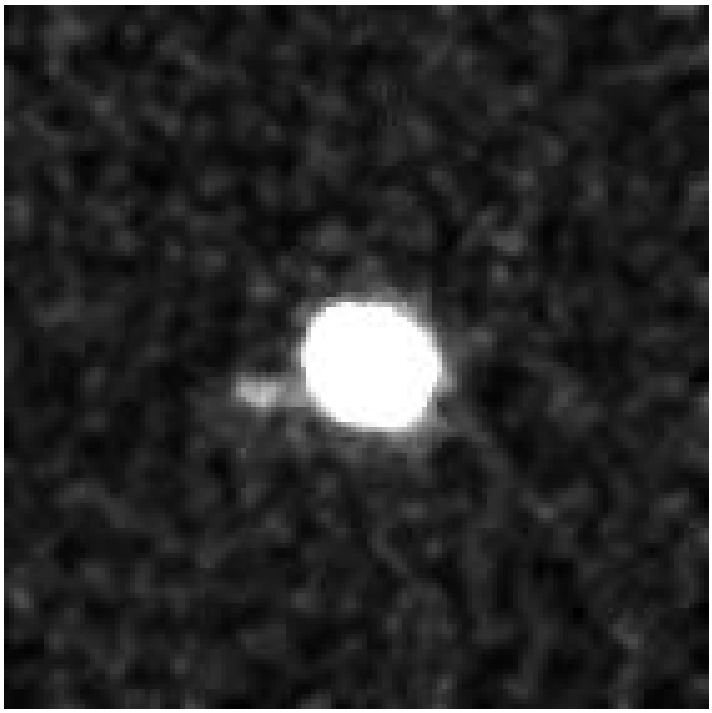

Figure 4.9: Image of BU496 showing a binary system with a 6 magnitudes difference between the central star and its companion. [From generation 1.5.2; 2 minute exposure time] Separation measured 5.7" and magnitude 6.8 and 12.8 in V. This is one of the first acquisition and there was some guilding problem.

System		Magnitude	Separation
ϵ 1	A	5.0	212"
	B	6.1	2.6"
ϵ 2	C	5.2	212"
	B	5.5	2.3"

Table 4.6: Characteristics of "double double star", ϵ *Lyr*

STF99AB φ Piscium is observed in prototype 1.5.2; 2 minute exposure time. It has a 4.7 V magnitude for the central star and 9.7 V magnitude companion at 7.5".

ϵ Lyr Observations that are made with ϵ *Lyr* are very important to illustrate improvement ϵ *Lyr* is a "Double-Double Star". All four stars are seen in figure 4.6. The two principal couples form a wide binary, which has a separation of 212". The separations between companions are 2.6" and 2.3" respectively, as shown in table 4.6. The separation of ϵ *Lyr* 2 can be distinguished easier than ϵ 1. This is due to the orientation of ϵ *Lyr* 1's couple, which is in the same direction residual chromatic abrasion due to misalignment of the corrective blazed lens.

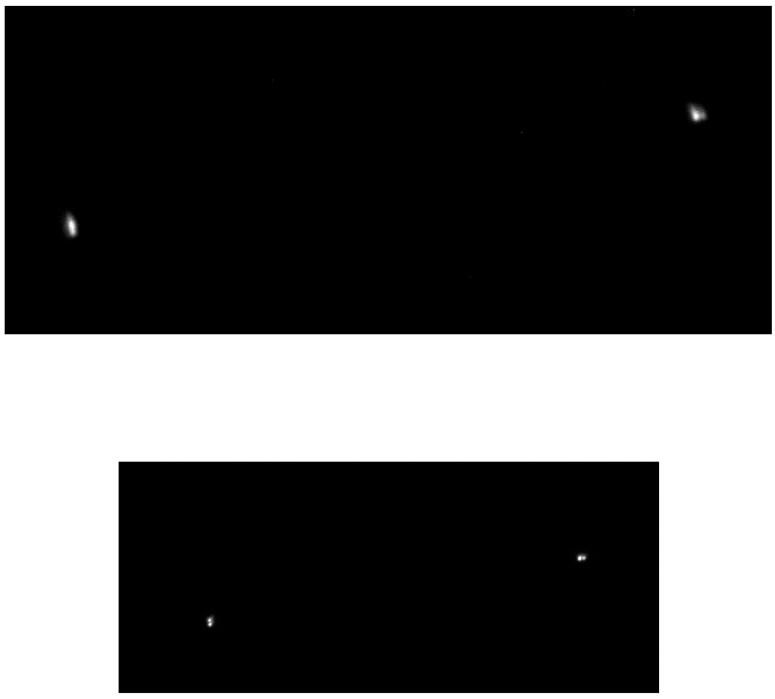

Figure 4.10: ϵ *Lyr* 1 and 2 and their companions form a Double Double System Top (a)Image from prototype 1.5.1, bottom (b) image from protyotype generation 2. One can see the improvement from generation I to generation II.

4.3.3 The Sirius binary star, companions A and B

Sirius is located in the constellation Canis Major. We can see Sirius with naked eyes in winter since the magnitude of Sirius A is bright: V = -1.47. However, there is a star; Sirius B, which is denser and has a higher temperature than Sirius A, to which it is gravitationally linked. Sirius B is much fainter than Sirius A and it cannot be seen with naked eyes. There are two reasons why it took such a long time to detect Sirius B. First, the luminosity of Sirius B is below the sensitivity of human eyes. Secondly, the angle of separation between those two is much smaller than human eyes resolution. It was first discovered in 1862 by Alvan Graham Clark, an American astronomer. He used a 47 cm telescope, which was the largest telescope at Dearborn Observatory at that time. To observe the companion star of Sirius A, the Fresnel Diffractive Imager must be able to overcome the high difference of luminosity between Sirius A and B with 200 mm of aperture and also manage a tight angular separation.

Characteristics

The characteristics of this binary system are the basic data that can help calculate and estimate the target's position on the graph in figure 4.2, i.e the magnitude difference($\triangle M$) and the apparent separation of its companions. Since the V magnitude of Sirius B is 8.3, there is a 9.7 $\triangle M$. It is a challenge to observe such an astrophysical target with a 200-mm aperture. From our dynamic range curve in figure 4.2, we study the limiting criterion of the targets, that make it possible for the Fresnel Imager to yield the results.

In theory, the Fresnel Imager can achieve $\triangle M = 10$ in the third resel at 3.4" in the diagonal from the central lobe of the PSF. Therefore, comparing to data in table 4.7, we suppose that it can possibly detect the companion star of Siruis A.

The Sirius data in table 4.8 are the objects' characteristics to use in a field test, such as stellar co-ordinates. It also shows orbital parameters for prevision of the companion's position in the field. The eccentricity (e= 0.591) and inclination (i=136.5) show that Sirius B has a non-circular orbit. Therefore, the angular separation will be different depending on observation time. The location of companion B has to be determined to estimate where it will appear in the field, so that we can adjust the spikes orientation accordingly to avoid masking it. The companion must not be hidden under one of the four spikes in the field, which is 3×10^{-3} times the brightness of the central star.

From the temperature listed table 4.7, the wavelength of the maximum brightness of the companion is far from our spectral band, estimated in band I (λ = 800nm). Then, magnitude of the stars will not correspond to the data listed.

Targets in field testing

The published data gives the distance and the orbital position of Sirius B with respect to Sirius A. Figure 4.11 shows the angular separation between Sirius A and B for the period of observation. This angular separation is superior to the angular resolution of the Fresnel Diffractive Imager, in theory: according to figure 4.11, the angular separation between Sirius A and B is 8.3" in 2010. As stated in the previous section, ρ = 0.8 ", we can determine that Sirius B will appear at 10^{th} resel, which is about a distance of 26 pixels from the central star. By the calculations leading to the curve in figure 4.2, the limiting magnitude difference at 10^{th} resel corresponds to a 14.5 magnitude. Therefore, we assume that we are able to observe

Sirius characteristics	A	B
Mass ($M_{\odot}$)	2.02	0.978
Radius ($R_{\odot}$)	1.711	0.0084 ± 3
Surface gravity (Log g)	4.33	8.57
Luminosity ($L_{\odot}$)	25.4	0.026
Apparent magnitude (V)	-1.47	8.30
Temperature (K)	9,940	25,200
Distance (pc)	2.64	
wavelength of the maximum brightness	291nm	116 nm

Table 4.7: Physical data of Sirius Binary System

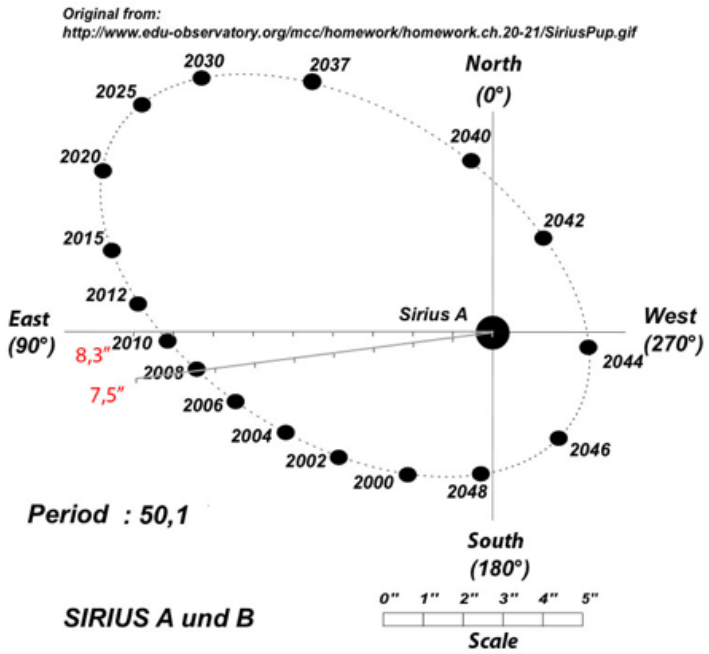

Figure 4.11: Relative orbit of Sirius B (Robert Burnham, Jr., 2000)[16]

Sirius orbital parameters	
Right ascension	06h 45m 08.9173s
Declination	-16 ° 42' , 58.017 "
Period (P)	50.09 year
Semimajor axis (a)	7.56 "
Eccentricity (e)	0.592
Inclination (i)	136.5

Table 4.8: Sirius binary System's orbital parameters.

Sirius B as the difference of magnitude is 9.76 in V and closes to 11 in I band, where we observe.

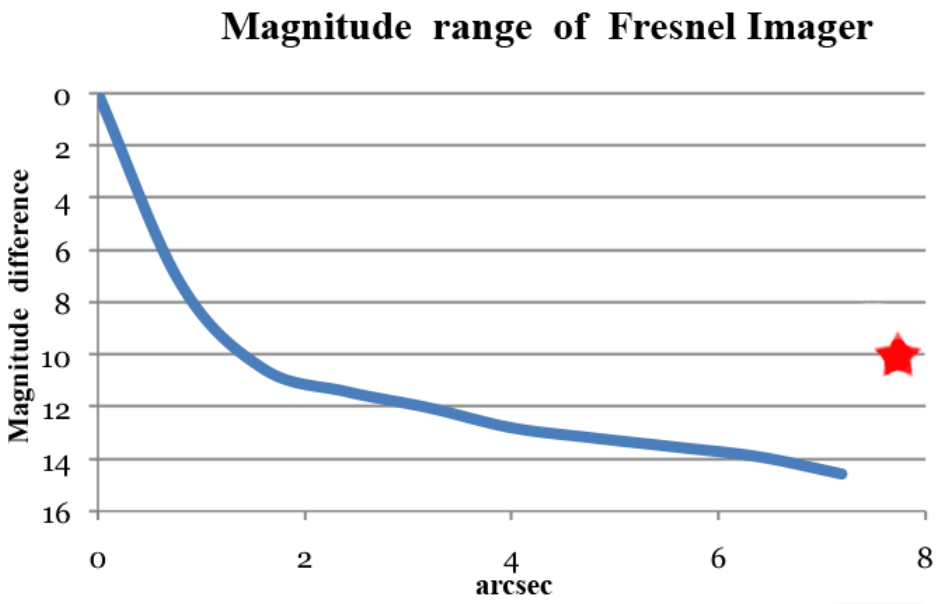

Figure 4.12: Sirius B relative position to Sirius A in a " separation versus dynamic range diagram

Observation

Sirius Sirius AB is our essential target that we expect to succeed in detecting. Sirius AB was first observed in I band (742 nm $<\lambda<$900nm) but we had no result from detection in this channel. This is the reason why we swapped our scientific channel and navigation channel. We observed again close to R band (630-740 nm) as we knew that in this band, there is a higher possibility for us to detect Sirius B (magnitude 10 in V band). In the result image shown in figure 4.13, Sirius A is in the center. At the lower right quadrant of image, Sirius B

appears near the central star. The diagonal, black lines are artifacts due to image subtraction of spikes from the array's orthogonal bars (as explained in the next section on Procyon). The position of Sirius B corresponds to where it is expected to be in the year 2010. This result shows that the Fresnel Imager can detect a 10 magnitudes differences at 8.5" separation.

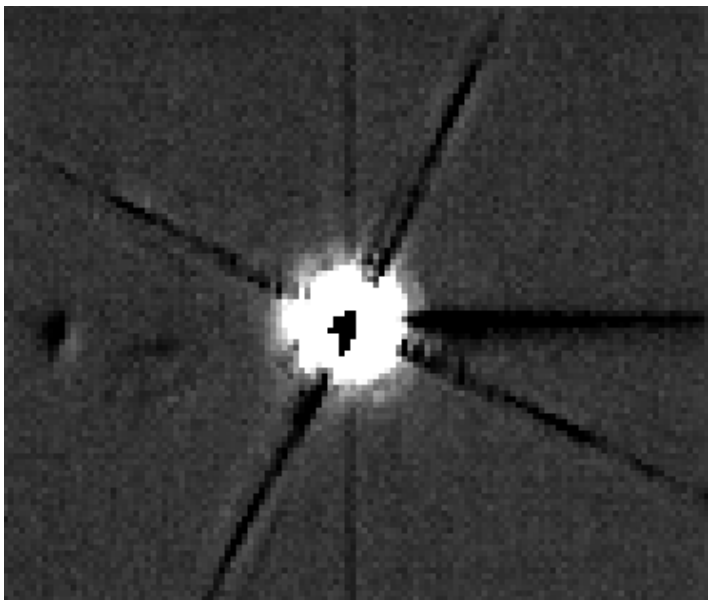

Figure 4.13: Sirius A is at the center of the image and the 10 magnitudes fainter (in R Band) Sirius B appears in the lower right quadrant near the center. The detection was achieved appears with 1000 composite images of 83ms exposure time on March 14, 2010 at 22:30.

4.3.4 The Procyon binary star, Companions A and B

Procyon shines from Canis Minor. This relatively young star is approximately 1.7 billion years old (Crosswell K., 2000)[2] (Eggenberger P., Carrier F. et al, 2005)[13]. It is the 14^{th} closest star system, located 3.5 pc away from our solar system, which is one reason for its brightness. Procyon binary system is composed of Procyon A and B, which travels in a 40-year orbit around Procyon A. Procyon B was observed by Bessel in 1844, Madler in 1851 and Dr. Auwers in 1861 to calculate its proper motion and confirm Procyon as a binary system (Isaac W., 1896)[24].

We can indicate that Procyon, as one of the targets of Fresnel observing runs, is a real challenge for the instrument. A difficulty in observing Procyon is its close orbit, 5" at apoastron. Unfortunately, in 2010 , Procyon B is in periastron, hence a 2" separation, shown in figure 4.14. The magnitude difference between Procyon A and B is 10.5 in V band and close to 12 in I band, as it is shown in table 4.10 and its close separation puts it on par with the limitation profile in figure 4.2.

Observation Images

Procyon was observed to test the magnitude differences limit. Initially, it was intended to observe the companion at 2" separation with 10 magnitudes difference in V band and more

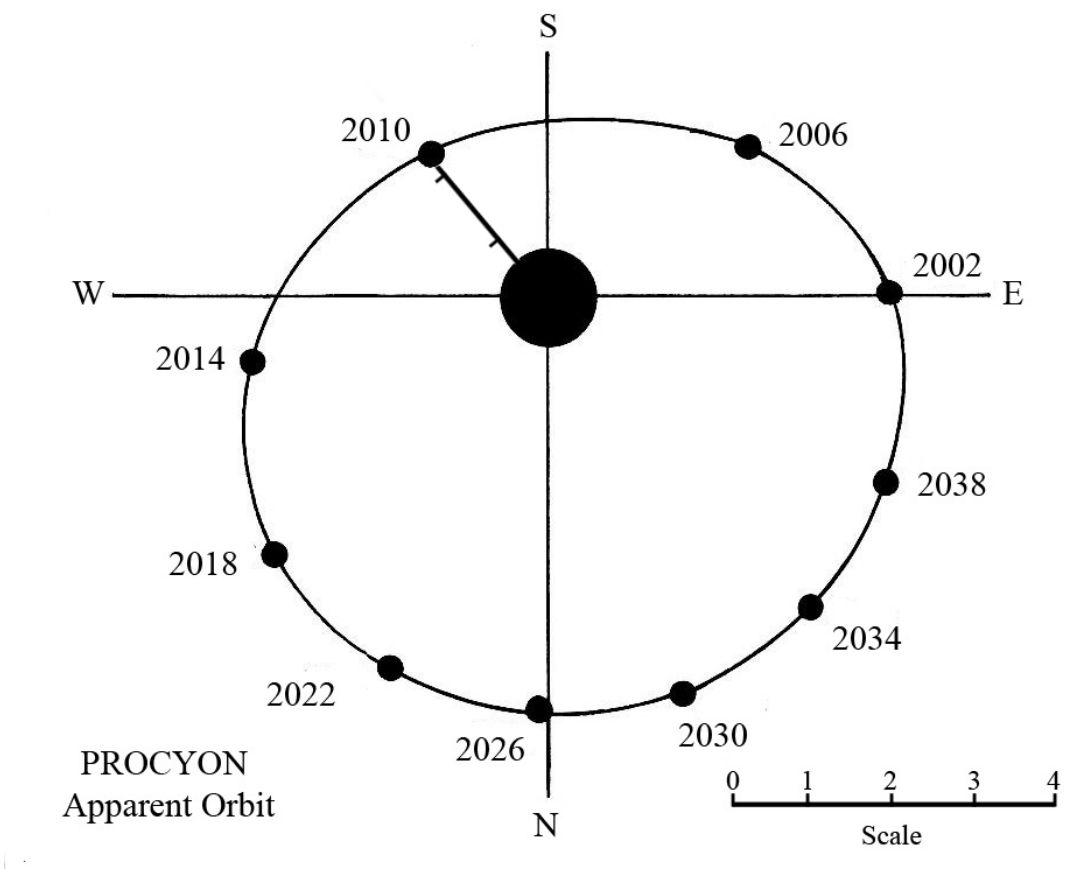

Figure 4.14: Procyon orbit during years 2002-2038 (scale in arcsecond)

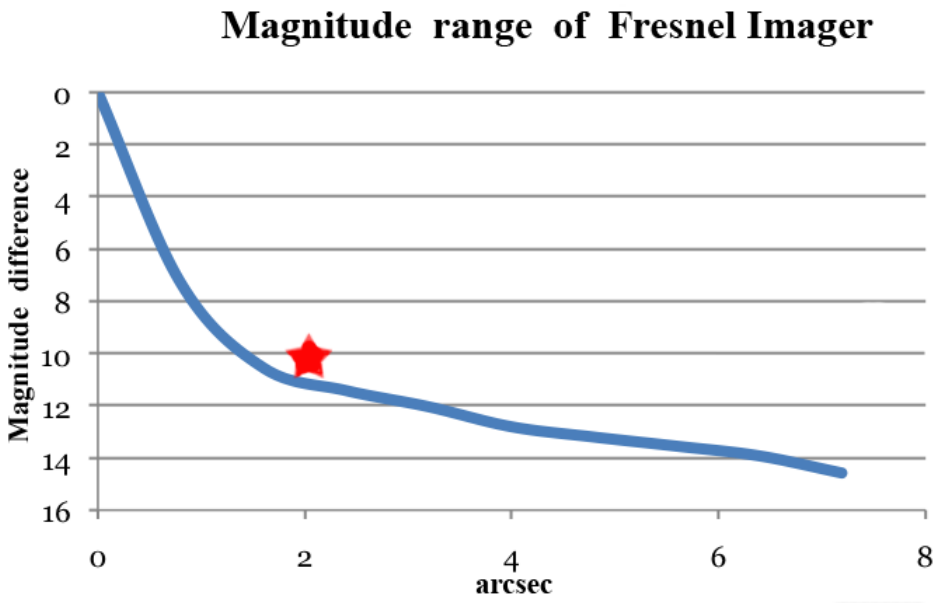

Figure 4.15: Procyon B relative position in arcsecond of separation versus dynamic range the solid line represents the limit achievable with prototype Gen II of Fresnel imager.

Procyon Stellar orientation parameters)	
Right ascension	07h 39m 18.1/17.7s
Declination	+05 13’ 29/20"
Period (P)	40.82 yr
Semimajor axis (a)	4.27"
Eccentricity (e)	0.41
Inclination (i)	31.9°

Table 4.9: Procyon Binary System stellar orientation parameters.

Procyon Characteristic	Procyon A	procyonB
Mass ($M_{\odot}$)	1.50	0.602 ± 0.015
Radius ($R_{\odot}$)	1.86	0.01234 ± 0.00032
Luminosity ($L_{\odot}$)	7.73	0.00055
Temperature (K)	6650	7740
Distance (pc)	3.496	
Apparent magnitude (V)	0.34	10.7(B) 10.92(V)

Table 4.10: Procyon Binary System data for use in observation.

in I band. At this state of observation, we were not able to notice any traces of companion B at 2" separation. Therefore, this star is afterwards used as a point source to create a PSF, shown in figure 4.16. The PSF of Procyon has been subtracted from the image of Sirius in order to reveal Sirius B.

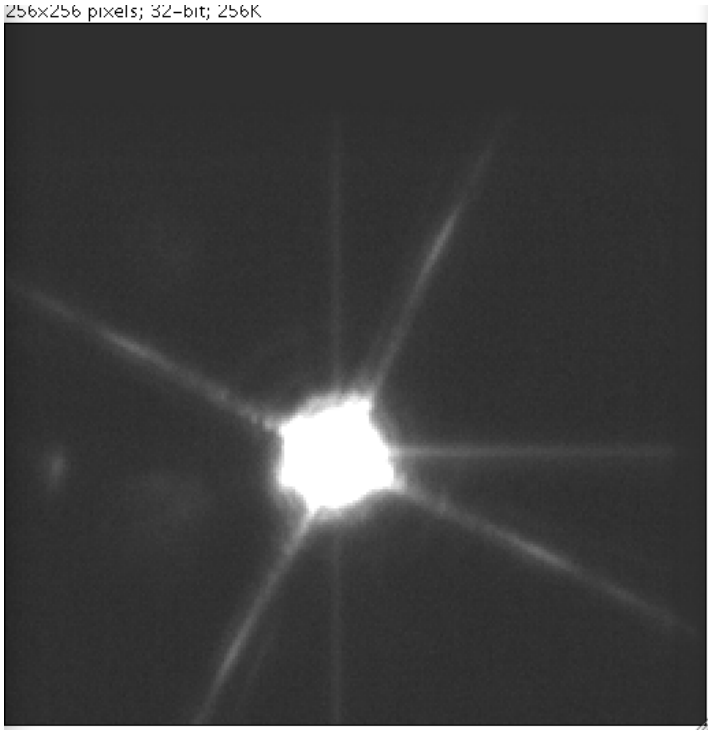

Figure 4.16: Procyon image by prototype generation 2, which consists of 25 composite exposures of 83ms on March 26, 2010 at 21:15

Category II : High Angular Resolution

4.3.5 Mars' Surface and Mars' Satellites

Mars has two satellites that we will observe for angular resolution and dynamic range tests. Mars' satellites were discovered in 1877 by Asaph Hall with a 66-cm telescope in Washington DC, US. There are two reasons why it is hard for us to detect the moons orbiting Mars. The first reason is that these moons are very small compared to the diameter of Mars. Phobos is 26 by 22 kilometers. Deimos is 15 by 12 kilometers. The small diameter directly affects the luminosity ratio. The second reason is their orbital radius: the distances between Mars and satellites are comparable to the radius of Mars itself (3,400 km). The orbital radius of Phobos is 9,378 kilometers and the orbital radius of Deimos is a little further at 23,459 kilometers. The orbital radius will affect the angular separation, which will be discussed below. These two reasons make it difficult for us to detect Mars' satellites from the ground with a 200-mm aperture, which, as far as we know, has never been done yet with such a small aperture.

Observation preparation

In the 2009-2010 opposition, the apparent diameter of Mars reached 14.11", which is about 4.5% of our field of view. The objectives of this observation are to validate the high dynamic range detection in the vicinity of bright extended objects such as Mars with a close separation Mars and its satellites. The preparation of this observation started with the calculation of a favourable observation period. For this, we used a published ephemeris to calculate apparent diameter and magnitude of Mars and its satellites from June 2009 to December 2010, see figure 4.17.

Then we calculated the luminosity of Phobos and Deimos from their ratio of diameters compared to Mars. The following calculation gives a quick estimate of the flux ratio between Mars and its satellites. The luminosity of Mars' satellites can be determined from the diameter ratio and albedo.

$$F_{Sat} = S_{Sat} \times \alpha_{Albedo} \times F_{Recived} \tag{4.3}$$

In this case, we assume that both Mars and its satellites receive the same illumination from the sun. Therefore, the luminosity of the satellites will be determined by

$$\frac{F_{Sat}}{F_{Mars}} = \frac{S_{Sat}}{S_{Mars}} \times \frac{\alpha_{Sat}}{\alpha_{Mars}} \tag{4.4}$$

where

$$\begin{aligned} F_{Sat} &= \text{Light flux from Satellite} \\ S_{Sat} &= \text{Surface of Satellite} \\ S_{Mars} &= \text{Surface of Mars} \\ \alpha_{Sat} &= \text{Albedo of Satellite} \\ \alpha_{Mars} &= \text{Albedo of Mars} \end{aligned}$$

$$\frac{F_{Sat}}{F_{Mars}} = (\frac{d_{Sat}}{d_{Mars}})^2 \times \frac{\alpha_{Sat}}{\alpha_{Mars}} \tag{4.5}$$

where

$$\begin{aligned} d_{Sat} &= \text{Diameter of Satellites} \\ d_{Mars} &= \text{Diameter of Mars} \end{aligned}$$

In the following, we define C as

$$C = \frac{F_{Sat}}{F_{Mars}}$$

The apparent magnitude, which is the magnitude that we can see from Earth, is defined by

$$m = -2.5 \log(\frac{F}{F_{Vega}}) \tag{4.6}$$

Then, in the case of Mars' satellites, from equation above we now have

$$m_{Sat} = -2.5 \log(\frac{F_{Sat}}{F_{Vega}}) \tag{4.7}$$

and then,

$$m_{Sat} = -2.5 \log(C \times \frac{F_{Mars}}{F_{Vega}}) \tag{4.8}$$

Finally, the difference in magnitude between Mars and one of its satellites can be expressed by

$$m_{Sat} - m_{Mars} = -2.5\log(C) \tag{4.9}$$

Consequently, we now can determine the magnitude of Phobos and Deimos compared to Mars.

From the given parameters above, the difference in magnitude between Mars and Phobos is 11, and 13 for Deimos. The angular separations of a planet and its satellites is determined by the ratios of the orbital radii to the distance of the observer. I started from the Strabourg CDS ephemeris giving the diameter of Mars as a function of time. I used it to calculate the distance between Mars and the Earth, then the angular separation of Phobos and Deimos as a function of time, see figure 4.17.

$$Angular_{Sep} = Distant_{Seperation} \times \frac{Angular_{Mars}}{Linear_{Mars}} \tag{4.10}$$

where

$Angular_{Sep}$ = angular separation of satellites
$Linear_{Mars}$ = diameter of Mars
$Angular_{Mars}$ = angular diameter of Mars

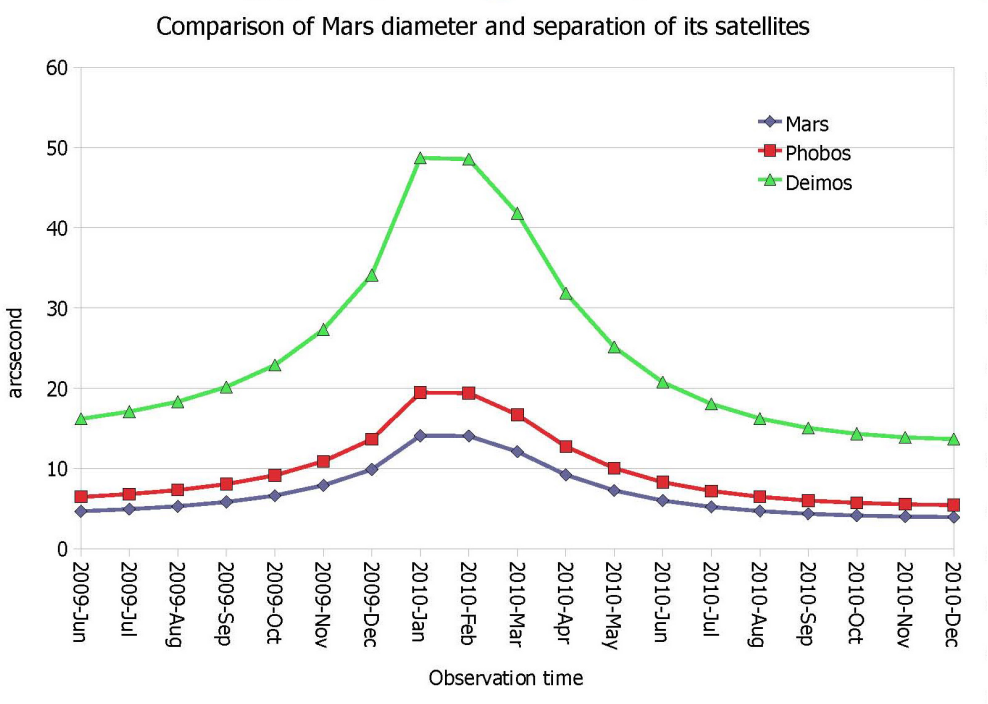

Figure 4.17: Angular diameter of Mars during the 2010 opposition and maximum angular separation of its satellites (Phobos and Deimos).

From figure 4.18, we can see that the maximum angular separations between Mars and Phobos is 22", and 74.1" for Deimos. According to the ephemeris of Mars, the largest angular diameter of Mars was on January 28, 2010.

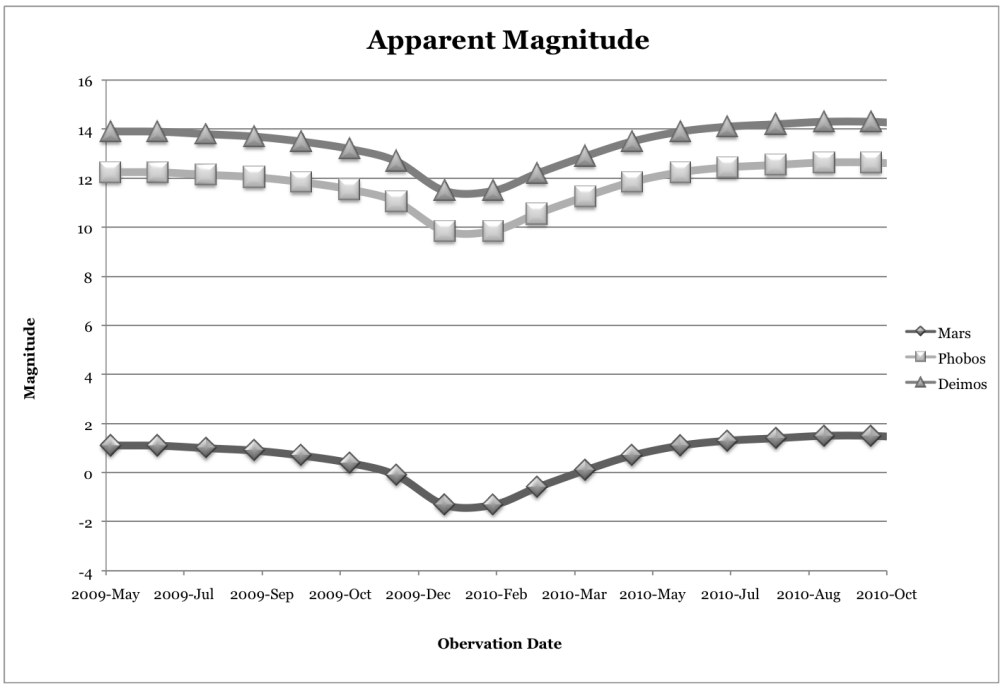

Figure 4.18: Apparent magnitude of Mars compared to its satellites

The period that gives the best result to observe Mars went from December, 3 2009 to March, 21 2010. In this period Mars started to exceed 10" in diameter and grew to 14.11" on January 28, then decreased to 10".

4.3.6 Extended object

Mars Image from prototype II We started observing Mars on January 17, 2010 to detect its satellites, Phobos and Demos. The image below is a sample of our detection which could not show the satellites. This image shown in figure 4.19 shows the detail of Mars' surface. This image is a full FOV from detector which shows the diameter of Mars at 13".

The observations of Mars satellites are shown in figure 4.20, which contains two images captured in time sequence. This figure shows that we can detect the satellites and observe their orbital motions. As the diameter of both satellites are small, the image just shows the satelletites as points in thier orbits. However, this demonstrates the the dynamic range and sensitivity of the instrument.

Category III : Sensitivity limit

4.3.7 M42 and θ Ori Trapazium

The Orion Nebula Messier 42, is chosen in order to determine the sensitivity of the instrument: to see details in the Nebula and the stars in the foreground.

The trapazium cluster was found in 1617 as multiple stars by Galileo Galilei. It is located in M42, one of the brightest largest Nebaulae in the sky. Their magnitude is shown in table

Satellites of Mars	Phobos	Deimos
Orbital Semi-major axis (km)	9378	23459
Orbital inclination (deg)	1.08	1.79
Orbital eccentricity	0.0151	0.0005
Major axis radius (km)	13.4	7.5
Median axis radius (km)	11.2	6.1
Minor axis radius (km)	9.2	5.2
Mass (10^{15} kg)	10.6	2.4
Mean density (kg/m3)	1900	1750
Geometric albedo	0.07	0.08

Table 4.11: Physical data of Mars and satellites

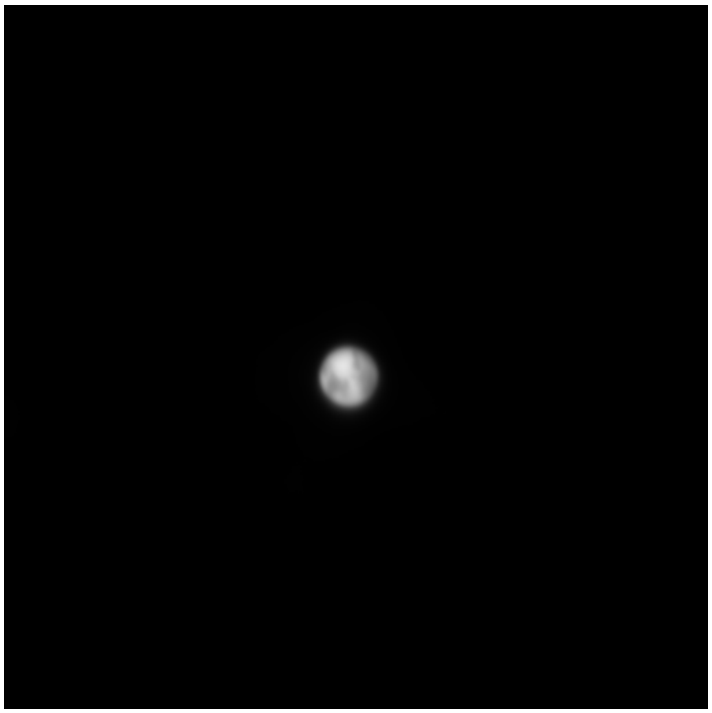

Figure 4.19: Mars image from Fresnel Imager prototype II, observed at 100 ms exposure time by prototype generation 2, filter 742 in front of the detector, on Febuary 13, 2010. The polar cap is on the right, details are visible on the disk/

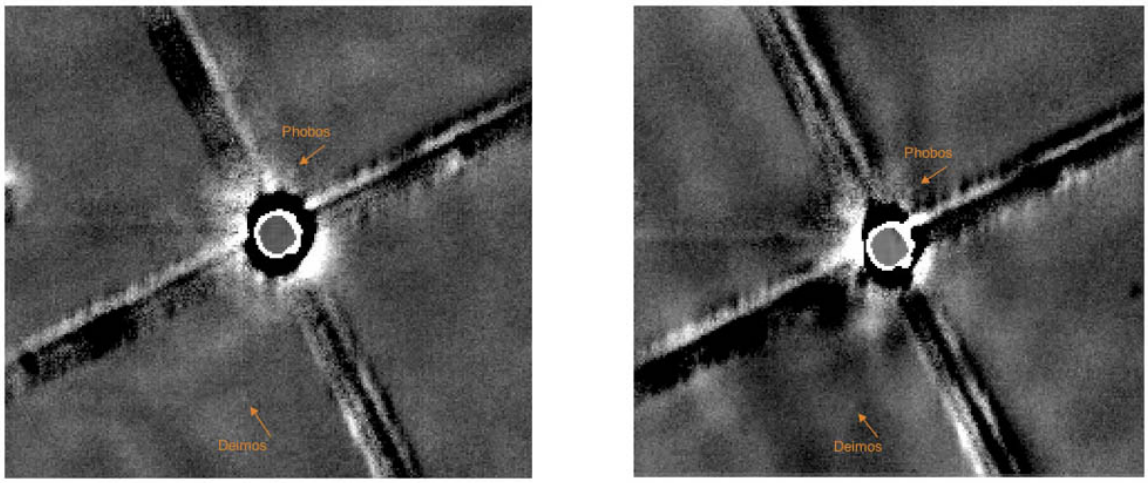

Figure 4.20: Satellites of Mars imaged from Fresnel Imager prototype II, these images are extracted from a sequence of 48 taken during two hours time, that show Phobos (above Mars) and Deimos (below of Mars), North is on the left.

4.12. The observation in M42 will demonstrate the capability of the Fresnel Imager for extended and faint objects.

Objects	magnitude
Θ1 Ori A	6.73
Θ1 Ori B	7.96
Θ1 Ori C	5.13
Θ1 Ori D	6.71

Table 4.12: V magnitude for the stars in M42 Trapezium

Fresnel observation In this image, we have 4 stars, each of which has a different magnitude close to 5. In the image, we see the sensitivity and limitation of dynamic ranges in Fresnel Imager. The nebula behind these stars in figure 4.22 shows the sensitivity of the instrument.

4.3.8 Extended Objects

Images of the moon Fresnel imager version 1.5.2 was used to observe the moon. Several pictures were taken on October 7, 2009. We observed the south eastern part of the moon, which is between the south of Mare Nectaris and the north of Janssen Highland. This part of the field shows many details of Reitha Valley and Rupes Altai mountain. A mosaic of two images on this field is displayed in figure 5.1.

The Moon This image of the moon was taken during our testing and optimizing sessions. It is not better than the ones taken with 1.5.2. It shows crater Tycho, 86 km of diameter. The

Figure 4.21: Orion and Trapazium, imaged by Laurent Koechlin with 50mm FD 2.0, exposure time: 5 minutes, Ektachrome 400 ASA. This image is here to show where the trapezium is located with regard to Orion constellation: in the middle of the M42 nebula; at the center of the field, which covers $20^\circ \times 30^\circ$ approximately.

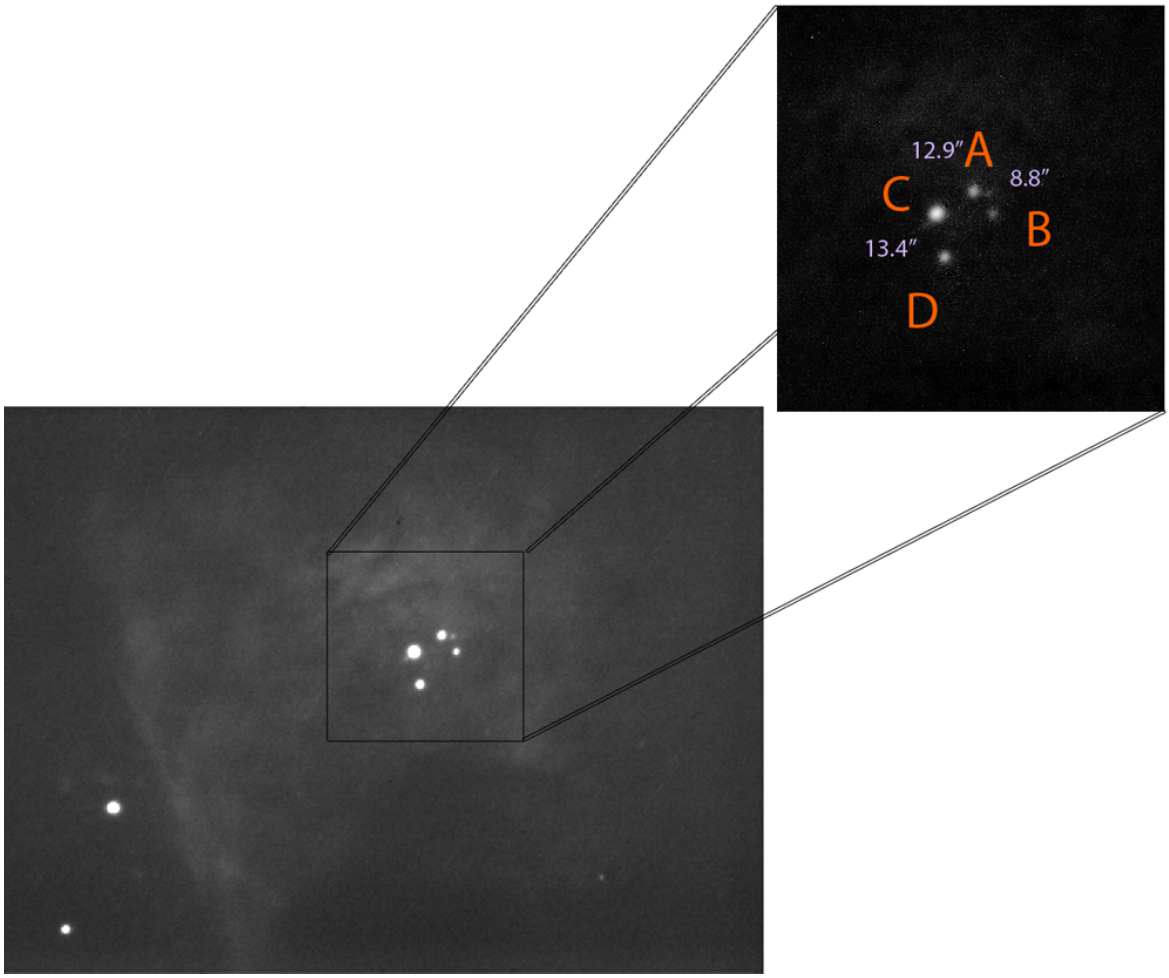

Figure 4.22: M42 Nebula and θ Orion Trapezium, composite of 43 images with a 10-second exposure time, process by shift and add with a code developed by Denis Serre.

field of view is 430 × 430 km.

Figure 4.23: Crater Tycho observed with Fresnel Imager generation 2 on Jan 27, 2010 at 23:03, taken at 180 ms exposure time with SXVH9 in band I.

Chapter 5

Instrument validation and Image analysis

After targets have been observed and images have been acquired, this chapter will give details in image analysis. The different prototypes have different specficications and performance. Hence, this chapter will show some aspects of the instrument before and after complete installation of version II, as well as a comparison of our preliminary studies and our results from observation.

5.1 Image analysis from prototype 1.5.1 and 1.5.2

To evaluate the specifications of the instrument, we calculate the performance from analysis of the images we acquired. Using equations from chapter 3, we control the sampling scale, determine the angular resolution and dynamic range from each observed target. We measure the sampling scale (R_{Samp}) of Fresnel by this equation:

$$R_{Samp} = \frac{D_{Ob}}{L_{px}} \tag{5.1}$$

where D_{Ob} is a distance or angle (diameter, separation) on the objects, and L_{px} is a separation in pixels in the image. Sampling scale will be expressed in "/pixel or km/pixel. The angular resolution is obtained by measuring the radius of the central lobe on unresolved or non - saturated stars. The dynamic range is determined by measuring the maximum brightness ratio obtained on different objects. The brightness ratio measured from our data may differ from that of the catalogues (Washington Double Star Catalogue)[1] as they do not correspond to the same wavelength band: we observed around 800 nm or 700 nm (I band) depending on the setting chosen, whereas our catalogue data corresponds to the V-Band (470-630 nm).

5.1.1 Optical characteristic analysis

Fresnel Imager 1.5.1 From the measured separation between the two binary systems (ϵ *Lyr* I-II), we determined our sampling scale. A measured value of 556 pixels for 212" of separation is given to equation 5.1 to calculate the sampling. As a result, we obtain 0.38" ± 0.02 per pixel. Other objects measurements are used to verify the sampling of Fresnel 1.5.1. ϵ *Lyr* 1 A and B are measured as 6 pixels for 2.4" but the separation is too small to give good precision . As a result, the sampling scale is 0.38 ± 0.003 (4 pixel error bar on the positions).

Object	52 Cyg			
	Companion			
	A	B	C	BG level
WDS catalog Magnitude	4.4	10	9.9	
Measured Intensity (ADU)	36964	1492	1394	338
Separation from WDS catalog(arcsec)		15.3	21.8	
Measured separation (px)		38.8	56.8	480
Sampling (arcsec/px)		0.4	0.4	
Exp time (s)	300			

Table 5.1: Measurements on data from triple star system, STT433 object

Object	52 Cyg, STF2726		
	Companion		
	A	B	BG level
WDS catalog Magnitude	4.7	8.7	
Measured Intensity (ADU)	42376	8892	4746
Separation from WDS catalog(arcsec)		6.4	
Measured separation (px)		16.7	480
Sampling (arcsec/px)		0.4	
Exp time(s)	300		

Table 5.2: Measurements on data from binary star system of STT2726

Angular separation of STT433 is determined from our previous measurement of sampling scale. They are shown in table 5.1.

Measurement of STF2726 is used to support our sampling scale evaluation. In addition, since STF2726 has a very close companion, we measured the largest dynamic range of at 6.4" separation, see Table 5.2. The small point on the left side of the image is a STF2726 B, which appears well in the image. The noise in the image may come from the long exposure with a Sony CCD Starslight SVXH9. In version II of prototype, the new CCD detector is more efficient.

A summary of measurements of ϵ *Lyr* is shown in table 5.3. The two binary systems are located at 212" separation, which has been described in the previous section. From all measurements and calculations of our image data, we determine a mean value of the sampling of Fresnel imager 1.5.1.; which is 0.4 arcsec per pixel. At the same time, we managed to acquire multiple stars' image of 4.5 magnitude difference in 4.4 arcsec. The specifications of a Fresnel imager 1.5.1 are displayed in table 5.4. This describes the specifications of a Fresnel imager in the state where it was when we observed the targets. The dynamic the range of the Fresnel imager is not determined as we have not got enough samples from this observation.

Fresnel Imager 1.5.2 With Fresnel Imager 1.5.2, we observed the surface of the moon. The composite image in figure 5.1 is from the south east of the moon, called Janssen (45S, 42E).[1] This south east highland of the moon contains main craters such as crater Janssen,

Object	Eps *Lyr*				
	ϵ*Lyr* I		ϵ *Lyr* II		BG level
	A	B	A	B	
WDS catalogMagnitude	5	6.1	5.2	5.5	
Measured Intensity	10035	7336	10303	9309	
Separation from WDS catalog (arcsec)		2.6	212	2.3	
Measured separation(px)		6.6	562	6	480
Sampling (arcsec/px)			0.38		
Exp time(s)	100				

Table 5.3: Measurements on data from double star system ϵ I-AB and II- AB

	arcsecond
One pixel	0.38
Total field of view at 1394×1040	556.8× 416

Table 5.4: Specifications of Fresnel imager generation 1.5.1 estimated sampling and field of view (FOV) with SONY SVXH detector.

with a diameter of 190 km, and Reita Valley which lies along a north-south axis for 500 km. This Janssen region is showed in the right of the image in figure 5.1.

In the top of the image, it is possible to discern Rupes Altai, which goes toward crater Piccolomini. This mountain is situated next to Rothman crater and is 480 km long in a north - south direction.

Measurements and calculations on the composite image of the moon in table 5.5 are made to find the sampling of Prototype 1.5.2. The mean value of all calculations gives a sampling scale, 0.77 km per pixel. This also means that the sampling is 0.42" at the surface of the moon, shown in table 5.6.

Crater	Diameter (km)	Distance (px)
Zagust	84	97
Rabbi Levi	81	106
Nicolai	41	53
Lindenau	53	74
Bush	54	72
Bushing	52	70

Table 5.5: Data and measurements of craters of the moon from figure 5.1

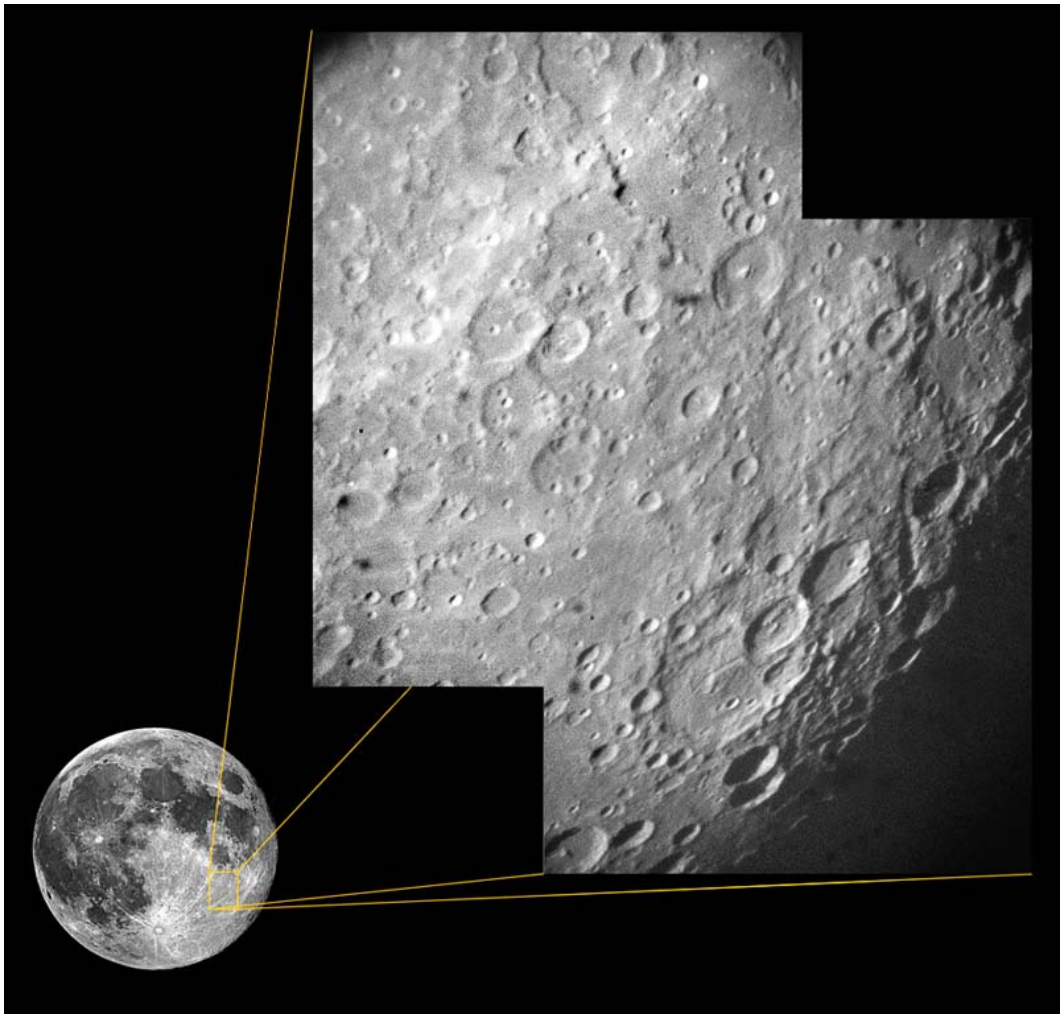

Figure 5.1: Composite of two images covering 1,155 × 986 km on the moon, taken by generation 1.5.2, 200ms exposure time. [Oct, 7 2009 at 3:03 am]

Pixel	0.42"
Pixel	0.77 km (at the surface of the moon)
Field of view	584× 436 "
Field of view	9.7 × 7.3 arcmin

Table 5.6: Specifications of FDIAs 1.5.2 estimated sampling and field of view (FOV) of SONY SVXH detector at 1392×1040 pixels

5.2 Image analysis from prototype II

After complete installation, the Fresnel imager has observed targets that have been described in previous chapters. Targets in three categories have validated high dynamic range (Sirius), high angular resolution (Phobos and Diemos) and high sensitivity (Orion-M42). As I described in preparation of observation of each target, the instrument is capable of detecting a binary objects, which have Δm = 8 i.e $10^{3.2}$ at 5 resel from central lobe. At 18 resels, we reach Δ m = 15 i.e.(10^6).

5.2.1 Summary of Validation of Fresnel imager on ground-based prototype

The Fresnel Imager prototypes for ground-based observation, which ran from generation 1.5 to 2, have been improved by the successive installation of new equipment. The dynamic range and angular resolution are enhanced and get close to the performance curve of prototype generation II, summarized in figure 5.2. This curve is obtained from a numerically simulated PSF and displays the dynamic range as a function of angular separation, to compare the potential of Fresnel observation results to the theoretical calculation.

The results from all three generations are summarized by the observed targets plotted in figure 5.2. The *red* dots are the stars we observed in July and September 2009 plotted according to the angular separation and differences of magnitude. It shows the results from generation 1.5, the blue spots are the targets that we detected with generation 2. These are located below the red group from generation 1.5. The last group is a green star, for which we cannot detect the companion: Procyon.

From figure 5.2, in prototype generation 1.5.1 we reach a 5.5 magnitudes difference at 6" separation, whereas it should reach 12 according to the numerically simulation curve. This discrepancy may come from the turbulence and our uncompleted installation prototype. Fresnel 1.5.1, nonetheless, achieved the detection of a 2.2" separation in ϵ *Lyr* AB.

With generation 1.5.2, we observed the moon, shown in figure 5.1. This picture of the surface of the moon almost reaches an angular resolution, of 0.8 " as we can detect several craters as small as 3 km, corresponding to 2". Detecting a2" crater requires at least a 1" resolution. The full specifications of the Fresnel imager are not reached at this stage 1.5.2.

In Fresnel prototype generation 2, we tested the instrument on difficult targets, as described previously. It is able to detect the binary star Sirius AB, which has a 8" separation and 10 magnitudes difference. This is remarkable for a 200 $\times$ 200mm aperture instrument. For Procyon, we were not able to observe the companion as the instrument cannot reach a 12 magnitudes difference at 2" separation; (see figure 5.2). Other targets that we observed, such as M42 and the moon, show the sensitivity and the potential of detection.

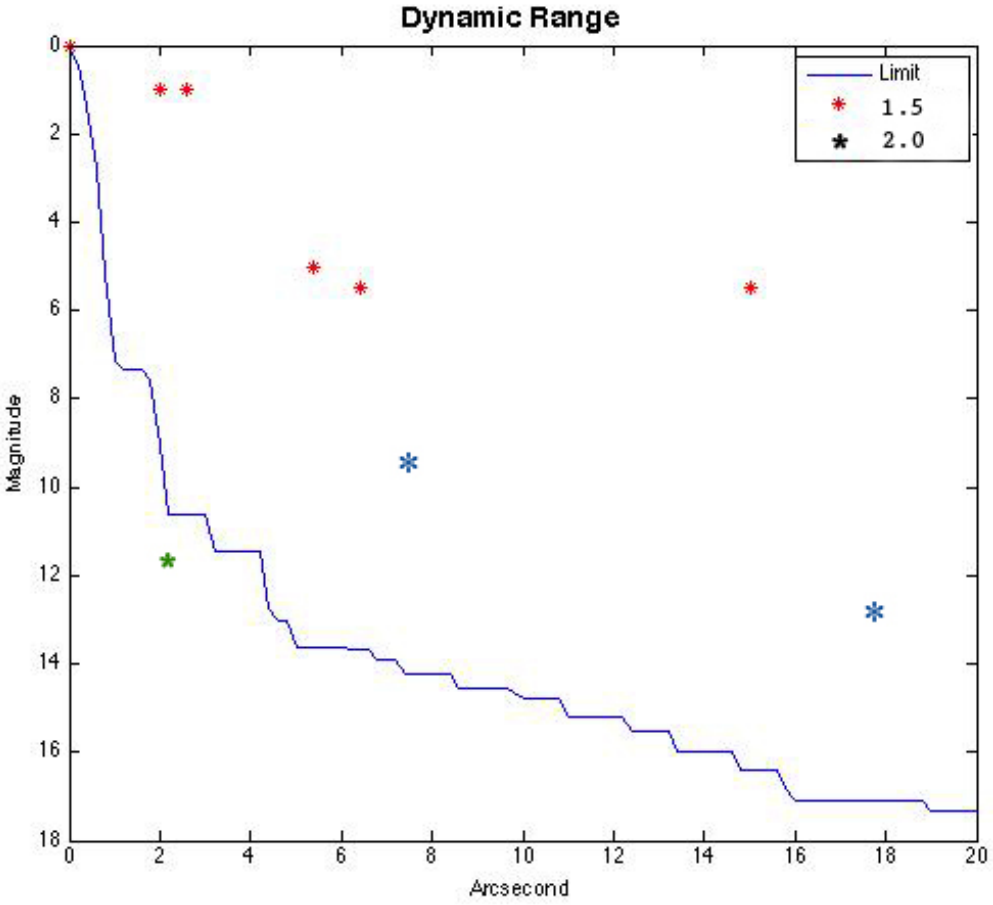

Figure 5.2: The curve corresponds to the limiting magnitude difference as a function of the angular separation. It is obtained from the PSF of the Fresnel Imager, compared to observed results from prototypes 1.5.1 and 1.5.2 and 2.0. The *red* stars are results from prototype generation 1.5.1 and 1.5.2. The results from a complete prototype generation 2 are shown as the *blue* stars. The green one below the curve is Procyon, for which the companion is not detected.

Chapter 6

Fresnel Imager for space mission

The Fresnel imager benefits from high angular resolution in space, by operating at short wavelengths, as it has a wavelength-dependent resolution. This advantage of Fresnel imager in the Ultra-Violet (UV) domain can be an impact to many applications. The Fresnel Diffractive Imagery Array in UV can cover from 300 to 120 nm wavelegnths. The upper limit is due to the configuration of the FDIA but can be expanded and the lower limit is due to the difficulty of long-distance focalisation of the Fresnel imager.

This chapter describes the advantages of the Fresnel array and its capability in the UV applications. It will mainly focus on the observation of accretion disks. This chapter will use a model to simulate images of young stars accretion disks as seen by a Fresnel imager.

6.1 Objects observed or detected in the UV

High-energy sources such as the high-temperature surfaces of young stars and their evolution, create high-energy particles and radiation, some of which can be detected in the UV. With the collaboration of the Network for UltraViolet Astrophysics (NUVA), we studied the potential of the Fresnel imager for the study of scattering disks in young stars, and for a UV space mission. An advantage of the Fresnel Imager is that its angular resolution increases at short wavelengths, applications in UV can thus lead to high angular resolution. The objects of interest that we will discuss in this chapter are interstellar disks, their evolution and light scattering.

6.1.1 Scattering in space observation

Light scattering by dust grains in the universe can be found in any region since dust is generated by various processes in space. Dust grains come from solidification of heavy elements like silica, carbon, etc. generated during late evolution phases of stars that have since blown out their outer layers during their last evolution stages. Therefore, dust in the universe can be detected in the star forming regions. Scattering plays an important role around many observation targets.

For example, in figure 6.1. HH30, which is detected by Hubble Space Telescope, shows an illuminated dust disk around the protostar. This image also shows the jets, which are not included in model. The matter surrounding the nucleus is a mixture of dust and ionized gas [3] and it has a complex structure, which is not well known in physics today. A dust grain

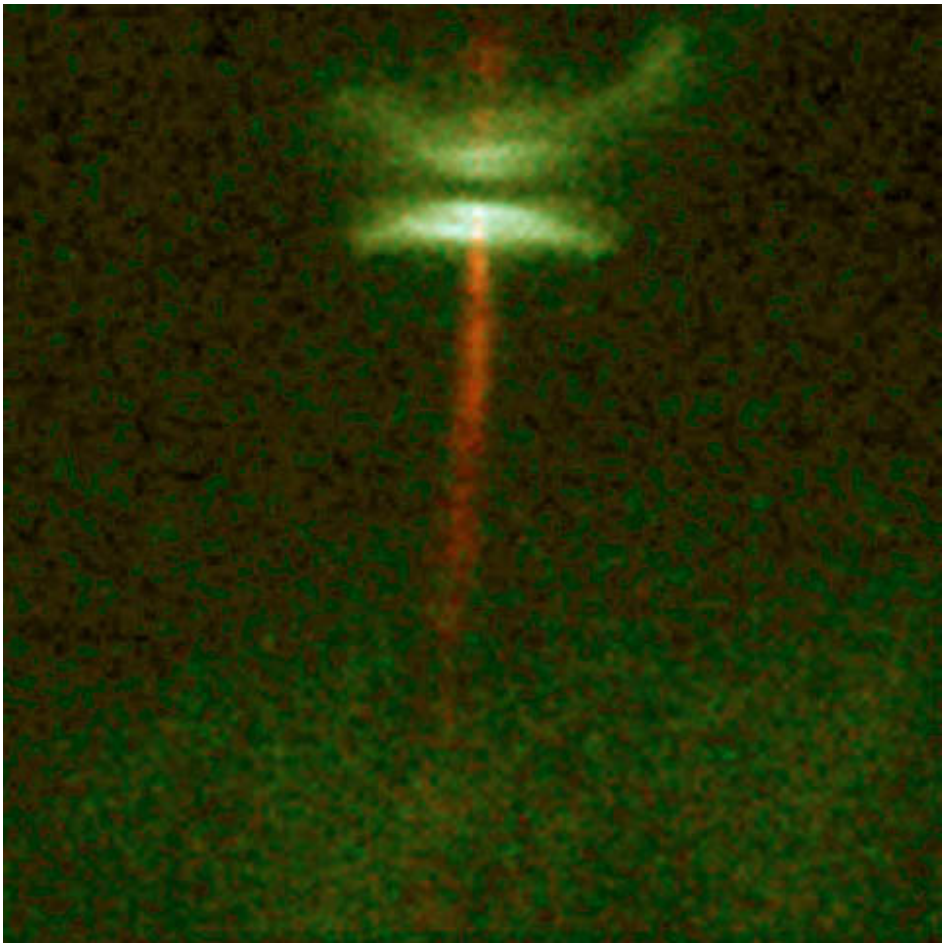

Figure 6.1: HH30 Accretion disk, observed by Hubble Space Telescope, Courtesy of NASA, JPL

can interact with electromagnetic radiation, either by absorption, polarization, emission and scattering. Dust scattering depends on the size and shape of the dust grain as well as the material contained inside, which is not taken into account in our simulation.

In this section, we will only deal with the scattering effect of dust particles. It will be modelled, to be used as a simulated input image of the Fresnel imager. Here, we will concentrate on the result image of the dust accretion disk as detected by the Fresnel Imager. Therefore, we do not need an elaborate model; we based ours on Hayashi (1981).

6.2 Methods

Accretion disks around young stars are studied since this can help us understand the origin of planetary systems. Here, we investigate on accretion disks that are usually found around young stars. With gravitational collapse of the molecular cloud into its core, disks will be aggregating and densifying due to the angular momentum and gravitational collapse. A fraction of the initial mass will fall into a disk around it, not forming the protostar [Terebey et al, 1984: Yorke et al., 1993: Dullemond et al., 2003]. Radiation from central star heats the gas and dust in the disks.

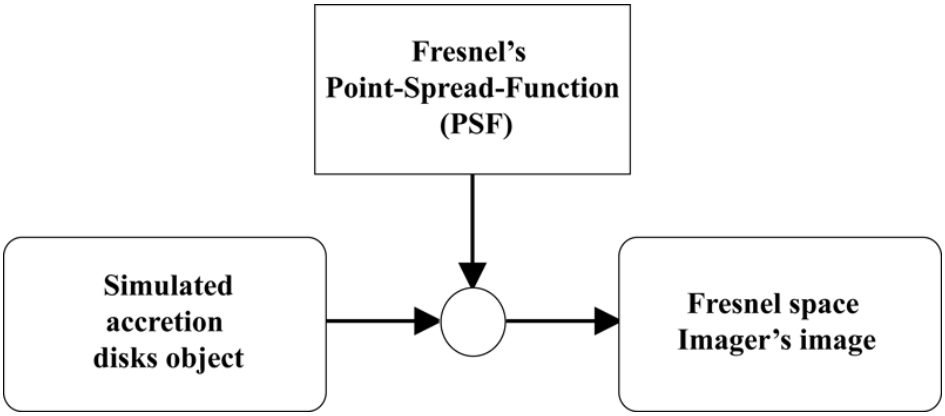

Figure 6.2: Fresnel's accretion disk simulation processes

Accretion disks type objects can be observed in the Ultra-Violet when high energy from the center travels through the dust and gas in the disks. Radiations are scattered by dust grains into our line of sight. Scattering light from dust grain can be observed in Ultra-Violet as dust grains have a micron scale radius ($r_{dg} \simeq 0.5\ \mu$) [Throop and Bally, 2005].

6.2.1 Disks Model

The physical and chemical model of disks we use are described in (Dullemond C.et al, 2003)[4] and Hayashi (1981). These models of protostellar disks assume that compounds of dust and gas are rotating around stars. Disks vary in shape and ingredients. The age of disks will define their composition, size and shape. The inner and outer radii are repectively, R_{in} = 0.2 AU R_{out} = 400 AU (Hersant F. et al, 2005)[9] and $M_{star} = M_{\odot}$ (Henry B. Throop, 2001)[23]. Disks are illuminated by UV radiation from the central star with an intensity L_{star} = $5L_{\odot}$. We neglect the chemical components in dust grains to simplify the scattering pattern

in the model. However, the shape of disks and dust density profile depends on the dust and gas mixture ratio.

Vertical Gas density Distribution

This model is from (Hayashi C., 1981)[7], (Hayashi C.,1985)[6]. It gives the vertical gas distribution as

$$\rho_g = \rho_{g0} \exp -(z/H)^2 \left[g/cm^3\right] \tag{6.1}$$

where ρ_{g0} is a gas density in the mid-plane of disks and H is the vertical scale height.

Vertical Scale Height

The vertical Scale Height(Sekiya M., 1988)[17] can be expressed as

$$H = \left[\frac{2r^3 kT}{GM_{\odot}m}\right]^{\frac{1}{2}} [cm] \tag{6.2}$$

To simulate a thin accretion disk, we follow [Tanigawa, 2004]:

$$\frac{H}{r} \propto r^{\frac{1}{4}} \tag{6.3}$$

Assuming the mean molecular weight of the solar nebular to be equal to 2.34, we get:

$$H = 7.1 \times 10^{11}\left[\frac{r}{AU}\right]^{\frac{5}{4}} [cm] \tag{6.4}$$

where r is the distance to the center of the disk, measured in the equatorial plane of this disk.

Column Density of gas and dust

In the present model of dust around a central star, the column density profile of the gas and dust are expressed by Σ_g and Σ_g respectively.

$$\Sigma_g = 1700\left[\frac{r}{AU}\right]^{-\frac{3}{2}} \left[g/cm^2\right] \tag{6.5}$$

$$\Sigma_d = 1.7\left[\frac{r}{AU}\right]^{-\frac{3}{2}} \left[g/cm^2\right] \tag{6.6}$$

We set the parameters between dust and gas density as

$$\frac{\Sigma_g}{\Sigma_d} \simeq 100 \tag{6.7}$$

6.2.2 Dust and Scattered light

In this section, we consider only scattering from dust particles. Scattered light from a dust grain is described as follows. First, the dust grain, containing electric charges, is excited by

incident light. Figure 6.3 shows that after the incident light illuminates the dust particle, the light is scattered in all directions with variable amplitude according to Henyey-Greenstein (Henyey-Greenstein, 1941)[8].

An observer who is placed far from the object will detect the scattering light coming into his line of sight. This dust scattering light builds the projected image at the observer's position.

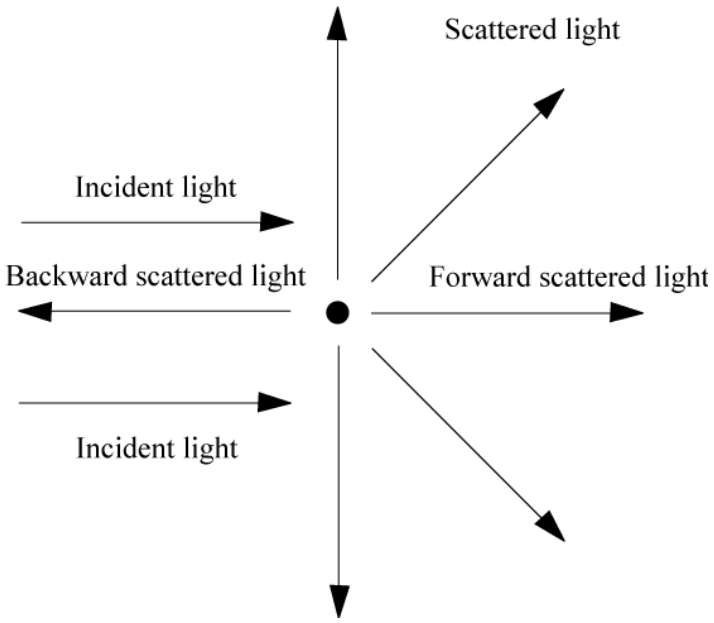

Figure 6.3: Light scattering diagram, describing scattering direction: backward scattering (g<0) and forward scattering (g>0).

Figure 6.4 illustrates the angle of scattered light. The dust grain is illuminated by the central star, placed at p(0,0,0). At p(x,y,z) locating a dust grain at a certain distance(r), light scattered by dust will travel into the line of sight of an observer with angle θ relatively to the incident direction. In this case, the observer captures the image in a plane perpendicular to the line of sight.

The scattering involves the relation between incident and scattered light intensities as a function of angle. It can be described by the Henyey-Greenstein phase function (Henyey-Greenstein, 1941)[8]. This equation describes the angular distribution of scattered light.

$$\phi(\theta) = \frac{1 - g^2}{4\pi \times (1 + g^2 - 2gcos\theta)^{3/2}} \tag{6.8}$$

where g is the anisotropy factor for forward and backward scattering.

The parameter "g" is referred to as the scattering phase function asymmetry and varies from -1 (complete back scattering), 0 (isotropic scattering) to 1 (complete forward scattering). The projected images of disks are varied, depending on g parameter. The value of g strongly influences the apparent shape of disks. In our case, we use $g \approx 0.6$.

In figure 6.4, incident energy is absorbed at the dust particle and scattered at θ : the angle between incident and scattered directions. Figure 6.4 illustrates the direction of scattered light by dust at radius R and send into the line of sight, to the detector plane.

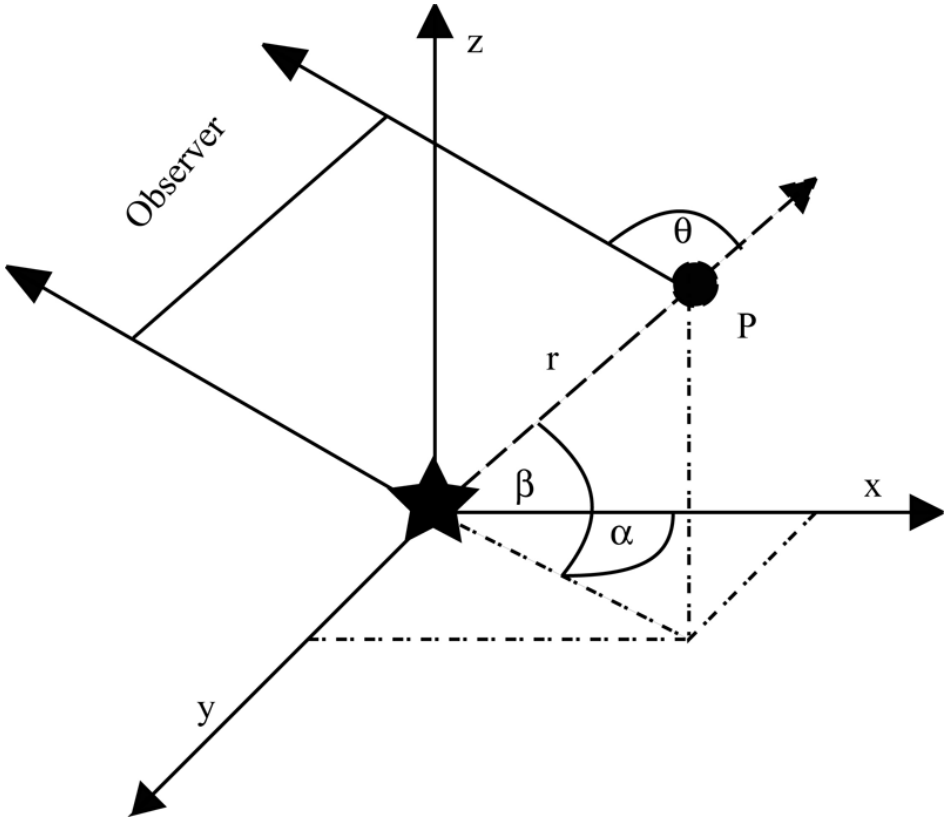

Figure 6.4: The dust grain is illuminated by the central star, placed at p(0,0,0). At p(x,y,z) locating a dust grain at a certain distance(r), light scattered by dust will travel into the line of sight of an observer with angle θ relatively to the incident direction. In this case, the observer captures the image at direction Y with a plane perpendicular to the axis

$$\cos\theta = \sin\beta \cdot \sin\gamma + \cos\beta \cdot \cos\gamma \cdot \sin\alpha \tag{6.9}$$

$\cos\theta$ can also be obtained by the inner product of dust grain position vector (relative to the star) and the observer direction vector.

$$\tan\alpha = \frac{r_x}{r_y} \tag{6.10}$$

$$\tan\beta = \frac{r_z}{r_{xy}} \tag{6.11}$$

The simulation is based from a model of the dust grains position, which are located in a thick disk volume, at distances r from the central protostar where r is such as $[R_{in} < r < R_{out}]$. The simulation calculates the scattering angle and scattered light intensity corresponding to the dust grains' location. Then, we calculates the projection from this scattered light intensity from each dust grains to the observer. Figure 6.5 shows the flowchart for the calculation of scattered light from dust grain in 3 dimensions. The angle of scattering is calculated by equation 6.9 where the dust disk plane contains the x and y axes.

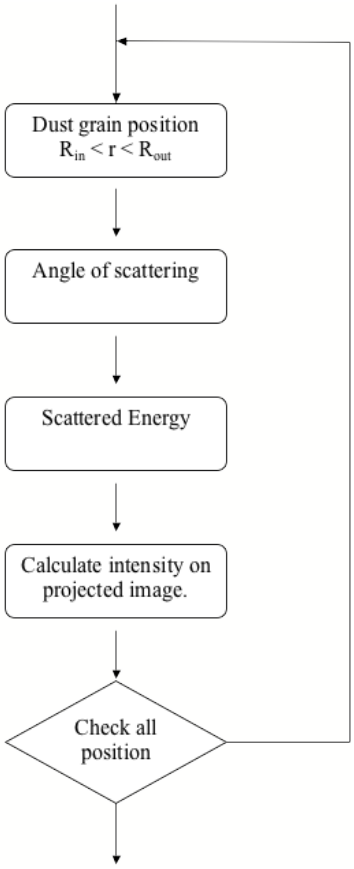

Figure 6.5: Accretion disks simulation flow chart.

This simulation is a projection of 3D accretion disks onto a phase perpendicular to the line of sight. We construct a 3-dimension model of the scattered light from a grain around the protostar following the equations in section 6.2.1. The distance where we put the protostar

will determine the linear sampling scale of the disk and the field of view. The internal and external radii of the disk are control parameters for the model e.g. R_{in} = 0.3AU R_{out}= 800 AU.

Since we assume an isotropic radiation from a central protostar, all dust grains at the inner radius are irradiated by the same protostar intensity. To calculate the scattering intensity, we use equation 6.12. Then, the scattered light intensity will be calculated according to the angle of scattering. We use Henyey-Greenstein phase distribution from equation 6.8, to calculate the scattered lights' intensity to the observer's projection plane.

$$I_{Scat} = (\frac{1}{4 \times \pi \times R_{Dist}^2}) \times P_{star} \times \phi(\theta) \tag{6.12}$$

where

I_{Scat} = scattered intensity
P_{star} = Power radiated by the central star
R_{Dist} = distance of dust grain from central protostar

The view angle (inclination angle) is used to construct the projected image of the scattering disks from different directions. The view angle is the angle between the plane of the disk and the detector plane.

6.3 Fresnel Imagery in Space

The Fresnel Diffractive Imager is proposed in many regimes, but these specifications are designed for the next 10-20 years. 20-meter arrays are expected to provide a good resolution for observation of disks; even larger arrays would give a better resolution and dynamic range. In this model, we use the specifications from table 4.1 to compute the Point-Spread-Function, which will be used for the convolution of accretion disks model.

The distance between the star and the observer will determine the angular dimension of the star and disk. The sampling scale in the disk model is accordingly adjusted to construct the image.

6.3.1 3D simulation and model perspective

The image shown in figure 6.6 is simulated at the following conditions (i) Henyey-Greenstein parameter at g =0.6 (it means it has a little more influence in forward scattering than isotropic scattering). (ii) disks inclination 60 ° corresponding to the line of sight. At the center of the image in the black region, it is the protostar, masked by the dust.

Due to the absorption of UV photons by the gas ionization and dust, there is a limit where UV radiation cannot penetrate and be scattered.(Richling S., 2000)[15] Therefore in the mid-plane of disks where the density is high, there is no scattered light coming to the observer.

Convolution by the PSF of a Fresnel Imager is then applied to the constructed image of accretion disks. The Point Spread function of a 20-meter Fresnel array is convoluted with the disks image to obtain the final output images. The different disks characteristics, distance of observation are tested to study the limitation of 20-meter Fresnel space mission.

Specifications	Fresnel Space Imager
Array size	20m
Array zones	1000 Zones
Wavelength	190 nm
Bandpass	160 - 220 nm
Instrument Resolution	1.5 mas
Image sampling	0.7 mas/pixel
Field optic diameter	2.25 m

Table 6.1: Fresnel Space Imager propose spacifications

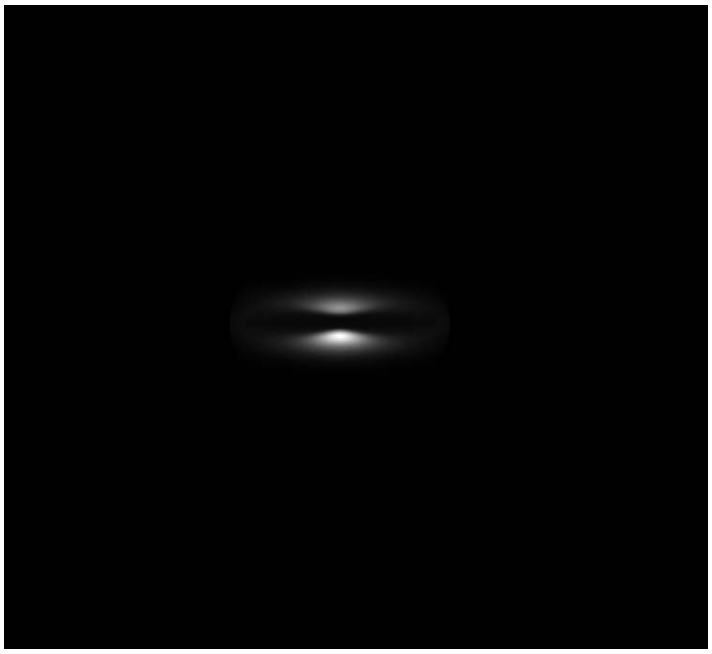

Figure 6.6: Scatter light from accretion illuminated by a central star: scattering parameter g = 0.6 scattered, disk inclination 60°, observer distance 150pc.

6.4 20-meter Fresnel array space observation

This simulation of a Fresnel Imager using a 20-meter array in space gives images of disks at different distances. From 50 pc, this array is able to observe the inner ring and the disks. While it goes further, the inner ring gets smaller angularly. Observations are still feasible until 1000 pc, showing the mid-plane and outer radius.

Figures 6.7 to 6.9 show the simulated accretion disks, at 60°inclination. Raw images on the left and convolution image on the right. They are simulated at 50pc, 150pc and 300pc. They are convoluted with the PSF of a Fresnel diffractive Imager; 20-meter arrays size, which has 1.5 mas resolution. In figures 6.7 to 6.9, the contrast is enhanced to present the spikes from PSF convolution. Figures 6.10 to 6.12 are images simulated at 80 ° inclination from 50 to 300 pc.

For a space mission with a 20-meter array, HH30 in Taurus, at 140 pc, is well within the range of observation, with the whole disks and the inner ring observable. Another interesting target could be T Tauri at 148 pc.

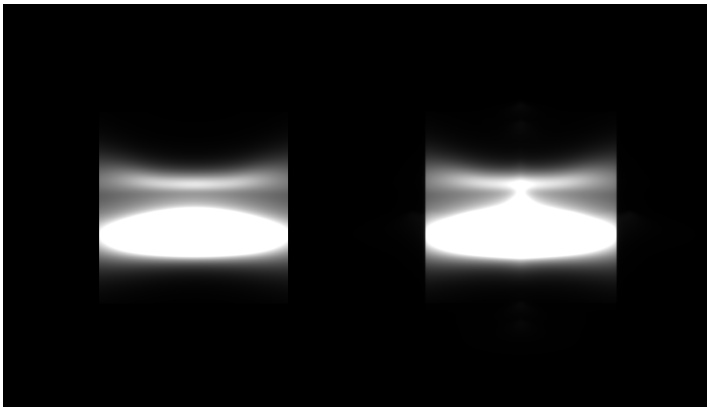

Figure 6.7: Images of an accretion disk at 60 °e inclination from 50pc. Left a) model image: g=0.6, Right (b) Output image from Fresnel Diffractive array, simulated by convolving the model with the PSF of a Fresnel Imager at 20-meter aperture.

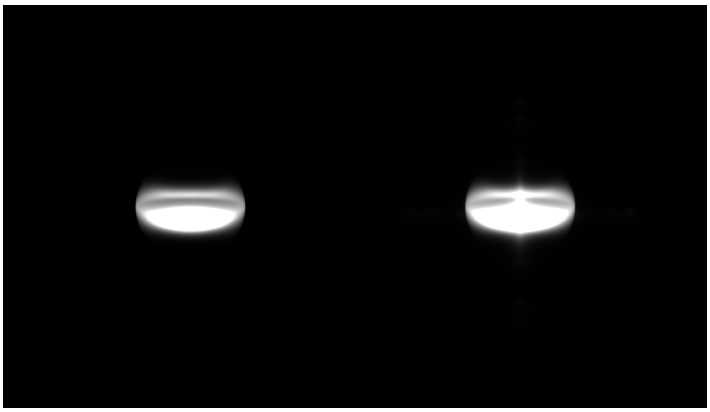

Figure 6.8: Images of an accretion disk at 60° inclination from 150pc. Left a) model image: g=0.6, Right (b) Output image from Fresnel Diffractive array, simulated by convolving the model with the PSF of a Fresnel Imager at 20-meter aperture.

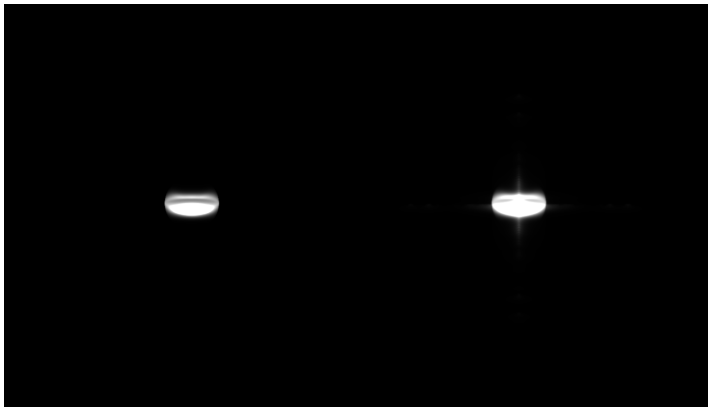

Figure 6.9: Images of an accretion disk at 60° inclination from 300pc. Left a) model image: g=0.6, Right (b) Output image from Fresnel Diffractive array, simulated by convolving the model with the PSF of a Fresnel Imager at 20-meter aperture.

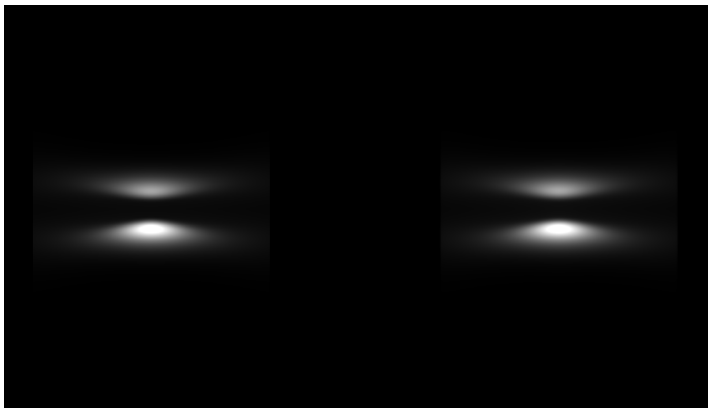

Figure 6.10: Images of an accretion disk at 80° inclination from 50pc. Left a) model image: g=0.6, Right (b) Output image from Fresnel Diffractive array, simulated by convolving the model with the PSF of a Fresnel Imager at 20-meter aperture.

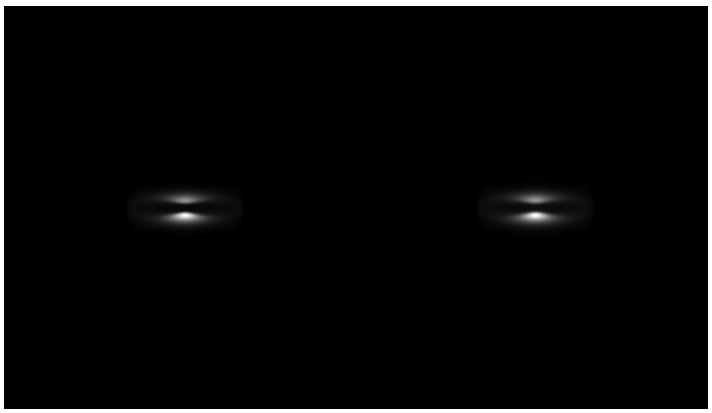

Figure 6.11: Images of an accretion disk at 80° inclination from 150pc. Left a) model image: g=0.6, Right (b) Output image from Fresnel Diffractive array, simulated by convolving the model with the PSF of a Fresnel Imager at 20-meter aperture.

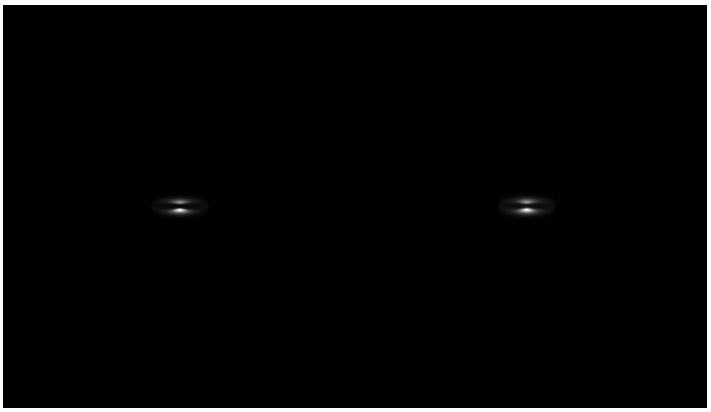

Figure 6.12: Images of an accretion disk at 80° inclination from 300pc. Left a) model image: g=0.6, Right (b) Output image from Fresnel Diffractive array, simulated by convolving the model with the PSF of a Fresnel Imager at 20-meter aperture.

Conclusion and Perspectives

For Astrophysical observations, the “Fresnel Diffractive Imager” is a new instrument concept. This concept used: diffractive focusing, has to be demonstrated so it can be developed and used for future space applications. The advantages it provides on high angular resolution and high dynamic range, while using a very light and thin material, will benefit to both space technologies and science aspects.

In this thesis, the Fresnel Imager concept has been validated for sky observation, using reduced scale prototypes.The necessary modifications and optimizations have been made to detect astrophysical targets. A 200 $\times$ 200mm “primary” module is used in our prototype, placed on a 19 meter refractor tube. A modified “receptor” module is positioned 18 m downstream: focal length of the primary module.

Our prototype generation II started with some modifications to generation I and operated at 800 nm when we first installed it on the refractor tube. Then optimizations and integrations continued until we finished in January 2009. Observations were made continuously during the installation processes. The results from sky observations showed the improvements of Fresnel Imager all along the integration process and helped us to optimize the system.

We checked the limitations of Fresnel Imager in angular resolution and dynamic range, at each version of the prototype. The final Fresnel prototype generation II has proven a 0.8" angular resolution and a 5.5 $\times 10^{-5}$ dynamic range at 8" separation.

In order to validate the instrument, this manuscript contains a synthesis of assessments in image quality and instrument functionalities. The processes of validation start from image quality measurements. Regarding image quality, Fresnel diffractive imager has proven to be suitable for high dynamic range and high angular resolution, as shown by Sirius AB images.

Mars and the detection of its satellites is also a solid proof of high dynamic range close to extended objects. We have been able to detect the orbital motion of Phobos and Deimos by direct imaging, which proves a 2.5 $\times$ 10^{-6} dynamic range at 30" angular separation (and probably at smaller angles too).

Before launching into space, Fresnel Imager has to be tested for performance in UV. As we have stated, the proposed mission for a Fresnel diffractive imager in space would operate in UV, to benefit from a high angular resolution while keeping an aperture size of 4 m. The “void and opaque focussing screen” concept can evolve to larger aperture telescopes for space, using a light weight focusing device. With the larger aperture instruments, the very high angular resolution will help resolving many deep space questions in the future.

Conclusion et Perspectives

L'imageur diffractif de Fresnel utilise un nouveau concept de focalisation pour l'observation astronomique. Ce concept de focalisation diffractive doit être testé pour les applications spatiales. Il procure entre autres des avantages décisifs pour la haute résolution angulaire et la haute dynamique, grâce à une membrane légère utilisant la focalisation diffractive "opaque-vide", qui profitera à la technologie spatiale.

Dans ma thèse, le concept du "Fresnel Imager" a été validé par des observations faites sur le ciel après les modifications et optimisations nécessaires des prototypes initiaux, qui ont été réalisées pour détecter des cibles astrophysiques. Il y a deux modules. Le module "grille primaire" supporte une ouverture de 200 × 200 mm utilisée dans ce prototype, placée pour les tests sur le tube de 19 mètres d'une lunette du XIX^{ime} siècle. Le module récepteur, qui a été modifié, est placé 18 m après la grille primaire : la longueur focale de la grille primaire.

Le prototype "génération 2" a commencé avec des modifications de la génération 1, exploité à une longueur d'onde de 800 nm lorsqu'on l'a installé sur le tube de la lunette. Ensuite, les optimisations et les intégrations ont continué jusqu'à ce que nous ayons terminé en janvier 2010. Les observations sont faites en continu pendant le processus d'installation. Les observations du ciel ont permis de contrler les améliorations du "Fresnel Imager" pendant le processus d'intégration et d'aider à optimiser le système.

On a vérifié les limites de l'Imageur de Fresnel en résolution angulaire et en dynamique, sur toutes les versions du prototype. La dernière génération : le prototype 2, a une résolution angulaire de 0,8 "et une dynamique de $5,5 \times 10^{-5}$ à 8" de séparation.

Ce manuscrit est une synthèse des évaluations de la qualité d'image et des fonctionnalités, faites afin de valider l'instrument.

En ce qui concerne la qualité d'image, l'Imageur du Fresnel diffractif est un instrument de qualité supérieure pour détecter des objets à haute dynamique et une haute résolution angulaire, comme le montrent les images de Sirius AB. C'est une réussite pour cet instrument de 200 × 200 mm d'ouverture.

Mars et la détection de ses satellites valide la haute résolution angulaire et haute dynamique à proximité d'objets étendus. Nous avons été en mesure de détecter le mouvement orbital de Phobos et Deimos par imagerie directe avec $2,5 \times 10^{-6}$ de dynamique à 30" de séparation angulaire (et probablement cela aurait été possible à moins de 30" de séparation). La validation au sol est donc réussie. Cet instrument a ainsi la capacité de fonctionner à longue focale, en deux modules séparés.

L'une des investigations supplémentaires des capacités de l'Imageur de Fresnel avant de se lancer dans l'espace doit être un test de performance dans le domaine UV. Comme on l'a dit, la mission proposée pour l'imageur de Fresnel diffractif dans l'espace serait d'exploiter pleinement la très haute résolution angulaire et la haute dynamique dans la bande UV. Le concept de focalisation diffractive "opaque-vide", peut évoluer vers des télescopes de grande

ouverture pour l'observation depuis l'espace.

Annexes

Appendix A

Fresnel Diffractive Imager: Instrument for space mission in the visible and UV

Accepted by SPIE Astronomical Telescopes and Instrumentation 2010

Fresnel Diffractive Imager: Instrument for space mission in the visible and UV

Raksasataya T.[a], Deba P. [a], Rivet J.P. [b], Gili R. [b], Serre D.[a], Koechlin L.. [a]

[a]LATT, Université Paul Sabatier, CNRS, 14 Avenue E.Belin, 31499 Toulouse, France;
[b]Obsecatoire de la côte d'azur, Bvd de lObservatoire, B.P. 4229 - 06304 Nice Cedex 4, France

ABSTRACT

We propose a new concept of diffractive optics: Fresnel arrays, for a 4 m aperture space telescope in the UV domain.

Fresnel arrays focus light by diffraction through a very thin binary mask. They form images optically and deliver very high quality wavefronts, specially in the UV. Up to 8% of the incident light is focussed, providing high angular resolution and high contrast images of compact objects.

Due to their focal lengths of a few kilometers in the UV, large Fresnel arrays will require two spacecraft in formation flying, but with relatively tolerant positioning. Diffraction focusing is also very chromatic; this chromatism is corrected, allowing relatively broad (30 to 100 nm) spectral channels in the 120-350 nm range. A 4 m aperture Fresnel imager providing 7 to 10 milli arc seconds resolution is very competitive for imaging compact and high contrast objects such as protoplanetary disks and young planetary systems, AGNs, and deep sky objects.

We have developed prototypes to validate the optical concept and related technologies : first a laboratory setup, then a 20 cm aperture ground-based prototype, which provides high contrast and diffraction limited images of sky objects in the visible and close IR. A new laboratory prototype is also being prepared for validation in the 250 - 350 nm wavelength range.

Keywords: Fresnel Imager, Diffractive focusing, Accretion disks, Ultra-violet domain

1. INTRODUCTION: OPTICAL CONCEPT AND STATE OF THE ART

For space telescopes with large apertures and light weight, we propose to replace the primary mirror by a thin membrane: a Fresnel Diffractive array. The optical concept has been described in detail in [1] . As the angular resolution is wavelength dependent, the advantages of Fresnel imager are high in the UV domain. We propose a 4m aperture Fresnel Imager operating at 120 to 300 nm.

This membrane the focuses light in a Fresnel imager is not reflective but opaque, with millions of void apertures, using an array of Fresnel rings held together by an orthogonal layout of narrow bars, the local period of bars being related to the Fresnel zones. The total area covered by the voids corresponds to almost 50% of the whole membrane.

The subapertures layout splits the incoming wavefront. One of the outgoing wavefronts is chosen, corresponding to diffraction order +1, in which 6% of the incident light is focused. The focal lengths of large Fresnel arrays are a few hundred to a few kilometers long in the UV domain, as the focal length f of a square aperture Fresnel array of size C having k_{max} Fresnel zones is given by

$$f = \frac{C^2}{8k_{max}\lambda} \quad . \tag{1}$$

Specifications	Fresnel diffractive imager prototype II
Main Array size	200 mm
Field optics diameter	45 mm
number of Fresnel zones	696
Central wavelength	800 nm
Bandpass	650 - 900 nm
Angular Resolution	0.8”
Field of view	500 ”

Table 1. Specifications of Fresnel Diffractive imager for ground based Validation on sky sources.

Formation flying of two spacecrafts is required. The second spacecraft is placed at the focal plane, where large field optics: a 60 cm telescope, forms a pupil plane. The chromatism of the Fresnel array is corrected by a small dimension diffractive mirror (in UV) of lens (in IR) placed in that pupil plane, and operating at order -1. The instantaneous bandwidth is $\Delta\lambda/\lambda \simeq 30\%$. Several such bands can be imaged sequentially, by changing the inter-spacecraft distance.

The unwanted orders of diffraction are blocked by a mask close to the pupil plane. Focal instrumentation and detectors are placed in the corrected bean.

In the next sections we present results obtained in the visible and close IR with a 200 mm aperture testbed: images of sky objects, and numerical simulations for UV based on protoplanetary disks models. We detail some science cases envisioned in the UV. The proposed techniques of detection and some targets will be described in the last section.

2. PROTOTYPE GENERATION II: GROUND-BASED VALIDATION TESTS.

As we propose a space mission with 4m-class apertures [2] , we first validate the concept by assessing the optical performances in angular resolution, throughput efficiency and dynamic range. These tests have been carried on with small aperture testbeds, as a test with a 4 m aperture would require kilometric focal lengths.

Following our generation I tests in laboratory (2005-2009)[3] , Tests on a generation II prototype are carried in 2009-2010 on the same principle, but modified for sky observation. As the objectives are to observe real astrophysical targets, the generation II prototype has been installed on a large refrector in Nice, southern France. The optics of the refractor are not used, but the tube and the mount allow steering of a 18 meter focal length ”two module” Fresnel imager.

In figure 1, prototype generation II is shown mounted on its refractor. The Fresnel array is visible at the front end on the right side of the tube, pointing at the sky. At the other end of refractor is the receptor module.

The Fresnel array used is a 200 mm apodized square aperture, 696 Fresnel zones array, the ring structure being held by means of thin orthogonal bars every 2 or 3 Fresnel zones. These bars contribute to the point spread function (PSF), but their layout has been optimized numerically before manufacturing, to keep as much as possible the high dynamic range and throughput efficiency at focus. The apodization is done by modulating the ratio between solid and void parts in Fresnel zones.

The testbed has been set up, a low altitude site close to the city of Nice, hence subject to light pollution and dust. However, this site has the advantage of being in a laminar flow from the sea and a potential for very good seeing conditions. The 200 mm Fresnel array tested on the sky has a 18m focal length at λ =800 nm.

Our optical axis runs parallel to the refractor tube and outside of it, leaving the historical refractor unmodified. The receptor module has a 45 mm aperture, to collect a 400 ” image field from Fresnel array.

Figure 1. Fresnel generation II testbed on the side of the 18 meter refractor at Observatoire de Nice. The 20 cm square Fresnel array is attached to the front end, the receptor module is the thin steerable optical bench at the rear end. The optical axis of the Fresnel imager runs in free air outside the refractor tube.

For these tests, we have chosen several criteria: angular resolution, field, dynamic range, spectral bandwidth, limiting magnitude. The sky targets chosen are binary stars with high magnitude difference, the surface of the moon, Mars, Saturn, Mars satellites, and galactic nebulae.

The outcome of these tests on the sky show a diffraction limited angular resolution (0.8"), the ability to make images within extended bright fields (fields on the moon surface), a limiting magnitude of 13.5 (in a quasi "streetlight" condition), and a dynamic range close to 2.510^{-6}. With this 20 cm aperture Fresnel imager testbed, among other targets, the satellites of Mars Phobos and Deimos have been imaged, and the Sirius AB couple has been resolved. These results and some others from our last observing run will be published soon, after a correct calibration is made.

2.1 Images from ground based observations

Our test Images were acquired on large magnitude difference binary stars, to test the dynamic range. ϵ Trianguli shown in figure 2 has been tested to measure dynamic performace of V magnitude= 5.3 and 11.3 at 4.7" separation.

Further investigations concerning the effect of spikes from the square array, affecting the contrast for extended objects, have been tested by observing the moon surface. With our 200 mm array aperture at λ =800 nm, we obtain large field images of the moon. In figure 5, the southern part of the moon is captured and shows small craters, down to 2 to 3 km diameter, corresponding to 1.5 ". The theoretical resolution is 0.8" is not reached, due to atmospheric seeing and residual misalinements.

3. PROTOTYPE GENERATION III: UV TESTBED

To validate the chromatic correction technology for the UV, a laboratory prototype (generation III) is being prepared.

A new 65 mm array has been carved, and the blazed lens in the prototype secondary module will be replaced by a diffractive concave Fresnel grating with a UV coating, under construction. This concave Fresnel grating will use only one reflection to correct the chromatism and focus the beam from the primary focal plane to the final focal plane. The tests are planned for the 2010-2011 period. There will still be two reflections in the field optics telescope upstream, required to form a pupil plane.

4. SPACE MISSION PROPOSED

We plan to propose a 4m-class mission in space, involving formation flying in orbit around L2. The diffraction limited imaging and high dynamic range capabilities preserved at short wavelengths should allow interesting science cases.

4.1 Fresnel Diffractive imager in Space, protoplanetary discs simulations

This study will assess the detection capability by a Fresnel Imager of accretion disks around protostars such as β Tauri. We compute a cicumstellar disk from an accretion model, based on[4] ,[5] ,[6] , and [7] . We then convolve the projected disk with the Point-Spread-Function of a Fresnal array computed from the specifications in Table 2. The radii and thickness of modeled discs are sampled to construct the accretion disk images at a scale adjusted to the Fresnel arrays' PSF.

The distance between the stars and the observer determines the angular dimension of the disks. These simulations show that a 4 m Fresnel Imager in the UV, having a 10 mas resolution and high dynamic range, should allow detection of disks around stars as far as 50 pc.

The Fresnel Diffractive Imager is proposed in several possible configurations, these specifications are designed for the next 10-20 years. Later, 20-meter arrays may provide a very high resolution for the study of compact objects at large diastances.

Figure 2. ϵ Trianguli (STF 201) and its companion at 4.7", magnitudes 5.3 and 11.3

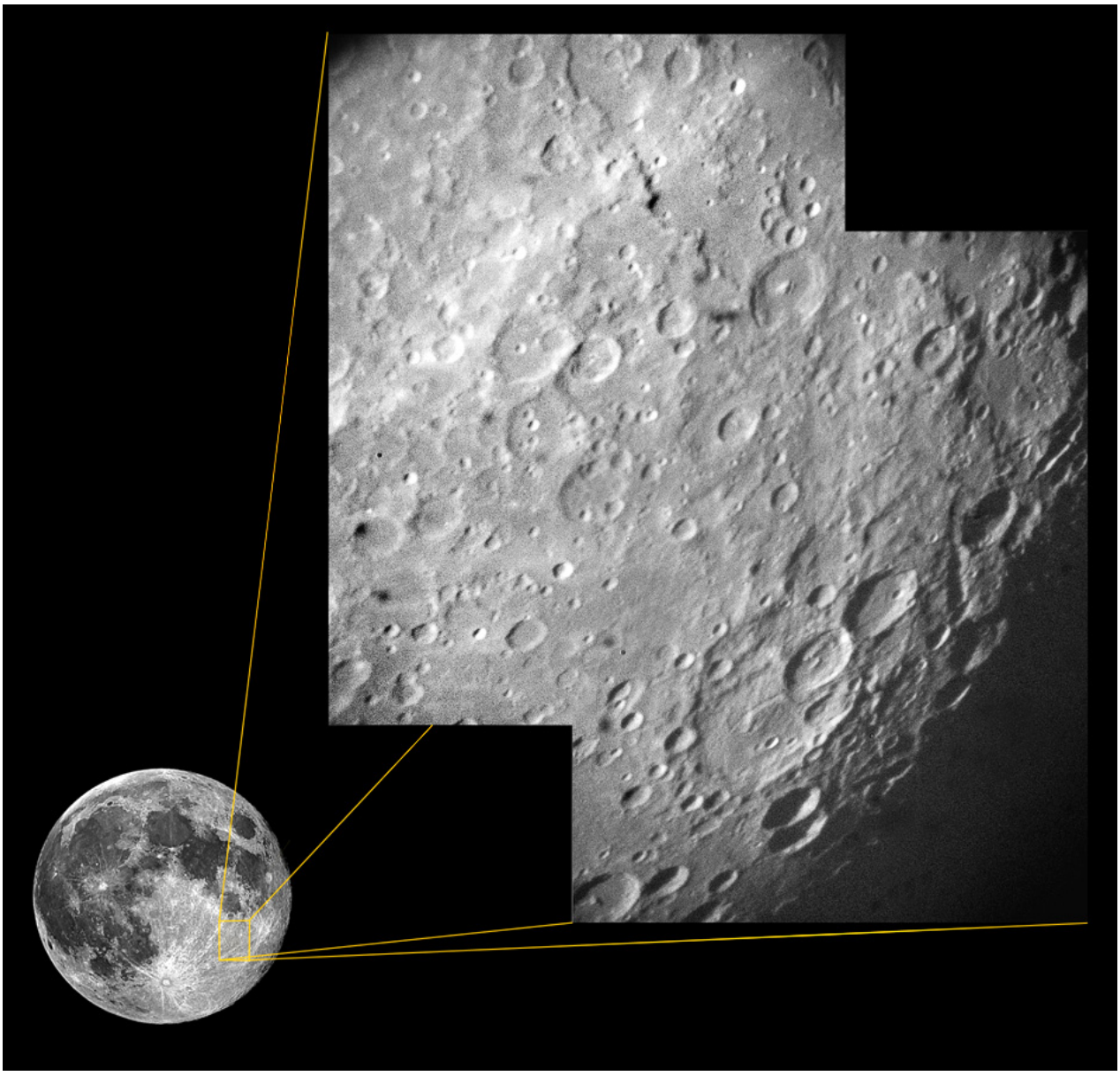

Figure 3. Mosaic of two images of moon surface showing the detail of craters on the moon surface with a 1" angular resolution. Image taken with a 200 mm square diffractive array at λ =800 nm. July 2009.

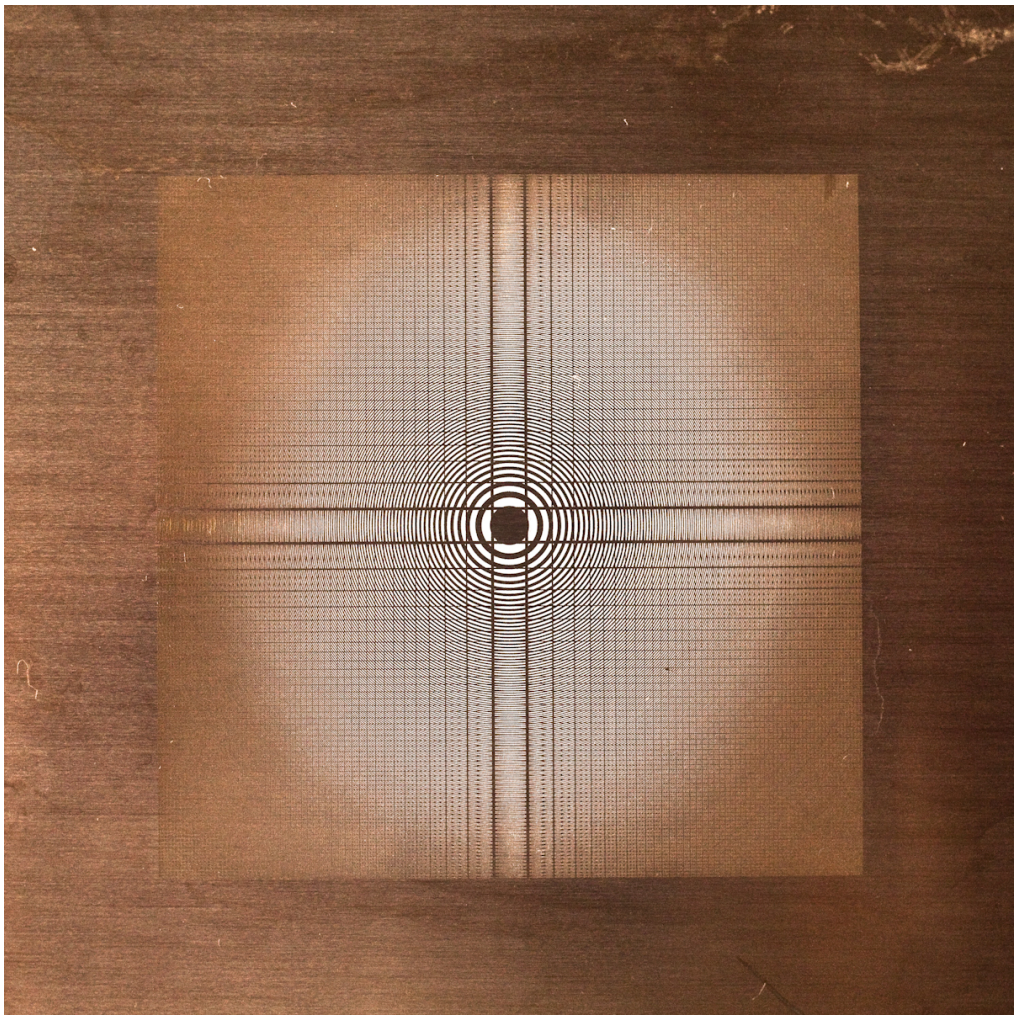

Figure 4. Fresnel Array for UV testbed: on a 65 mm square frame. It will be used for laboratory tests in the UV, from 340 to 250 nm.

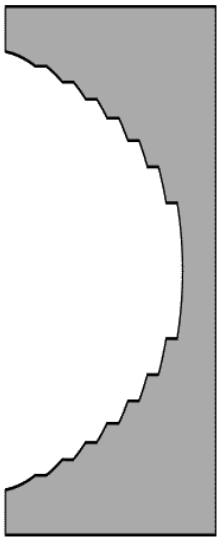

Figure 5. A diffractive concave Fresnel grating will replace the blazed lens for chromatism correction in the UV. Only the 7 central Fresnel zones are shown here.

Specifications	Fresnel Space Imager
Array size	20 m
Field optics diameter	2 m
Fresnel zones	3000
Wavelength	190 nm
Bandpass	150 - 250 nm
Angular Resolution	2 mas
Field of View	4.7 ”

Table 2. Fresnel Space Imager Specifications for UV image simulations.

5. CONCLUSION

The concepts and related technologies of a Fresnel Diffractive Imager are validated in various aspects. The results from ground-based sky tests are a good cues for a space mission. Some of the aspects of formation flying have also been tested during these ground-based tests. The next study on a UV testbed will improve the Technology readiness level (TRL) and allow to refine the and science cases.

In the future, High angular resolution and high dynamic of Fresnel Imagers will provide high quality deep sky data in many spectral bands:UV, visible and IR.

ACKNOWLEDGMENTS

This work has been funded by Université Paul Sabatier Toulouse, Centre National de la Recherche scientifique, Centre National d'Etudes Soatiales, Thales Alenia Space, and ”Réseau Thématique de Recherche Avancée ”Sciences et Technologies pour l'Aéronautique et l'Espace” (RTRA STAE) . We thank Observatoire de la côte d'Azur for allowing us observing time on the ”grand réfracteur”.

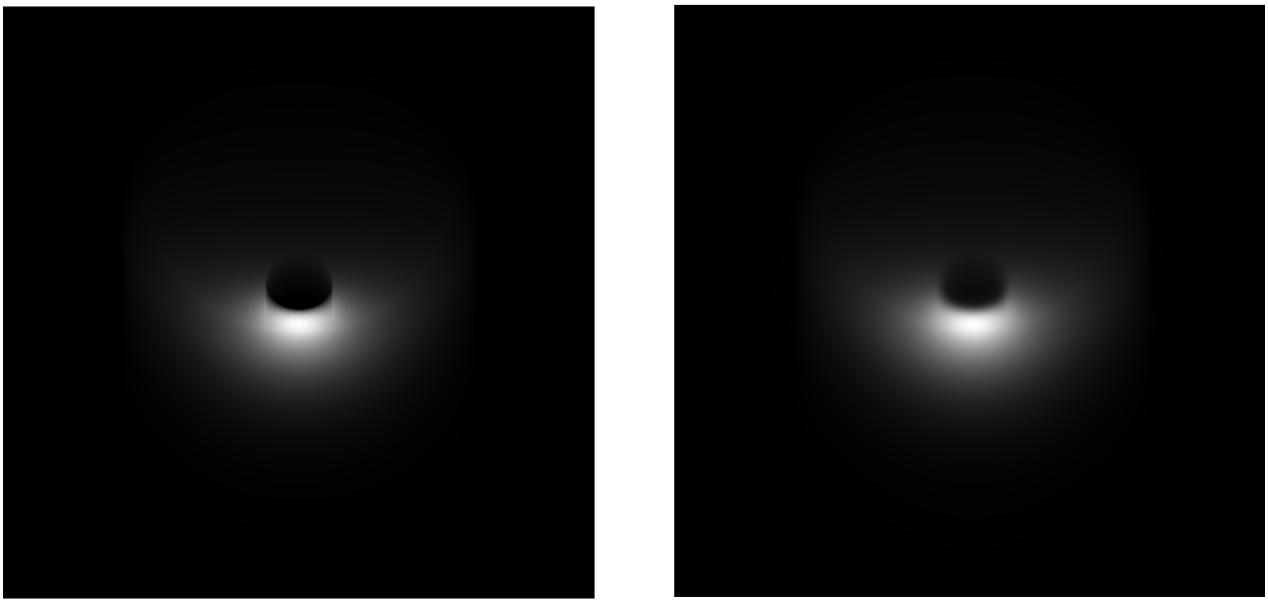

Figure 6. Left: Dust accretion disk simulated in section above at 60° inclination, Right: image obtained from convolution of a Fresnel imager point spread function (PSF) with the simulated disc

REFERENCES

[1] Koechlin L, Serre D., and Duchon P. High resolution imaging with fresnel interferometric arrays: suitability for exoplanet detection. *Astronomy & Astrophysics*, 443:709–720, 2005.

[2] Koechlin L.,Serre D., Deba P., Pelló R., Peillon C., Duchon P., Gomez de Castro A.I. , Karovska M., Désert J.-M. , Ehrenreich D., Hebrard G., Lecavelier Des Etangs A., Ferlet R., Sing D., and Vidal-Madjar A. The fresnel interferometric imager. *Experimental Astronomy*, pages 29–+, August 2008.

[3] Serre D., Deba ., Koechlin L. Fresnel Interferometric Imager: ground-based prototype. Applied Optics Vol. 48, Iss. 15, 2811-2820 (2009).

[4] Richling S. and Yorke H.W. Photoevaporation of Protostellar Disks. V. Circumstellar Disks under the Influence of Both Extreme-Ultraviolet and Far-Ultraviolet Radiation . *Nature*, 186:958, June 1960.

[5] Dullemond C.P, Hollenbach D. , d'Alessio P. Models of the Structure and Evolution of Protoplanetary Disks *arXiv:astro-ph,*/0602619v1 (2005).

[6] Gordon K.D. INTERSTELLAR DUST SCATTERING PROPERTIES. *Astrophysics of Dust, ASP Conf.* , 15, 2003.

[7] Semenov D., Wiebe D. and Henning Th. Gas-Phase CO-in Protoplanetary Disks: A challenge for turbulent mixing, *Astronomy & Astrophysics*, 647:L57-L60, 2006.

Appendix B

Generation 1.5 testbed of Fresnel Imager : setting up and first images

Submitted to Experimental Astronomy 2010

Noname manuscript No.
(will be inserted by the editor)

Generation 1.5 testbeds of Fresnel Imager : setting up and first images

Jean-Pierre Rivet[1], **Laurent Koechlin**[2],
Truswin Raksasataya[2], **Paul Deba**[2], **René Gili**[1]

the date of receipt and acceptance should be inserted later

Abstract The Fresnel Diffractive Array Imager (FDAI) is a new optical concept proposed for large telescopes in space. To evaluate its performance on real sky objects, we have built a new testbed of FDAI, especially designed for on-sky operation. It is an evolution of the laboratory setup previously used to validate the concept on artificial sources. In order to observe celestial objects, this new two-module testbed was installed in July 2009 at the *Observatoire de la Côte d'Azur*, (Nice, France), thanks to a funding by "Centre National d'Etudes Spatiales". The two modules of the testbed (the Fresnel array module and the receiver module), were secured at both ends of the 18 meter long tube of an historical refractor, used as an optical bench on an equatorial mount.

In this article, we focus on the evolution steps from a laboratory experiment to the first observation prototype, and on the targets chosen for performance assessment. We show the first on-sky results of a FDAI, although they do not reflect the nominal performances of the final testbed. These nominal performances have been attained only with the latest and most sophisticated prototype, and are presented in a separate article in this special issue.

1 Introduction

The concept of Fresnel Diffractive Array Imager (FDAI) as a space borne instrument has been proposed in [1,2], for high resolution astronomical imaging. It is based on the Soret's rings experiment [3] and is described in detail in other articles in this special issue.

In this article, we describe how we made the transition between the early 116 Fresnel zones laboratory prototype of Fresnel imager (the so called "Generation 1" prototype) to the 696 Fresnel zones fully featured observation instrument (the "Generation 2" prototype). We present the problems encountered, how we solved them, some sky target choices, the first images, and the initial performance assessments.

(1) Observatoire de la Côte d'Azur, B.P. 4229, F-06304 NICE Cedex 4, France
(2) Laboratoire d'Astrophysique de Toulouse-Tarbes, Université de Toulouse, CNRS, 31400 Toulouse, France

We started the validation campaign of the Fresnel diffractive imaging in 2005, shortly after the concept of orthogonal laser-carved Fresnel arrays came out. For a preliminary qualitative validation and for demonstration purpose, we have used a 20×20 mm stainless steel array with 40 Fresnel zones from center to corner, lit with a laser diode.

Later on, thanks to a CNES grant, we have started a quantitative laboratory broadband test campaign on a 80×80 mm array with 116 Fresnel zones on its semi-diagonal ("Generation 1" prototype). Its focal length was 23 m at 600 nm and the wavefront quality better than $\lambda/20$ peak-to-peak. This wavefront quality estimate comes from the position accuracy of the laser carving techniques : 5 μm, which is 20 times smaller than the smallest (outermost) individual sub-aperture.

The chromatic correction was achieved by a 16 mm diameter Silica blazed Fresnel lens with 116 zones. Chromatic correction over the whole visible domain has been assessed. In parallel, an end-to-end numerical simulation tool has been developed [4, 5]. A dynamic range of 10^{-6} has been measured with this laboratory setup, which is in good agreement with the numerical simulations [4]. The diffraction pattern we obtained experimentally was also in quantitative agreement with the simulated image. This proves the diffraction-limited imaging capabilities of this instrument.

However, more intermediate steps are required before a space mission can be accepted, based on this novel concept. One of them involves testing the instrument on real celestial sources. This has been done in 2009 and 2010 with the "Generation 2" prototype, which validates the concept in real observing conditions, and also addresses, in reduced size, some of the navigation aspects of a possible future formation flying space mission. To hold this prototype, we had the opportunity to use the historical 30" refractor of the *Observatoire de la Côte d'Azur* (Nice, France). This nineteenth century refractor was one of the largest of its time. We did not use the optics of this 18 m focal length refractor, but only its tube (as an optical bench), and its German equatorial mount and drive.

The layout and gradual implementation of the Fresnel astronomical imager prototype is described in sections 2 and 3 along with the problems encountered and the solutions found. The first stellar images, and the first performance assessments are described in sections 4 and 5.

The high dynamic range results that have been obtained after complete implementation, and their discussion are published as a separate article in this special issue [6].

2 General layout of the Generation 2 prototype

Our Fresnel Imager Generation 2 testbed has been designed to operate in the optical and close IR domains : 650–663 nm (H_α), 650–740 nm, and 740–880 nm, in order to benefit from a low atmospheric diffusion, sky transparency and better seeing. Moreover, given the external geometric constraints (maximum distance between both modules), and the manufacturing constraints of the Fresnel array (minimum size of individual sub-apertures), the surface of the entrance pupil scales like the wavelength to the power two. Thus, choosing relatively long wavelengths allows the largest possible aperture for the Fresnel array.

The testbed consists in two independent modules : the "Fresnel array" module placed ahead, which focuses incoming light by diffraction, and the "receiver" module placed 18 meters downstream, which corrects and record the focal images. They are

both secured on the west side of the 30" refractor's tube, the optical axis of which runs parallel the axis of our experiment.

The "Fresnel array" module holds the primary entrance diffractive array, a thin metal sheet laser-carved with a carefully designed pattern of sub-apertures, inherited from the Soret's ring pattern.

On a standard Soret's ring array, all ring-shaped sub-apertures have equal surfaces. However, to get better dynamics, some kind of apodization have been introduced on our Fresnel array : the surface of the sub-apertures is smaller near the edges than at the center. Thus, the outermost sub-apertures are thinner than they would be on a standard Soret ring array. Consequently, the main manufacturing constraint (minimum size of sub-apertures) is more stringent than it would be for a standard Soret's ring array.

The different assays of Fresnel arrays tested were designed to have less than 18 m focal length at 800 nm. This is the maximum focal length compatible with safe operations, taking into account the length of the refractor's tube and the inner radius of the dome. Given the maximal focal length of the array, the central wavelength λ_0, and the minimum sub-aperture size d_{min} compatible with the laser carving technology, we can compute the maximum size of the array, and the corresponding number of Fresnel zones. To do so, we need the following expressions for the focal length F and the size d of the smallest (outermost) sub-aperture :

$$F = \frac{D^2}{8n\lambda} \qquad \text{and} \qquad d = \frac{D}{8n\,\alpha}, \tag{1}$$

where λ is the corresponding wavelength, D is the diagonal size of the square Fresnel array, n is the number of Fresnel zones from center to corner, along the diagonal, and α is a coefficient larger than 1, that accounts for the apodization (the smallest sub-aperture is smaller than in the corresponding Soret's rings array; $\alpha = 1$ without apodization). Consequently, for a wavelength λ and a targeted focal length F, the expressions for the maximum diagonal size D and the maximum number n of Fresnel zones read :

$$D_{max} = \frac{F\,\lambda}{\alpha\,d_{min}} \qquad \text{and} \qquad n_{max} = \frac{F\,\lambda}{8\alpha^2\,d_{min}^2}, \tag{2}$$

where d_{min} is the minimum achievable sub-aperture size. Taking into account the manufacturing limitation (no carving smaller than $= 20$ μm) and the focal length limitation at 18 m, we chose to design a 200×200 mm square aperture Fresnel array ($D = 283$ mm) with 696 Fresnel zones on the semi-diagonal. The resulting focal length at $\lambda_0 = 800$ nm is $F_0 = 17.96$ m.

The Fresnel array is mounted on a mechanical frame which allows for manual rotations around the optical axis. This is useful to reject the diffraction spikes in regions of the image where they do not hide astronomically relevant elements.

The "receiver module" is more complex. It incorporates a field optics with a field stop, and a precision blazed Fresnel lens to compensate for the chromatism of the primary Fresnel array (focal length proportional to λ^{-1}). This fine optical component must be located in a plane where the field optics produces a sharp image of the entrance Fresnel array.

As any diffraction grating, the primary Fresnel array diffracts the incoming light on several diffraction orders. Only the light from the order +1 is focused on the CCD sensor. The light beams from other diffraction orders focus in other planes, and spread onto the sensor, acting as a near uniform background that might hamper the high

dynamics capabilities of the imager. Most of these beams are too faint to have a significant contribution at the sensor's level, except the light diffracted at the zero order. This light is not focused at all when it reaches the field optics. Thus, it converges in the focal plane of the field optics. To reject this unwanted light, a 1.5 mm opaque solid circular stop is inserted in this focal plane. This so-called "zero order mask" is held in position by a spider (two crossed 30 μm wires).

The receiver module also incorporates the science and guiding cameras, two *Andor Luca R* EMCCD cameras, and a custom-designed doublet to produce a final image onto the camera's sensor. The resulting final focal length a the level of the detector is $f = 3.12$ m.

Finally, for the sake of image dynamics and sharpness, the Generation 2 prototype incorporates a tip-tilt corrector. Its goal is to reduce the impact of the mechanical defects of the mount, and also of the lowest orders of the atmospheric turbulence.

The distance between modules is fixed, but the receiver module's orientation is steerable by a remote controlled two-axis translation stage. This attitude control is necessary for a precise alignment of both modules. This alignment condition is crucial for an accurate chromatic correction : the image of the entrance Fresnel array through the field optics must coincide exactly with the blazed Fresnel lens. Due to mechanical flexions, the attitude of the receiver module has to be fine-tuned frequently.

The angular on-sky field is limited by the diameter $D_{fs} = 45$ mm of the field stop located at the entrance of the field optics. With a focal length of $F_0 = 17.96$ m at the central wavelength $\lambda_0 = 800$ nm, this leads to a monochromatic field of view $\phi_0 = 517''$. For a non-vanishing bandpass $\Delta\lambda$, there is a trade-off between the field of view and the bandpass, for a given size of the field stop. Indeed, wavelengths longer than the nominal one (λ_0) will converge upstream with respect to the field stop (located at a distance F_0 of the primary Fresnel array). On the contrary, sorter wavelengths will converge downstream. Consequently the input beam for non-nominal wavelengths will have a non-vanishing size at the level of the field stop. Thus, the broadband unvignetted field of view ϕ and the bandwidth $\Delta\lambda$ for a given field stop diameter D_{fs} are linked by the following relation :

$$\phi + \frac{D}{F_0}.\frac{\Delta\lambda}{2\lambda_0} = \frac{D_{fs}}{F_0} = \phi_0, \tag{3}$$

where D is the diagonal size of the square entrance Fresnel array and F_0 is the primary focal length at the nominal wavelength λ_0. On our Generation 2 prototype, the maximum unvignetted bandwidth for vanishing field of view is thus $\Delta\lambda_{max} = 254$ nm for $\lambda_0 = 800$ nm.

In space, as the focal length will correspond to the distance between two free flying spacecraft (a few kilometers), Fresnel arrays will not suffer this limit in focal length, hence in aperture. However, large apertures will imply relatively large field optics : the field optics diameter being 1/6 to 1/10 of the primary aperture diameter (e.g. 0.4 m to 0.6 m prime focus field for a 4 m aperture). The other optics, downstream in the receptor module will be much smaller, and the corresponding ones in our Generation 2 testbed have diameters about half of those of a 4 m space borne Fresnel imager.

For a square aperture Fresnel array of size C, the angular resolution is the same as that of a solid square aperture : $R_{Airy} = \lambda/C$. The Rayleigh resolution for the Generation 2 prototype is $0.825''$. Since the CCD sensor has 1000×1000 pixels of 8×8 μm (0.53×0.53" for a final focal length $f = 3.12$ m), the final image contains roughly 650×650 resolution elements.

Fresnel Array size	200×200 mm
Number of Fresnel zones from center to corner	696
Type of Fresnel array	Orthocircular [7]
Central wavelength λ_0	800 nm
Primary focal length F_0 at λ_0	17.96 m
Field stop diameter	45 mm
Field of view for vanishing bandwidth ϕ_0	$517''$
Unvignetted bandpass $\Delta\lambda_{max}$ for vanishing field of view	$673 - 927$ nm
Angular Airy radius at λ_0	$0.825''$
Detector pixel size	8 μm
Final focal length f (at detector)	3.12 m
Pixels per Airy radius	1.5

Table 1 Specifications of the full-fledged Fresnel Imager Generation 2 testbed.

The specifications of the Generation 2 ground-based testbed are summarized in Table 1.

3 Gradual evolution from Generation 1 to Generation 2

From the laboratory Generation 1 prototype to the full-fledged sky-watcher Generation 2 instrument, we chose to evolve in a step by step approach, new components replacing the old ones gradually, while keeping the optical system operational. On-sky validations were performed after each significative upgrade of the instrument. The major milestones between the early laboratory testbed and the latest on-sky instrument are summarized in Table 2. Figures 1 and 2 show the primary Fresnel arrays of Generation 1 and Generation 2 testbeds respectively,

3.1 The "Generation 1.5.1" intermediate prototype

The design phase for the on-sky version lasted from December 2007 to June 2009. We chose the wavelength domain and designed the optics accordingly. The technical solutions to secure the two modules of the testbed onto the refractor's tube were crucial design issues. Standard hardware solutions had to be rejected, since the refractor is part of an historical monument, and no permanent modification was allowed. Nonetheless, the mechanical link between the modules and the refractor's tube had to be as stable and reliable as possible, for the sake of instrumental stability. Another important issue was the logical connection between the refractor's driving electronics and the prototype's tip-tilt corrector device : when the tip-tilt corrector happens to run out of its correction range, it has to automatically interact with the refractor's slow motion driving system.

In spring 2009, a new 200×200 mm metal primary array with 696 Fresnel zones was delivered by the manufacturer and replaced the 80×80 mm array with 116 Fresnel zones, formerly tested in our laboratory setup (Generation 1). The new compound "orthocircular" design [7] for the 200×200 mm Fresnel array involves less bars to sustain the Fresnel rings, than the earlier one used on the laboratory Generation 1 testbed. As a consequence, the spikes are 3 times fainter and the central lobe almost twice as bright. Thus the brightness ratio is improved by a factor 6.

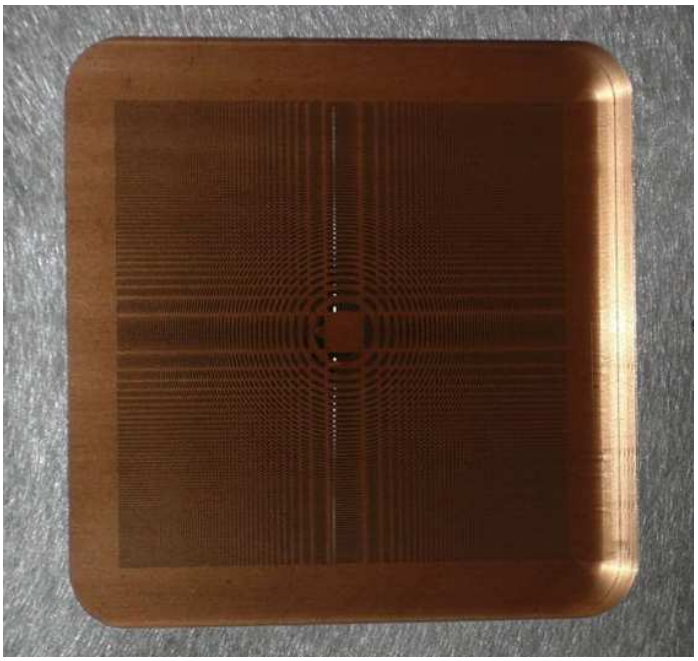

Fig. 1 The primary Fresnel Array for the Generation 1 prototype: 80 × 80 mm, 116 Fresnel zones from center to corner.

The old chromatic correction Fresnel lens (diameter 16 mm, 116 Fresnel zones) was still in use. This limited the effective aperture to a circle of 115 mm in diameter. The instrument operated without any tip-tilt corrector. Consequently, the atmospheric tip-tilt and the mechanical drifts and flexions affected the quality of the images. The sensor was still a *Starlight SXV-H9* camera (392 × 1040 pixels of 6.45 × 6.45 μm).

In July 2009 the Generation 1.5.1 testbed was moved on the 30" refractor's tube in Nice, and received its first star light. The specifications of this intermediate step is described in the column "Gen. 1.5.1" of Table 2 (the column "Gen. 1" of this table recalls the specification of the early laboratory testbed).

3.2 The "Generation 1.5.2" intermediate prototype

In September 2009, the new 58 mm blazed Fresnel lens with 702 Fresnel zones (manufactured by ion etching on fused silica) is delivered by the provider. This Fresnel blazed lens intended for chromatic correction has six more zones on its semi-diagonal than the primary Fresnel diffractive array. This allows for slight displacements of the primary array's image on the blazed Fresnel lens. The slight linear chromatism that results from these displacements is needed to compensate for differential atmospheric chromatism at moderate or high air masses. In addition, a new, custom-designed, doublet was also delivered, for final imaging on the CCD sensor. Special housing had to be designed and realized to protect these fine optics against dust contamination during on-sky op-

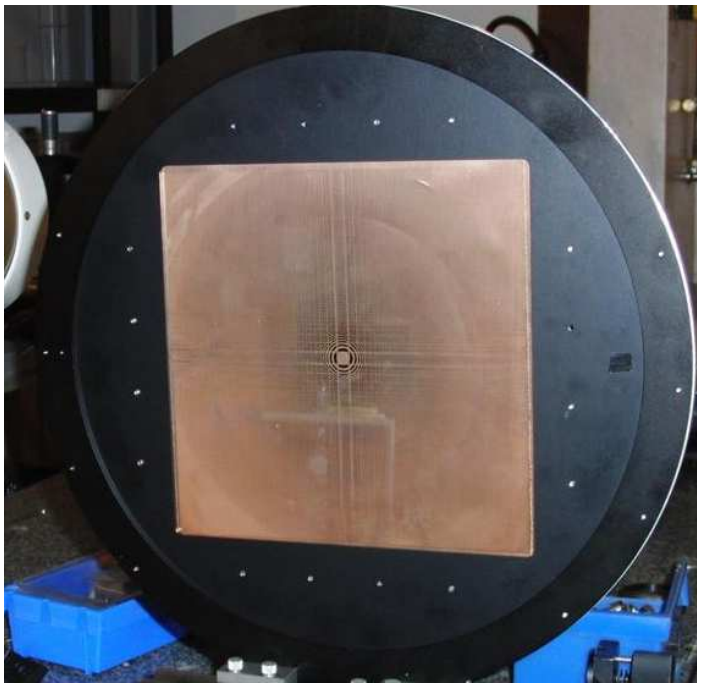

Fig. 2 The primary Fresnel Array for the Generation 2 prototype : 200×200 mm, 696 Fresnel zones from center to corner.

erations (no clean room). These new optical elements have sufficient diameter to take advantage of the full 200×200 mm of the aperture diffractive Fresnel array.

The mechanical structure of the prototype have also been improved : when not strictly vertical, the 2 meters optical rail of the receiver module bends under the effect of gravity. This leads to orientation-dependent internal misalignments within the optical components of the receiver. To cope with this problem, we have stiffen the optical rail of the Generation 1.5.2 prototype with yards and marine-like steel guys.

Besides the flexions of the receiver's optical rail, the 18 meter long refractor's tube also bends under the action of gravity. Thus, the tube takes a bow shape, the flexion angle of which can reach a few arc minutes. In normal operation mode (that is, when the instrument is used as a standard refractor), this altitude-dependent bending of the tube does not affect the orientation of the refractor's optical axis, since the tube is designed so that both ends deviate by the same amount. However, as our receiver module is linked to the rear end of the tube, its orientation follows the local tangent to the tube. This yields some altitude-dependent misalignment of the receiver module with respect to the Fresnel array module. Consequently, the correct alignment of both module, which is critical for correct chromatic correction, has to be checked and corrected frequently. The angular precision required for a good chromatic correction is λ_0/S, where S is the diameter of the field optics. This corresponds to $3.6''$ for a 45 mm field stop at 800 nm. The adjustment procedure that we have developed to solve this problem is likely to be helpful to design the policy of attitude control for the receiver spacecraft in future formation flying space borne version.

Generation	**1**	**1.5.1**	**1.5.2**	**2**
First light	04/2006	06/2009	09/2009	01/2010
Context	lab.	sky	sky	sky
Primary array size (mm)	80×80	200×200	200×200	200×200
Primary array # of zones	116	696	696	696
Fresnel lens diameter (mm)	16	16	58	58
Fresnel lens # of zones	116	116	702	702
Imaging doublet	off-the-shelf	off-the-shelf	custom	custom
Detector(s)	*Starlight SXV-H9*	*Starlight SXV-H9*	*Starlight SXV-H9*	2× *Andor Luca R*
Tip-Tilt corrector	no	no	no	yes

Table 2 Summary of the technical evolution of the Fresnel imager testbeds from the early Generation 1 prototype to the full-fledged Generation 2 instrument.

3.3 The "Generation 2" final prototype

As far as only optical elements are concerned, the Generation 1.5.2 testbed is complete at this stage. However, the quality of long exposure images was hampered by tit-tilt motions of various origins (slight polar misalignments, periodic error of the mount's worm gear, tube mechanical flexions, atmospheric turbulence). In addition, the non-intensified CCD sensor of the *Starlight SXV-H9* camera lacked some sensitivity. These problems have been corrected (at least partially) by a 100 Hz tip-tilt corrector, which was delivered late 2009, together with a new sensor module. This sensor module features two *Andor Luca R* intensified EMCCD cameras, one to record science images, an the other one to monitor tip-tilt errors on a guide star. The beam splitting between both cameras is done by a dichroic plate. A computer closes the servo loop and sends translation orders to the piezoelectric XY translation stage which bears the final imaging doublet. The resulting Generation 2 prototype of Fresnel imager and its first results are thoroughly described in a separate article in this special issue [6].

4 First on-sky images with the Generation 1.5.1 intermediate prototype

The first on-sky images from our Fresnel Imager have been acquired in July 2009 with the Generation 1.5.1 testbed. Several observations of bright single stars and of binary or multiple systems have been done, for performance assessments.

4.1 Bright single stars

Two very bright stars, *Vega* and *Deneb*, have been used for the initial optical alignements of the testbed, and for a careful study of the PSF. As far as we know, these images are the very first images of astronomical targets obtained with a carved metal sheet as focusing component.

Figure 3 shows an image of *Deneb* taken with the Generation 1.5.1. The image displays the four expected spikes in the PSF, due to the orthogonal structure of the bars which hold the Fresnel rings in the diffraction array. Four diffraction spikes stick out from the central lobe of the PSF : two from order (0 in x, +1 in y), and two from

order (+1 in x, 0 in y). The central lobe originates from diffraction order (+1 in x, +1 in y).

Besides the four expected spikes, four other short spikes show up. They are due to the diffraction of light by the spider holding the zero order mask (see Section 2). In later observation runs, the respective orientation of the primary array and of the spider have been trimmed so that both spike sets be superimposed.

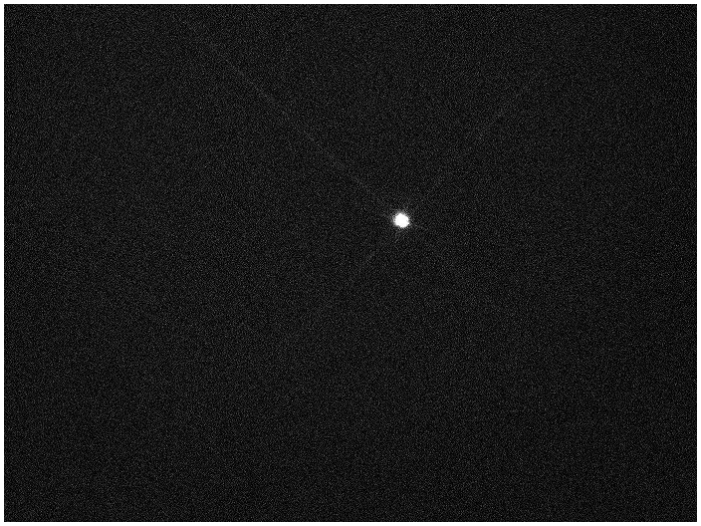

Fig. 3 Image of *Deneb*, with the Generation 1.5.1 testbed in the $740-900$ nm bandpass. The central lobe and the diffraction spikes of the primary array are clearly visible. A secondary set of spikes is also visible, originating from diffraction by the spider of the zero order mask.

4.2 Multiple Stars

Tests on multiple stars have been performed for field calibration, and to assess the capabilities of our Fresnel imagers in terms of contrast and effective resolution. Table 3 sums up the characteristics of the double or multiple stars which have been considered in this article. For these tests, the exposure time varies between 1 s and 100 s, and the selected spectral band is $750-850$ nm. As a consequence, the V-magnitudes in Table 3 do not reflect exactly the PSF brightness ratios.

Figure 4 shows an image of the $\epsilon - Lyr$ system obtained with the Generation 1.5.1 prototype. Since the effective aperture of this prototype was 115 mm in diameter (see Section 3.1), the expected diffraction-limited resolution is $1.7''$ at 800 nm. On the image we obtained, the PSFs are blurred asymmetrically. This is due to a less than ideal chromatic correction stability. The resulting anisotropic PSF size is $2 \times 4''$. Consequently, the two components of $\epsilon_2 - Lyr$ are not clearly resolved, whereas those of $\epsilon_1 - Lyr$ are.

To have the East-West orientation of the pictures, we have made a 10 s exposure on $\alpha - Lyr$, with the sidereal motion switched off (see inserted picture in Figure 4).

System		V magnitude	Separation
STT 433	A	4.4	
	B	10	A-B : 15.3”
	C	9.9	A-C : 21.8”
$\epsilon_1 - Lyr$	A	5.0	
	B	6.1	A-B : 2.6”
$\epsilon_2 - Lyr$	C	5.2	A-C : 212”
	D	5.5	C-D : 2.3”
STF 2726 $(52 - Cyg)$	A	4.2	
	B	8.7	A-B : 6.4”

Table 3 Characteristics (magnitudes and separations) of the binary and multiple systems under consideration in this article.

The wrinkles on the East-West track are due to atmospheric tip-tilt only, since the refractor's tube was still. This axis orientation holds for star images presented here, made with the *SXV-H9* camera.

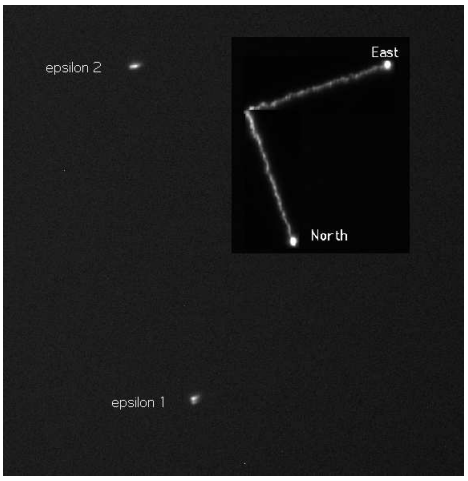

Fig. 4 Image of the multiple system $\epsilon_1 - Lyr$ and $\epsilon_2 - Lyr$ obtained with the Generation 1.5.1 prototype (115 mm effective aperture). The direction of separation of these binary systems are approximately at right angle. On this image, the chromatism is not perfectly corrected, hence the anisotropic blurring of the PSFs. The upper-right inserted image shows the North and East directions (see text).

The scale of the image, in arc seconds per pixel, can be deduced from a distance measurement on the image, and from the angular separation of the couple. The final focal length on the CCD sensor can be deduced from the Camera's pixel size (6.45 μm for the *SXV-H9* camera). Table 4.2 sums up this calculation. The resulting scale is $0.372 \pm 0.001''$/pixel. This effective focal length is much shorter than the primary array focal length. This is due to the relay optics (blazed Fresnel lens and imaging doublet) in the receiver module that we have dimensioned for a correct sampling of the PSF.

Angular separation ($''$)	209.85
Linear separation(px)	564 ± 1
Scale ($''$/px)	0.372 ± 0.001
Focal length (mm)	3576 ± 6

Table 4 Image scale calibration with $\epsilon - Lyr$.

This value is different for the Generation 1.5.2 prototype, since the blazed Fresnel lens is different.

Figure 5 is a long exposure (300 s) image of the binary star STF 2726 ($52 - Cyg$). The companion is 4.5 magnitudes fainter than the central star, and the angular separation is $6.4''$. The companion STF 2627-B emerges out of the noise, on the right side of the main star. The noise clearly visible in the image comes from the lack of sensitivity of the *Sony ICX285AL* CCD sensor of the *SXV-H9* camera. The system STF 2726 is the closest couple with such a magnitude difference we have imaged with the Generation 1.5.1 testbed. It is worth noting that this 300 s exposure have been obtained without any guiding or tip-tilt correction. The refractor's mount and drive happen to be accurate enough to allow such 300 s exposures without any correction. As for $\epsilon - Lyr$, the scale of the image can be deduced from a distance measurement

Fig. 5 Image of the double star STF 2726 ($52 - Cyg$) obtained with the Generation 1.5.1 prototype (115 mm effective aperture). The companion on the right hand side is 4.5 magnitudes fainter than the central star, and separated by $6.4''$.

on the image, and from the angular separation of the couple, found in the Washington Double Star catalog (WDS). Table 4.2 sums up this calculation. The resulting scale is $0.38''$/pixel. Even with the same optical elements, the effective focal length strongly depends on the exact positions of these elements, and also on the focus setting of the field optics (a Maksutov telescope). This is why the focal length estimate obtained with STT 2726 (3.47 m) slightly differs from the value obtained with $\epsilon - Lyr$ (3.58 m). As a consequence, the image scale calibration must be performed after each optical fine tuning operation. In the future, this scale calibration will be done by observing a bright

Angular separation ($''$)	6.4
Linear separation(px)	16.7
Scale ($''$/px)	0.38
Focal length (mm)	3472

Table 5 Image scale calibration with the binary star *STT* 2726.

single star with a narrow band filter, through a broad grating located upstream from the primary Fresnel array. This will produce secondary peaks in the image, at precise angles [8].

5 Results obtained with the 1.5.2 intermediate prototype

The triple star *STT* 433 have been used to assess the high dynamic imaging capabilities of the Generation 1.5.2 testbed (full 200×200 mm aperture; new 58 mm blazed Fresnel lens for chromatic correction). Figure 6 shows the resulting image. The spikes appearing on this image have been oriented so that they do not overlap the companion stars. The orientation of the spikes can be trimmed by rotating the main Fresnel array around its optical axis.

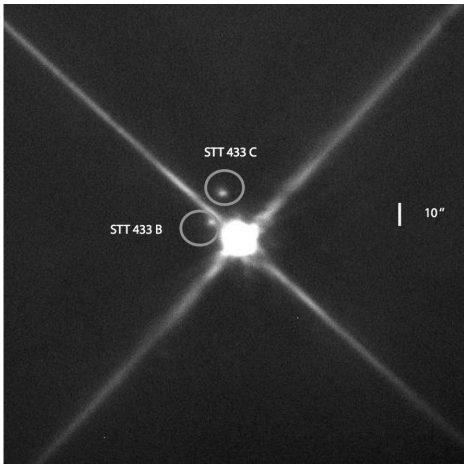

Fig. 6 Image of the multiple star *STT* 433 and its companions B and C, with the Generation 1.5.2 prototype. Exposure time on the *SXV-H9* camera : 300 s.

To test the imaging capabilities of the Generation 1.5.2 prototype on resolved astronomical sources, we have taken pictures of the Moon (see Figure 7). This demonstrates the imaging quality of Fresnel imagers on large fields or on fields with a bright background. The contrast is lower than in the case of compact objects, but the high resolution is still there.

For these images of the Moon, the chromatic correction settings have been performed by taking advantage of the moiré fringes that appear in the pupil plane from the superposition of two Fresnel rings patterns : the main array and the blazed Fresnel

lens [9]. The orientation and spacing of these moiré fringes give informations on the residual misalignment. In later versions of the prototype, extra optics will be added, to image the pupil plane. So, controlling the correct superposition of the blazed Fresnel lens and of the image of the primary Fresnel array will be made easier and more accurate.

The mosaic of two images in Figure 7 shows a region in the south-east of the Moon around *Janssen Crater* (45 South, 42 East) and *Reita Vallis*, which extends north-south on 500 km. The bright diagonal strip is a ray from *Tycho Crater*, crossing *Rupes Altai*. The field covered in a single frame is 1070 × 800 km. The exposure time on the *SXV-H9* CCD camera was 100 ms. The scale calibration of this image has been done

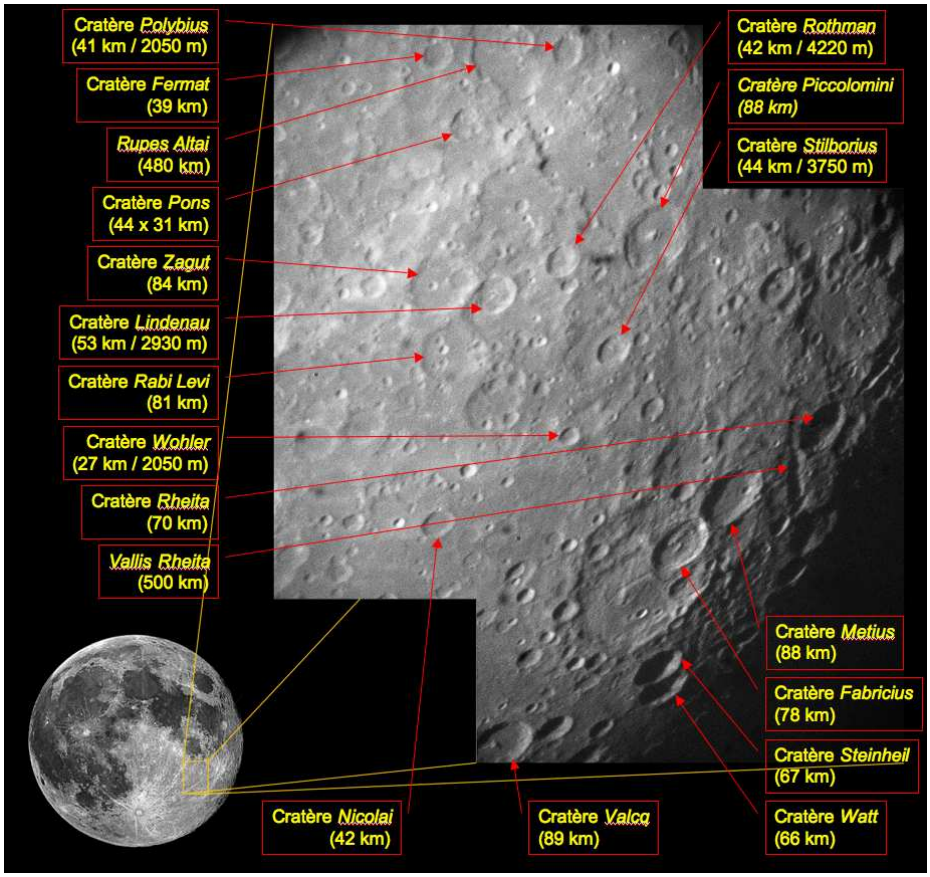

Fig. 7 Mosaic of two images covering 1155 × 986 km on the Moon, obtained with the Generation 1.5.2 prototype on October 7, 2009. The pictures show the south-eastern part of the quasi full moon, between *Nectaris Mare* and *Janssen Highland*.

on 6 large and well defined craters clearly visible in the field, assuming a topocentric distance of 372 000 km for the Moon region under consideration, at the date of the observation (October 7th, 2009, 03h UT). We find an average field scale of $0.426''$ per

Crater	Zagut	R. Levi	Nicolai	Lindenau	Buch	Büsching	Average
Diameter (km)	84	81	41	53	54	52	
Diameter ($''$)	47	45	23	29	30	29	
Diameter (pix)	97	106	53	74	72	70	
Scale ($''$/pix)	0.480	0.423	0.429	0.397	0.416	0.412	0.426

Table 6 Scale calibration for the image of the Moon.

pixel, and an effective focal length of 3.12 m for a pixel size of 6.45 μm. Table 5 sums up the calibration measurement on the Moon.

At 800 nm with a 200×200 mm aperture, the diffraction-limited resolution is $0.82''$. This corresponds to a linear resolution of 1.5 km on the Moon, and 1.94 pixels on the CCD sensor. Kilometric-sized details are visible on the full resolution image of the Moon. For example, the shadow inside the 6 km satellite crater *Nicolai-D* (small crater on the North side of *Nicolai Crater*) is clearly visible. Thus, this image of the Moon obtained with Generation 1.5.2 prototype can be considered as close to diffraction limited.

6 Conclusions and perspectives

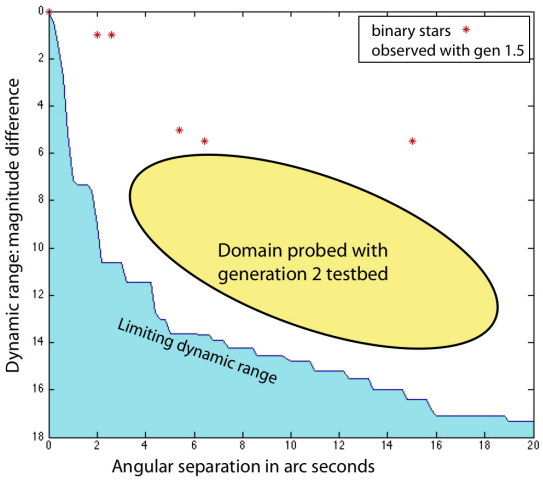

Fig. 8 Separation versus contrast diagram. The star markers represent the couples actually studied with the Generation 1.5.1 and 1.5.2 testbeds. The continuous curve is the theoretical limit, and the ovale shaded shape sketches the expected region of action of the full generation 2 testbed.

The intermediate prototypes 1.5.1 and 1.5.2 have modest performances. They were only intended to reveal the potential problems, to prepare the observation procedures, and to ensure a progressive transition between the laboratory prototype and the final Generation 2 observing testbed. The full performances will be attained with the full

Generation 2 prototype, equipped with a tip-tilt correction and with more sensitive EMCCD cameras.

Figure 8 is a separation versus magnitude difference diagram. The star-shaped dots represent the couples actually measured with the intermediate prototypes. The continuous curve is the boundary of the theoretically accessible region, and the shaded elliptic shape sketches the region that is to be sampled by the Generation 2 instrument.

The preliminary experiments reported in this article have provided for valuable experimental feedback. For example, they have clearly demonstrated the importance of frequently controlling and correcting the orientation of the receiver module, in order to have a correct chromatic correction.

The mechanical stiffness of the optical rail in the receiver module has also proven to be an important issue. Simple "hardware" solutions have been found, implemented and successfully tested on the intermediate prototypes. This valuable experimental feedback has benefitted to the Generation 2 prototype.

The Generation 2 prototype which is currently under investigation will allow higher dynamic range and resolution observations. Another article in this special issue is dedicated to its first observation campaign during which more difficult targets have been studied.

References

1. L. Koechlin, D. Serre, & P. Duchon, *"High resolution imaging with fresnel interferometric arrays : suitability for exoplanet detection"*, *Astronomy & Astrophysics* **443**, pp. 709–720, 2005.
2. L. Koechlin, D. Serre, P. Deba, R. Pelló, C. Peillon, P. Duchon, A. I. Gomez de Castro, M. Karovska, J.-M. Désert, D. Ehrenreich, G. Hebrard, A. Lecavelier Des Etangs, R. Ferlet, D. Sing, & A. Vidal-Madjar, *"The fresnel interferometric imager"*, *Experimental Astronomy* **23**, p. 379, 2009.
3. J.-L. Soret, *"Sur les phénomènes de diffraction produits par les réseaux circulaires"*, *Archives des Sciences Physiques et Naturelles* **52**, pp. 320-337, 1875.
4. D. Serre, *"LImageur Interférométrique de Fresnel : un instrument spatial pour lobservation à haute résolution angulaire"*, PhD thesis, Université Paul Sabatier, Toulouse (France), 2007.
5. D. Serre, *"The Fresnel Imager : Instrument Numerical Model"*, *Experimental Astronomy*, to appear in this special issue, 2010.
6. L. Koechlin, J.-P. Rivet, P. Deba, T. Raksasataya, T. Gharsa & R. Gili, *"Generation 2 testbed of Fresnel Imager : first results on the sky"*, *Experimental Astronomy*, to appear in this special issue, 2010.
7. D. Serre, P. Deba, L. Koechlin, *"Fresnel Interferometric Imager : ground-based prototype"* *Applied Optics* **48**(15), pp. 2811–2820, 2009.
8. M. E. Germain, G. G. Douglass & C. E. Worley, *Astron. J.* **117**, pp. 2511–2527, 1999.
9. L. Mertz & N.O. Young) N.O., *"Fresnel transformation of images"*, in the proceedings of the *International Conference on Optical Instrumation Techniques*, K.J. Habell ed., vol. 305. Chapman and Hall, London (1961).

Appendix C

Generation 2 testbed of Fresnel Imager : first results on the sky

accepted by Experimental Astronomy 2010

Noname manuscript No.
(will be inserted by the editor)

Generation 2 testbed of Fresnel Imager : first results on the sky

Laurent Koechlin[1], **Jean-Pierre Rivet**[2],
Paul Deba[1], **Truswin Raksasataya**[1],
Thierry Gharsa[1], **RenéGili**[2]

the date of receipt and acceptance should be inserted later

Abstract We present and discuss the first sky images obtained with a second generation "Fresnel Diffractive Array Imager" (FDAI) prototype.

The focusing objective: a 200×200 mm "Fresnel array", is a 50 μm-thick opaque foil featuring approximately 250 000 specially shaped void apertures, corresponding to 696 Fresnel zones. It focusses light by diffraction.

This prototype has been installed in parallel to the 76 cm "*grand équatorial*" (17.89 meter focal length) at the *Observatoire de la Côte d'Azur*, (Nice, France). The Fresnel array is attached close to the front end and on the side of of the 19 m long refractor's tube. The "receiver module" (field optics, chromatic corrector and cameras) is placed at prime focus of the Fresnel array, and attached to the refractor tube close to the rear end. The chromatic correction in the receiver module is adapted to 800 nm, but operates successfully in the two spectral bands used : $630 - 745$ nm and $750 - 950$ nm.

This setup has been used to test the on-sky capabilities of the diffractive imaging system in angular resolution, limiting magnitude and contrast, and to experience some of the situations that will be encountered in a future space-borne formation flying configuration.

We have obtained high contrast diffraction-limited images of various celestial sources, with a field of view larger than $500''$, a resolution of $0.8''$ at 800 nm, and a dynamic range better than 10^{-5}.

1 Introduction

The Fresnel Diffractive Array Imager (FDAI) is based on the binary Soret rings plate concept (Soret 1875). An orthogonal structure is superimposed to the traditional Soret rings, so that the structure is self-sustained, and can be realized by laser carving a thin opaque sheet (no transparent substrate needed). Fig. 1 shows a traditional Soret zone plate (left) and a self-sustained Fresnel array (right). This has been described in detail

(1) Laboratoire d'Astrophysique de Toulouse-Tarbes, Université de Toulouse, CNRS, 14 avenue Edouard Belin, 31400 Toulouse, France
(2) Département Cassiopée, Université de Nice Sophia-Antipolis, CNRS, Observatoire de la cote d'Azur, B.P. 4229, F-06304 NICE Cedex 4, France

in previous publications (Koechlin, Serre, Duchon 2005, Koechlin et al. 2008). The advantages of this new concept for astronomical imaging is two-fold : first, the incoming light converges without passing through any material. Consequently, no absorption occurs in this part of instrument, and a wide range of wavelengths (practically from 120 nm to 25 μm) would be accessible in a space-borne implementation. Second, the main aperture optical component is a light-weight and thin opaque foil with void apertures, much lighter and than an equivalent diameter telescope.

The released tolerances compared to classical optics polishing and positioning allow high quality wavefronts even at very short wavelengths. Moreover, the small weight of a Fresnel array, compared to standard optics with similar collecting power, makes this concept particularly well suited to large space-borne telescopes: from 4 to 40 meters diameter or more, with focal lengths from 400 m to 40 km that would be accessible with a two-spacecraft formation flying.

Before sending to space an instrument involving a new optical concept, it has to be qualified with ground based testbeds. In the recent years, we have built several generations of such equipment. The first two were laboratory experiments. They have validated the high dynamic range and diffraction-limited imaging capabilities on artificial sources (Serre, Deba & Koechlin, 2007; Serre, 2010 in this issue). In addition, an end-to-end dedicated numerical simulation tool has also been developed (Serre, 2008; Serre, 2010, in this issue), the results of which have been successfully compared with experimental data.

The "Generation 2" testbed under consideration in this article is dedicated to on-sky operation. It is the result of a step by step evolution. The migration stages from generation 1 to generation 2, and the work done from 2008 to November 2009 are presented in (Rivet, *et al.* 2010, in this issue). The present paper discusses the final implementation and the on-sky results obtained with the fully featured generation 2 prototype, on "well known" but difficult sky objects such as high contrast, faint, and close binary stars, or planets.

Sections 2 and 3 describe why and how we have implemented this testbed. The optical and mechanical design, and the reduction procedure are presented in Section 4. The results obtained on several sky sources (binary stars, planets and satellites, deep sky objects) are discussed in Section 5, and the outline of a future space mission is depicted in section 6.

2 Why a Generation 2 testbed ?

Although we propose this new concept for space applications with very large apertures and very long focal lengths, its validation has to be made with a limited budget, hence with a small diameter aperture and a focal length adapted to a ground-based setup. Nonetheless, the validation has to be as precise and realistic as possible.

The first laboratory testbed (Generation 1) has been successful in demonstrating the high contrast imaging capabilities of Fresnel imagers on artificial sources : 10^{-6} (Serre, 2007). This has motivated the decision to proceed further and to tackle with the broad diversity of spectra, contrasts, angular sizes and brightness offered by astronomical sources in real conditions. Indeed, it was important to assess the efficiency of this new concept in observing conditions, closer to those of a real space instrument. The goal was to prove that, even in less than ideal situations, Fresnel imagers can

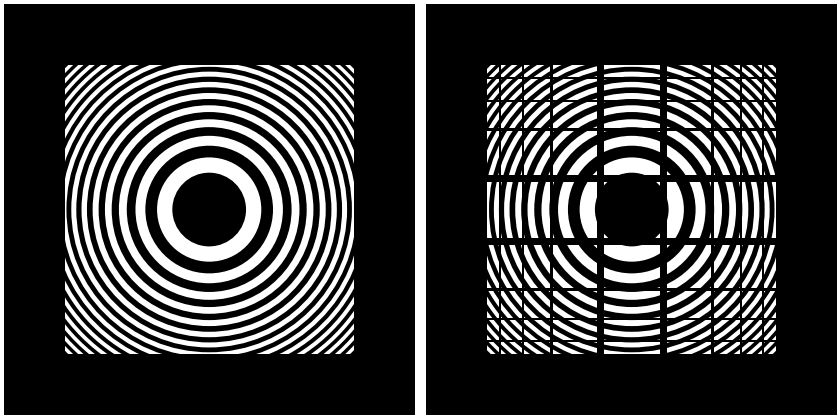

Fig. 1 *Left : Circular (Soret) zone plate. Right : an example of self-sustained Fresnel array, with* 15 *Fresnel zones (on the half diagonal). The bars holding the rings are in phase relation with them : one every* n^{th} *ring. In the Fresnel array of the Generation 2 prototype, there are* 696*-Fresnel zones and* 2×232 *bars. This corresponds to* $\simeq 250,000$ *arc-shaped holes. Some kind of apodization has also been introduced : the rings' thickness ratios vary from center to edge.*

produce astronomical images with contrast and resolution equivalent or better than classical observation means at equal aperture.

Even with a Fresnel array as small as 200×200 mm, the focal lengths are rather long, we also wanted to target sky sources without using siderostat mirrors, which are likely to hamper the incoming wavefront quality. Thus, we have chosen to use the tube of a large astronomical refractor as a giant optical bench : the Fresnel imager has been fixed in parallel alongside the 19 m long refractor's tube.

The two modules of Generation 1 testbed were modified to fit safely on the refractor's tube. The first steps of implementation started in June 2009, and the system was operational with nominal performances in October 2009.

The tests carried on with this generation 2 testbed addressed the following issues :

- angular resolution
- field width and spectral bandpass
- dynamic range
- limiting magnitude

These tests aim also to study practical problems of importance for future space-borne applications, such as the accuracy required on the relative position and attitude (orientation) of the receiver module and of the Fresnel array module, in order to have an efficient chromatic correction using a scheme adapted from (Schupmann, 1899) and (Faklis & Morris, 1989). The issue of turbulent tip-tilt and its real-time correction has also been addressed.

3 Setting up the Generation 2 testbed

The second generation testbed had to demonstrate the on-sky efficiency of the FDAI concept in real (ground-based) observing conditions. Indeed, experimental feedback

was needed on how such optical combination withstands non-ideal conditions (thermal fluctuations, mechanical flexions, vibrations, misalignments, atmospheric turbulence, poor celestial guiding). For cost - and time - efficiency, we have chosen to install the FDAI in parallel to an existing astronomical instrument, which was expected to act both as a mechanical mounting and as a reference for optical performances comparisons.

As explained in the paper presenting generation 1.5 prototype of Diffractive Fresnel Imager in the same issue, for a 200×200 mm Fresnel array, reasonable focal lengths are close to 20 m at $\lambda = 800$ nm. That is why the historical 76 cm refractor (focal length 17.89 m, tube length 19 m) of the *Observatoire de la Côte d'Azur* (Nice, France), has been chosen to hold our Generation 2 prototype. The "*grand équatorial*" was one of the largest of its time in 1887. At present, it is still fully operational and used for scientific research. Although the most recent improvements date from the 1960's, it is well maintained and has a reasonably precise drive.

3.1 Implementation constraints

Since the 76 cm diameter refractor which was available for this experiment is part of a protected historical monument, some constraints had to be taken into account when designing the mechanical interfaces between the FDAI and the tube of the refractor. Indeed, the two elements (the Fresnel array module and the receiver module) had to be assembled on the tube without any irreversible operation : no hole could be drilled in any part of the existing mechanical structure, and no historical element could be removed, if not temporarily.

Using an existing instrument as a mechanical support yields another limitation : the modules must not be too heavy. Otherwise, excessive mechanical flexions of the refractor's tube may result, and the motor drives may have insufficient torque to move the instrument correctly. The total weight of each module had to fall well below 40 kg.

Another design constraint comes from the flexions of the tube and their consequences on the chromatic correction: a correct chromatic correction requires a good alignment of the receiver module with the Fresnel array module. Since both modules are at opposite ends of a 19 m long metallic tube, a flexion of the tube results in a misalignment, and poor chromatic correction. Thus, the orientation of the receiver module with respect to the Fresnel Array needs to be fine-tuned. Moreover, the mechanical flexion of the refractor's tube varies when the instrument's orientation changes. As a consequence, the relative orientation must be corrected frequently.

All these issues have crucial influence on both the "external design" of the instrument (the way the two modules are connected to the existing refractor) and on the "internal design" (the way the optical components are arranged within each module). Both issues are discussed hereafter.

3.2 "External" design

Fig. 2 shows the overall geometry of the setup, including the refractor's tube, the Fresnel array module, and the receiver module. Both modules of the Fresnel imager are connected to the refractor's tube by massive mechanical stands, which are fastened to the tube by a pair of stainless steel belts. Those belts are stiffened by stay tensioners

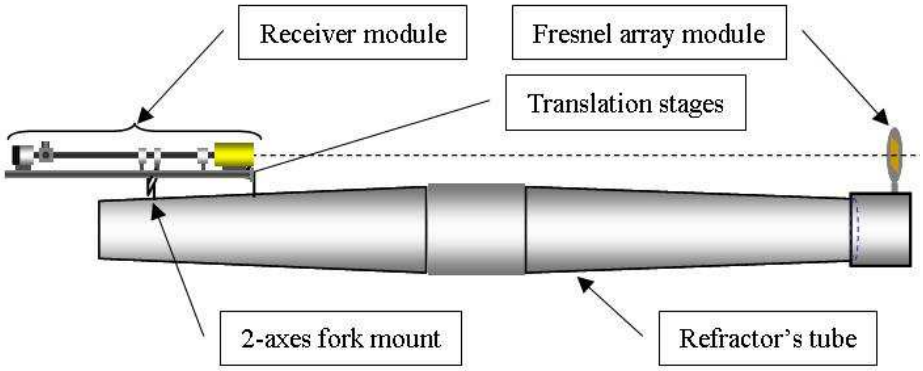

Fig. 2 *The global structure of the instrument (not to scale). The refractor's tube is* 19 *m long, and the optical rail is* 2 *m long. The optical axes of the refractor and of the Fresnel imager are parallel.*

(see Fig. 3). This mechanical solution, although fully reversible and harmless for the refractor's tube, revealed to be steady enough four our purpose.

The Fresnel array module stand is rather simple, since no runtime fine-tuning is required usually. Casually, it may happen that the diffraction spikes of the array exactly coincide with an astronomically relevant feature in the final image. In this case, the array has to be rotated around its optical axis. The mount has been designed consequently. This is the only degree of freedom that may me modified in runtime on the array module. Fig. 4 displays this module.

The receiver module is much more complex and requires an elaborate mount. Basically, this module is a 2 m long optical rail with an "X"-shaped cross section. Since it has to be oriented accurately towards the center of the Fresnel array, it cannot be rigidly connected to the refractor's tube. A good chromatic correction requires frequent correction of this module's orientation. Thus, the rail is connected to the tube by a two-axis fork mount (see Fig. 5). The intersection of those axes is supposed to be very close to the center of gravity of the receiver module, so that the module is close to a neutral equilibrium, and very few strength is needed to modify its orientation. This fork mount bears the weight of the receiver module. It is thus firmly bolted onto the refractor's tube, through the already existing mechanical interface of an auxiliary finder .

To drive smoothly and accurately the global tip-tilt motion of this module, a third stand is connected to the tube, with the same kind of steel belts as for the Fresnel array module. This stand is connected to the tip of the receiver module's optical rail through a pair of crossed electrically-operated translator stages (see Fig. 6). Thus, the orientation of the rail can be remote-controlled easily and accurately during runtime.

3.3 "Internal" design

In Fresnel imagers, the incoming light encounters first the Fresnel array, a 200×200 mm thin metallic foil with laser-carved apertures (696 apertures along a semi-diagonal). The second component on the optical path is a field optics located close to the focal plane of

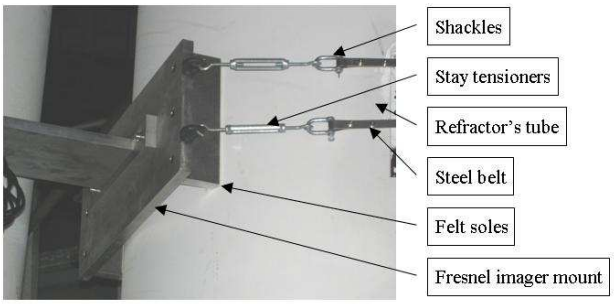

Fig. 3 *Non-destructive mounting system. The mount is fastened to the refractor's tube by two stainless steel belts, the tension of which is adjusted with four stay tensioners. The felt soles prevent damage of the refractor's coating.*

Fig. 4 *Left: the Fresnel array module on its mechanical stand. Right: the same module, mounted on the refractor's tube. The orientation of the square aperture (hence of its PSF spikes) can be adjusted by rotating the cell holding it. The cell has been rotated by* 45° *between the two figures.*

the Fresnel array (first diffractive order), 18 m downstream (see Fig. 7). This field optics is a 150 mm Maksutov telescope with 1800 mm nominal focal length. The field is limited by an off-axis 45 mm circular field stop, fitted between the central obscuration and the edge of the Maksutov aperture, and placed in front of the Maksutov meniscus. The field optics makes an image of the entrance pupil (the Fresnel Array) onto the chromatic corrector, a 58 mm fused silica blazed Fresnel lens with 702 zones. At nominal setting, each Fresnel zone of the main array is imaged upon the corresponding zone of the chromatic corrector.

The 6 additional zones of the chromatic corrector (702 compared to 696) make possible a relative shift of the pupil versus blazed lens, without vignetting, in case a linear dispersion of specified amplitude and orientation is wanted in the image plane.

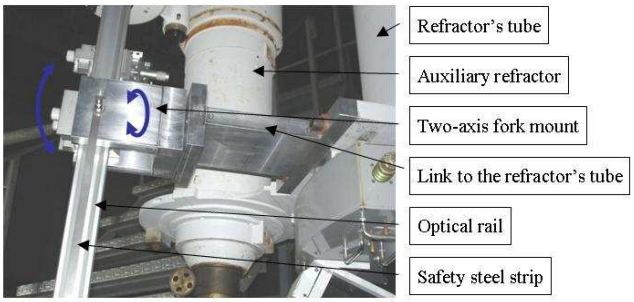

Fig. 5 *The two-axes fork mount connecting the receiver module to the refractor's tube. The foot of the fork mount is tightly bolted on an existing structure of the refractor (the sole of a former auxiliary finder).*

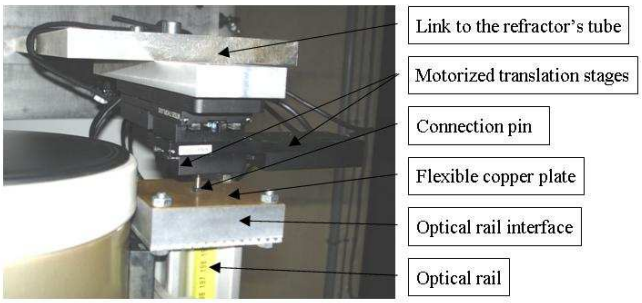

Fig. 6 *The crossed XY translator stages connecting the optical rail of the receiver module to the refractor's tube. Since the optical rail is on a fork mount, the XY translation stages acting on its upper end, modify the orientation of the whole receiver module with respect to the Fresnel array module. The fine tuning of the chromatic correction is obtained by electrically controlling these translation stages.*

The linear dispersion (or no dispersion) is set by the translations stages atop the optical rail.

Then, a custom-made doublet (diameter 64 mm, optimized for 800 nm with focal length 350 mm) produces a final image in the cameras module. This baffled module contains two identical *Andor Luca R* EMCCD cameras, one for science and one for guiding, plus a beam splitter between the science and guiding channels : a square $50.8 \times$ 50.8 mm dichroic plate with a sharp cutoff at 740 nm. The quantum efficiency of theses cameras peeks at 65% for 600 nm, and remains above 40% between 400 nm and 820 nm, and 25% at 900 nm.

Like a diffraction grating, The Fresnel array transmits light at several orders. Only the light from order $+1$ is wanted at the final focus. A proper design of the Fresnel array almost suppresses the light from orders ± 2 and all non-zero even orders. The light from order -1 is unfocussed and contributes to the background at a very low relative level of $\simeq (1/4k_{max})^2 = 1.3\ 10^{-7}$ for $k_{max} = 348$, The light from orders ± 3 and above are so dim and unfocused that they can also be neglected. However, the light from order 0, which is not focused and spread over the image plane, has to be rejected, since it would hamper the high dynamics capabilities for the instrument. For

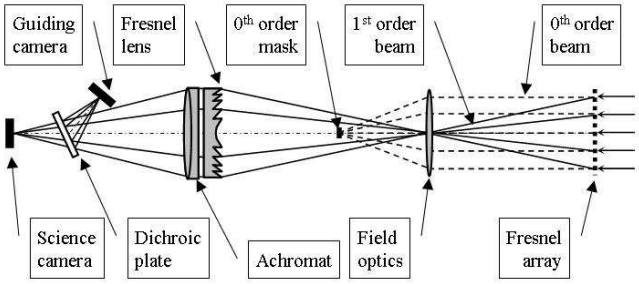

Fig. 7 *The optical scheme of the Generation 2 Fresnel imager (not to scale). The light beam from the zero order of diffraction is represented by dashed lines, whereas solid lines are used for the first order beam.*

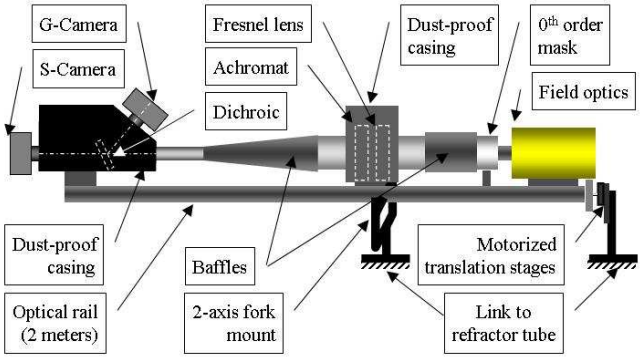

Fig. 8 *The setup of the Generation 2 Fresnel imager (not to scale). The* 45 *mm field stop (not represented) is located immediately upstream of the field optics (a Maksutov telescope).*

this sake, an opaque mask stands exactly where the order 0 light focuses, that is, in the image focal plane of the field optics. This mask is a 2 mm diameter disk, suspended to a pair of crossed 30 μm synthetic wires stretched across two diameters of a metallic barrel. In this plane, the light beam from first order has a diameter of 30 mm. Thus, the order 0 rejection mask does not block a significant amount of the scientifically relevant light. The zero order blocking setup would be slightly different for the real size space borne system. During the alignment phase, this zero order mask must be visible on the final image. Thus, it can be illuminated by a series of blue LEDs (400 nm wavelength), so as to become visible on the guiding camera (the one which receives the short wavelengths from the dichroic plate). This choice of a short wavelength to illuminate the zero order rejection mask deserves an explanation : the light focused by the Fresnel array at order 1 is chromatically corrected by the order -1 of the Fresnel lens. Thus, the blaze angle of this lens has been optimized to minimize the amount of light wasted in all diffraction orders but the order -1, at least in the nominal spectral band of the instrument (750 nm to 850 nm). Thus, in this spectral band, very few light is transmitted by the Fresnel lens at order 0. Consequently, the light from the zero order rejection mask, focused onto the camera's sensor by the order 0 of the Fresnel lens, would be too faint to be detectable. However, this doesn't hold for a wavelengths

such as 400 nm, well outside of the nominal spectral band for which the Fresnel lens has been blazed. So, this bue light reaches the camera as expected, making the zero order rejection mask clearly visible during the preliminary alignment phase.

The initial choice of the bandpass was between 750 nm and 850 nm in order to minimize the atmospheric diffusion and absorption by H_2O. In addition, seeing is also better in this band. The atmospheric O_2 absorption line at 760 nm blocks only a small part of the light, as it is relatively narrow. Some of the results presented in this article have been made in a second waveband, between 650 nm and 750 nm, for some hot objects such as Sirius-B. Finally a third set of data on nebulae (M42) has been acquired with a 12 nm bandwidth H_α filter.

For various reasons (flexions, polar misalignments, turbulence), the position of stellar images is not steady on the sensor. To compensate as much as possible for these unwanted motions, the final achromat is mounted on an XY piezzo-actuator. This actuator is driven according to the indications of the guiding camera, by a computer running a real-time PID control loop program with a fast centroid detection algorithm. The servo loop running at 100 Hz is able to compensate for mechanical drifts (flexions, sidereal guiding defects), and even for slow atmospheric tip-tilt. However, in order to smear out some inhomogeneities in the target background of the cameras, we chose to disconnect the tip-tilt corrector for part of the observation campaign. It was replaced by a software shift-and-add postprocessing algorithm.

The EMCCD cameras were chosen for their sensitivity, and their cost efficiency, but they appeared to be less than optimal for high dynamics. The choice of a more expensive backlit CCD would have greatly improved the quality of data. Indeed, the ghosts due to the diffraction patterns on the sensor and the irregularity of the target background would have been avoided. In addition, the global efficiency of the instrument would be enhanced by a anti-reflect coating on the entrance window of the camera.

All the aforementioned optical elements, except the entrance Fresnel diffractive mask belong to what we named “the receiver module” in Section 3.1.

3.4 Alignment procedure

The proper alignment of this Fresnel array system is a critical issue for high dynamics. There are two main elements that need special care : the blazed Fresnel lens which has to be superimposed to the image of the main Fresnel array through the field optics, and the the zero order mask, which has to be properly centered to play its role.

For the blazed Fresnel lens, the initial alignment procedure involves the daytime sky background to lighten the Fresnel array. Then, a lens and an eyepiece are inserted on the optical path close to final focus, to show a pupil plane downstream. Thus, both the Fresnel zones of the main array and the Fresnel zones of the blazed lens are visible in the eyepiece. The correct orientation for chromatic correction is reached when, by setting the attitude of the receiver module, the Fresnel zones of the blazed lens are seen superimposed to those of the main array. During nighttime observations, due to flexions of the refractor tube, the orientation of the receiver module needs to be fine-tuned every few minutes. As the main Fresnel array cannot be illuminated during data acquisition, the correction is based on residual dispersion (for compact objects) or moiré fringes in the pupil plane (for extended sources). In the case of a space mission, the pupil alignment will have to be maintained by a proper attitude control of the receiver spacecraft. The precision required is comparable to the angular resolution of

the field optics : a 4.5 cm aperture in our testbed, (60 cm for a space version with a 4 m membrane array).

For the zero order rejection mask, a proper alignment has to be done by night, on a stellar image. The image has to be well centered in the field. Then the zero order mask illumination LED is switched on. The mask becomes clearly visible on the guiding camera, superimposed to the stellar image. It is then easy to translate the rejection mask to center it on the stellar image, before starting the high dynamic range data acquisition.

3.5 Some issues about high dynamics

Our optical setup does not contain a coronagraphic mask. Thus, the performances in terms of dynamic range rely only on the quality of the Fresnel array's PSF, on the rejection of stray light, and on the quality of the detector. The results of the first observation has shown to which extend the sake of high dynamics is demanding in terms of the detector's quality. The structure of the detector itself was responsible for two kinds of artifacts : diffraction effects, and electronic crosstalk. The pixels of the *Andor Luca R* EMCCD sensor reflect and diffract a small part of the incident light. A fraction of this reflected/diffracted light is reflected back to the sensor by its uncoated window. Thus, bright PSFs produced spurious cross-shaped diffraction spikes, in addition to the expected spikes of the Fresnel array. Moreover, at high dynamic range, some electronic "crosstalk" between distant bright and faint pixels is responsible for background irregularities unnoticed in normal conditions. These artifacts produce unwanted non random features in the image, which cannot be eliminated by averaging. They cannot be completely eliminated by flat-fielding either, since they are linked to bright PSFs. These effets were underestimated during the prototype design phase, and as we could not afford a very high grade camera, we found workaround solutions to get rid of them, at least partially.

In order to implement the tip-tilt correction, we needed to split the light into a guiding channel and a science channel. For this, we use a dichroic plate. Our results also showed that optical filters or dichroic beam splitters usually considered of "high quality" can generate ghosts by multiple reflections. This effect, which is considered as minor for standard applications, becomes relevant when high dynamics is concerned.

To improve the dynamics, the spectral bandpass needs to be limited by filters for two reasons. First, our chromatic correction scheme is effective at all wavelengths for the light transmitted through the diffraction order -1 of this Fresnel lens. Only this light is chromatically corrected and focused on the detector. Far from its blaze nominal wavelength (800 nm), the lens transmits a small fraction of the incoming light through other orders. This uncorrected and unfocussed light is shed all over the image plane and causes a nearly uniform haze. This small fraction of the light (from 0 to 2%) is diluted over a wide area and does not significantly limit high dynamic range if the working bandpass is limited to ± 150 nm around the nominal wavelength (800 nm). Second, the longitudinal chromatism of the main Fresnel array also yield a limitation of the accessible bandpass : for wavelengths far from nominal, the first order focus of the Fresnel array is far upstream or downstream from its nominal position. This does not affect the dynamics, provided the beam is not vignetted by the field stop (a 45 mm circular hole located in front of the Maksutov telescope used as a field optics; (see Fig. 8 and section 3.3).

If vignetting occurs, a relatively bright and lower-resolution PSF is superimposed to the nominal high-resolution one. A loss in both resolution and dynamics would result. This feature requires to limit the working bandwidth to $\Delta\lambda = \sqrt{2}\lambda D/C$, where D is the diameter of the field stop at primary focus, and C the size of the square aperture. For example, a 200 mm Fresnel array and a 45 mm field stop, leads to a bandwidth limitation of $\Delta\lambda/\lambda = 30\%$, which corresponds to $\pm$120 nm around the nominal wavelength (800 nm). As we accepted some vignetting concerning the corners of the main square aperture at off-center wavelengths, the tolerance was increased to $\pm$150 nm.

To limit the bandpass properly, we have added on the optical path a long-pass filter, which eliminates wavelengths shorter than 630 nm. Wavelengths longer than 900 nm are naturally eliminated, both by atmospheric H_2O absorption, and by the waning sensitivity of the detector.

4 Data acquisition and processing

The main goal of this first set of on-sky experiments was to assess the high dynamics capabilities of the Fresnel imager. In this context, flat-field correction would have been of little interest. Moreover, they would have introduced some unwanted noise. Consequently, the raw images were only corrected for the sky background brightness.

As explained in Section 3.3, some data sets were obtained without any real-time active tip-tilt correction. For those data, we apply a shift-and-add algorithm with frame selection (lucky imaging). Let's now describe in some detail the data acquisition procedure and processing.

4.1 Data acquisition procedure

The acquisition software delivers data cubes with up to 1000 individual frames, and stores them according to the FITS image standard. For each sky target, several sequences of 10 data cubes were taken. The chromatic correction needed to be checked and sometimes fine tuned, at least every 15 minutes, due to the combined effect of mechanical flexions and atmospheric dispersion (see 3.3).

Since the sky background is high and rapidly varying, series of sky background images acquisitions were performed after each set of 10 science sequences, with the same exposure time and the same filters.

Even when the tip-tilt corrector was off, the rapidly refreshed images of the guiding camera were displayed by the guiding computer. This was useful to check for unwanted drifts of the image. Thus, if needed, the image was manually centered on during the readout phase which follows each data cube acquisition inside a sequence.

4.2 Data processing

The first step of the data processing pipeline is to process the sky background sequences of data cubes. From each data cube in a sky background sequence, one extracts a unique sky background image by a clipped averaging procedure : for each pixel of the final image, the level values of the corresponding pixel from all the individual frames in

the cube are collected and sorted. The 1% smallest and the 5% highest are considered as non significant and thus rejected. The remaining values are averaged. This procedure is performed with all the cubes in the sequence, leading to one sky background image per data cube. Then a "global sky image" is obtained by a simple averaging of the resulting individual background images.

Then, one processes the sequence of science data cubes corresponding to the sequence of sky background data just processed. For each science data cube in the sequence, the following operations are performed :

1. Subtract the master sky background image from each individual frame of the cube.
2. On a chosen reference image (not necessarily from the same data cube), determine the centroid of the brightest object. This position will be chosen as "reference point".
3. For all other frames, compute the centroid in a 50×50 to 200×200 pixels window around the reference point, and shift the frame so that the centroid coincides with the reference point. The centroids and shifts are at a 0.2 pixels or better precision.
4. Perform a clipped averaging of all recentered individual frames.

This leads to one compound image per data cube. Then, all are summed to form the science image of each sequence.

5 Results in resolution and high dynamic range

Our goal was of course not to make discoveries in astrophysics with this modest 200×200 mm aperture instrument. Our sky targets have been chosen to challenge different aspects of the Fresnel imager. We aim at sampling the "dynamic range versus angular separation" space : from the data obtained on binary stars, we measure a dynamic range for a given angular separation, then compare it to what can be expected from a numerical instrument model developed by Serre (2008). We wanted to check how close to this model we could approach on sky objects, in real observation conditions.

This instrument model is extendable to large Fresnel arrays, and shows that for 4 m arrays, dynamic ranges of 10^{-7} to 10^{-8} can be reached on raw images. For small, 200×200 mm arrays, the predicted dynamic range is around 10^{-6}.

5.1 Binaries

The results presented here are made with the 200×200 mm aperture Fresnel imager and an *Andor Luca R* EMCCD camera. The multiple star systems *BU* 893 AB and *STF* 1273 AD has been resolved. See figs. 9 and 10. They show stars with high magnitudes differences: respectively 6 and 12 at $18''$ separation, and 3.5 and 12.5 at $18''$ separation. A magnitude difference of 9 as in *STF* 1273 AD, corresponds to a brightness ratio of 4000 to 1. The other components of the multiple system *STF* 1273 are either not resolved, or out of the field.

5.2 Saturn

The planetary disk of Saturn covers $19''$, and $45''$ with its rings, It has been imaged with four of its satellites in the field : Titan, Rhea, Dione, Enceladus, which are evidenced in

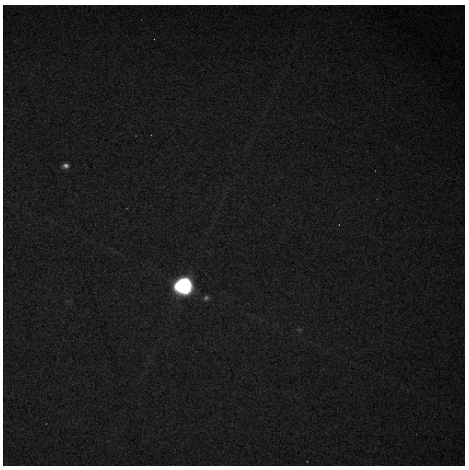

Fig. 9 *Binary star BU* 893 *AB (HR2137), with a* 6 *magnitudes difference between the central star and its companion. Image taken on January 22nd, 2010, with* 300 *s exposure time, without intensification, in the bandpass* $745 - 900$ *nm. V magnitudes* 6 *and* 12*, separation* $18''$*. The companion is well detected, although a diffraction spike of the brighter star's PSF happens to be almost exactly superposed. Several other stars are visible in the field.*

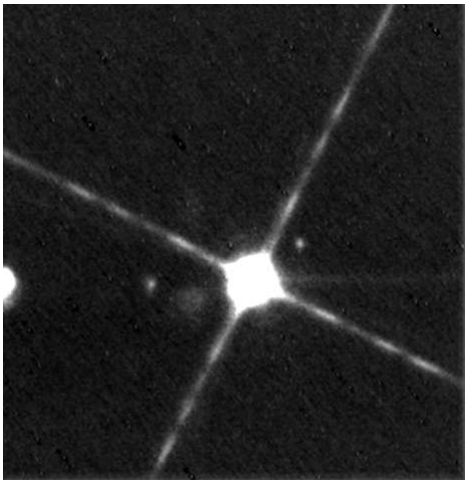

Fig. 10 *Multiple system STF* 1273*, with a* 9 *magnitudes difference between the central star and the companion on the upper right. High contrast image taken on March 14th, 2010, exposure time* 20 *s with EM intensification, bandpass* $630 - 743$ *nm. In this image, only one companion of STF* 1273*-A (magnitude* 3.5*) is shown : STF* 1273*-D : of magnitude* 12.5*, at* $18''$ *separation. The other companions are either unresolved or out of the field. The spot on the left and blobs at the left side of the image are artifacts: multiple reflections of the central star in the dichroic plate used for splitting the beam between "science" and "guiding" channels.*

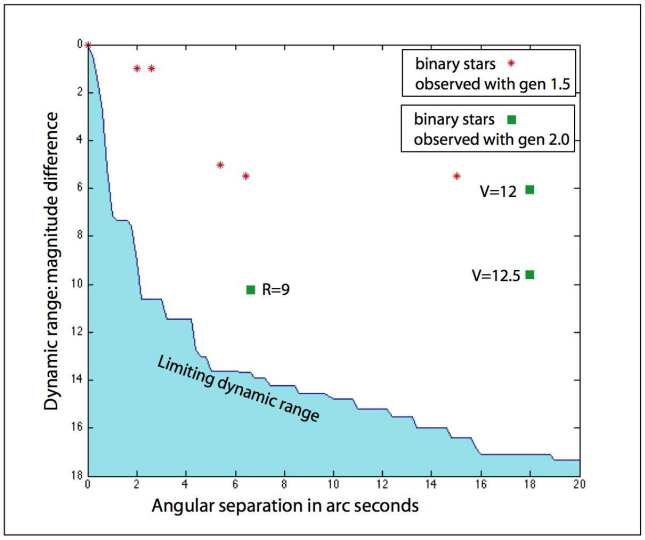

Fig. 11 *Binary stars observed with Generation 1.5 prototype (red diamonds) and Generation 2.0 (green squares). Some V and R magnitudes of the faint component star are mentioned. The curve defining the blue shaded zone below corresponds to the limiting dynamic range (in stellar magnitudes) as a function of angular separation (in arc seconds) as sampled from the numerically computed PSF of our Fresnel imager prototype.*

the same acquisition when adjusting the contrast and luminosity. Several artifacts are present: the four diffraction spikes convolved with the planetary disk, an unfocussed reflection originating from the dichroic beam-splitter, smearing from the CCD camera, and reflection from the sensor window.

6 Space mission proposed

With the successful runs of the Fresnel imager testbed at Nice observatory, the high dynamic range is validated on the sky, so is the angular resolution, but what is new now, since we have these results ? How will they impact the future development of this concept ?

We have developed the Fresnel array initially for direct imaging and spectral analysis of exoplanets (Koechlin, Serre, Duchon, 2005). There are many other ways to do that : nulling interferometry (Mariotti *et al*, 2001; Martin *et al*, 2003), coronagraphy (Trauger, J. T. and Traub, 2007), occulting masks (Cash, 2006).

Now we come up with our diffractive imaging concept, which has in fact a much broader scope than the field of exoplanets, but this is not to our advantage : at present, the rationale of space agencies is to start from a problem to be solved, then launch into space a spacecraft designed with the best suited solution for this problem, and not the other way around : to start from a solution : launch a new technology instrument, then expect observing run proposals to explore the related problems (science cases) that it could solve! As far as we know, this second situation has occurred only for a

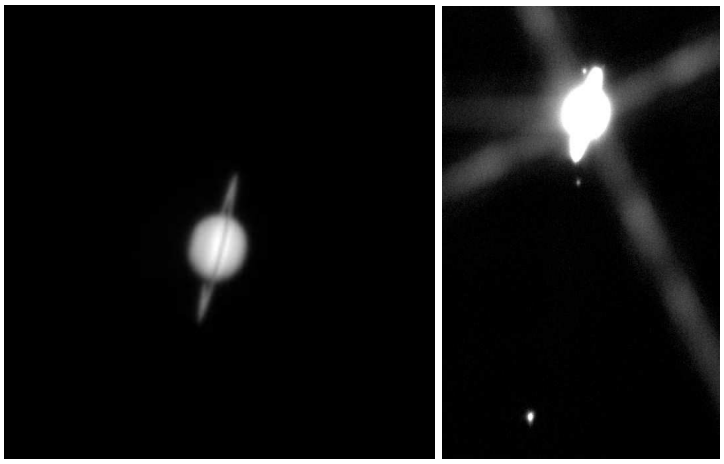

Fig. 12 *Disc of Saturn and rings.* 200 *exposures of* 0.2 *s each averaged, taken on February 13th, 2010 at* $01:15$ *UT with the* 200×200 *mm aperture diffractive Fresnel imager, equipped with an* Andor Luca R *EMCCD camera. Satellites of Saturn are visible on the same data set, using a square root brightness scale : Titan at the bottom, Dione below the rings, Rhea on the upper left, and Enceladus appearing on the upper right, close to the rings. Spectral bandpass* $650 - 663$ *nm.*

few very large projects such as LISA or PLANCK, involving worldwide cooperation, and thoroughly tested, space qualified optical concepts.

Although, to our point of view, both approaches are complementary, the second is more risky, but has better chances to bring unexpected and important discoveries. Space agencies don't take risks, and we understand it, so we plan to propose a well defined mission for this yet unqualified concept in space : this mission will be centered on UV science cases. The UV domain is rich in puzzling objects such as very young planetary systems, and the interstellar medium in which they f orm (Gomez de Castro *et al.* 2006). It is also suitable for the study of exoplanets atmospheres, as proposed by Lecavelier des Etangs and Ehrenreich (2005).

Furthermore, the UV domain has been very little explored at high angular resolution, as the large existing space telescopes were not diffraction-limited. This is no longer the case if a large (e.g. 4 meters) Fresnel imager, is launched in space: its high wavefront quality would provide unprecedented angular resolution and dynamic range in the UV. A 4 m aperture Fresnel imager in orbit around L2, with a 7 mas resolution and 10^{-6} dynamic range, should remain within the cost limits of an "M-class" ESA mission that could be launched in the 2025s.

A generation 3 prototype for concept validation in the UV is under construction, and the optical scenarios for space are reviewed in (Deba, Etcheto, Duchon, 2010, in this issue).

Fresnel imagers have two hurdles to overcome before they can be considered seriously by space agencies : show the formation flying requirements they imply are less stringent than in other projects, and show the 7% throughput of the main aperture can be compensated by an increased size at equal price. This can be done with intermediate steps.

The first of these two items could be dealt with, by a micro-satellite mission of a few days or weeks in low orbit, having the optical aperture and inter-module distance comparable to our generation 2 testbed, but free flying and involving the most basic formation flying system.

The second item : developing large membrane diffractive arrays at reasonable cost, is presently under study by ESA contractors in ground-based facilities.

7 Conclusion

We have proven now that for astronomical applications, Fresnel imagers behave honorably compared to classical optics of the same size : for example with the fact that we have imaged the two satellites of Mars with a 200×200 mm aperture Fresnel imager. This does not prove that it would not have been feasible with classical optics of the same size, but as far as we know, it had only been done before with telescopes 300 mm or larger in diameter.

Future developments regard both ground-based and space-borne projects. The UV domain is one possible niche for a first space mission using this young concept.

Most important to us is cooperation, specially with people concerned by the potential science cases in astrophysics that this new concept opens : solar system objects, stellar physics, reflection nebulae, accretion disks and planetary systems formation, exoplanet study and detection of life, Active Galactic Nuclei, and the many other fields of science that may be opened.

Acknowledgments

This work has been funded by CNES, Université de Toulouse, CNRS, Fondation STAE, and made possible thanks to the involvement of many people at Observatoire Midi Pyrénées and Observatoire de la Côte d'Azur. We are specially thankful to Jacqueline Platzer, Driss Kouach, Bruno Dubois, Marcel Belot, Marin Cortial, Jean-Jacques Bois, Carine Marchive, Thierry Mallet, and the "Service de Mécanique Mutualisé" at the Observatoire de la Côte d'Azur.

References

1. Cash W. : Detection of Earth-like planets around nearby stars using a petal-shaped occulter, *Nature* **442**, 51–53 (2006).
2. Faklis, D. Morris G. M. : Broadband imaging with holographic lenses, *Optical Engineering* **28**(6), 592–598 (1989).
3. Gomez de Castro A.-I., Lecavelier A., D'Avillez M., Linsky J. L., Cernicharo J.: UV Capabilities to Probe the Formation of Planetary Systems : From the ISM to Planets, *ApSS*, **303**, 33–52, (2006).
4. Koechlin L., Serre D. Duchon P. : High resolution imaging with Fresnel interferometric arrays : suitability for exoplanet detection, Astron & Astroph **443**, 709–720 (2005).
5. Koechlin L., Serre D. Deba P. : Fresnel interferometric arrays for space-based imaging : testbed results, in "UV/Optical/IR Space Telescopes : Innovative Technologies and Concepts III", H. A. MacEwen J. B. Breckinridge Eds., SPIE Proc. Vol. 6687, San Diego, (August 2007).
6. Koechlin L., Serre D., Deba P., Pellò R., Peillon C., Duchon P., Gomez de Castro A.I., Karovska M., Désert J.M., Ehrenreich D., Hebrard G., Lecavelier des Etangs A., Ferlet R., Sing D., Vidal-Madjar A.: The fresnel interferometric imager Exp Astron **23**, 379–402 (2009)

7. Lecavelier des Etangs A., Ehrenreich D. : A large UV-optical telescope for characterization of the atmospheres of extrasolar planets and satellites, 39th ESLAB Symposium on Trends in Space Science and Cosmic Vision 2020, 19-21 April 2005, Noordwijk, The Netherlands. Favata F., Sanz-Forcada J., Gimènez, È., Battrick B. Eds., ESA SP-588. European Space Agency, 73L, (2005).
8. Martin S. R., Gappinger R. O., Loya F. M., Mennesson B. P., Crawford S. L. Serabyn E. : A midinfrared nuller for Terrestrial Planet Finder : Design, progress, and results, in "Techniques and Instrumentation for Detection of Exoplanets", D. R. Coulter Ed., SPIE Proc. Vol. 5170, 144–154, (2003).
9. Ollivier M., Mariotti J.-M., Léger A., Skulic P., Brunaud J. Miche G. : Nulling interferometry for the DARWIN space mission, *Comptes Rendus de l'Académie des Sciences - Series IV - Physics* **2**(1), 149–156, (2001).
10. Schupmann L. : Die medial-fernrohre: eine neue konstruktion für grosse astronomische instrumente, Teubner B G, (1899).
11. Serre D., Koechlin L. Deba P. : Fresnel Interferometric Arrays for space-based imaging : testbed results, SPIE Proc. Vol. 6687-OI, (2007).
12. Serre D. : L'imageur interférométrique de Fresnel : un instrument pour l'observation à haute résolution angulaire, Ph.D. thesis, Université Toulouse III, (2007).
13. Soret J.-L. : Sur les phénomènes de diffraction produits par les réseaux circulaires, *Archives des Sciences Physiques et Naturelles* **52**, 320–337, (1875).
14. Trauger, J. T. Traub, W. A. : A laboratory demonstration of the capability to image an earth-like extrasolar planet, *Nature* **446**, 771–773, (April 2007).

Appendix D

A space Fresnel Imager for Ultra-Violet Astrophysics: example on accretion disks

Submitted to Experimental Astronomy 2010

Noname manuscript No.
(will be inserted by the editor)

A space Fresnel Imager for Ultra-Violet Astrophysics : example on accretion disks

Truswin Raksasataya[1], Ana-Ines Gomez de Castro[2], Laurent Koechlin[1], Jean-Pierre Rivet[3]

the date of receipt and acceptance should be inserted later

Abstract The Fresnel Diffractive Imager concept is proposed for space borne astronomical imaging at Ultra-Violet wavelengths, using diffractive focalization. The high angular resolution and high dynamic range provided by this new concept makes it an ideal tool to resolve circumstellar structures such as disks or jets around bright sources, among them, pre-main sequence stars and young planetary disks.

The study presented in this paper addresses two different configurations of Fresnel diffractive imagers : a large one, which involves a 20 meter "Fresnel array" featuring 2000 Fresnel zones, and a small one, whose diffractive array is 4 meters large, with 696 Fresnel zones. The diffractive arrays are opaque foils punched with a large number of void subapertures with carefully designed shapes and positions. In the proposed space missions, these punched foils would be deployed in space. Depending on the size of the array and on the working spectral band, the focal length of such imagers will range from a few kilometers to a few tens of kilometers. Thus, such space mission requires a formation flying configuration for two satellites around the L2 Sun-Earth Lagragian point.

In this article, we investigate numerically the potential of Fresnel arrays for imaging circumstellar dust environments. These simulations are based upon a simple protostellar disk model, and on the computed optical characteristics of the instrument.

1 Introduction

The Fresnel Diffractive Array Imager (FDAI) is based on the Fresnel Zone Plate concept (Soret, 1875). It has been proposed in 2005 for space imaging (Koechlin, Serre, Duchon, 2005), (Koechlin *et al.*, 2009) and tested with laboratory breadboard designs (Serre 2007, 2009). It is also described elsewhere in this special issue (Koechlin *et al.* 2010), (Deba 2010), (Rivet *et al.* 2010).

(1) Laboratoire d'Astrophysique de Toulouse-Tarbes, Université de Toulouse, CNRS, 14 avenue Edouard Belin, 31400 Toulouse, France.
(2) Fac. de CC Matematicas, Universidad Complutense de Madrid, 28040 Madrid, Spain
(3) Université de Nice Sophia-Antipolis, CNRS, Observatoire de la Côte d'Azur, Département Cassiopée, B.P. 4229, F-06304 NICE Cedex 4, France

For the sake of self consistency of the present paper, we recall here some basic facts and formula related with Fresnel diffractive imagers. A Fresnel imager has a wavelength-dependent angular resolution :

$$R_{airy} = \frac{\lambda}{D}, \tag{1}$$

which similar to that of a square aperture telescope of equivalent size. The focal length of a FDAI depends on the linear size ϕ of the array, on the wavelength λ, and on k_{max}, the number of Fresnel zones from center to corner according to the following formula :

$$f = \frac{\phi^2}{8k_{max}\lambda} \tag{2}$$

For example, a "large" 20 m FDAI, with 2000 Fresnel zones from center to corner will have a focal length of 66 km at 250 nm, and 140 km at 120 nm. A "small" 4 m FDAI with 700 Fresnel zones will have a focal length of 11 km at 250 nm, and 24 km at 120 nm.

For several reasons, FDAI's are most valuable for UV imaging. First, the light is focused without any absorption or reflection loss (the focuser only involves void holes). Second, the light focused by a FDAI has a wave front quality which is independent of the wavelength. If the diffractive array is manufactured according to the desired specifications, the resulting image is diffraction-limited at all wavelengths. Thus, working with smaller wavelengths will increase the resolution limit without hampering the image quality. Furthermore, diffraction focussing provides high dynamic range that is otherwise difficult to reach in UV, and will allow to map disks around stars without having to use coronagraphs that simultaneously block the stellar radiation and the most interesting inner region of the disk.

As a consequence, protostellar disks around Pre-Main Sequence (PMS) stars are natural candidates for diffractive imaging studies. Indeed, intermediate mass ($2 - 10$ $M_\odot$) PMS stars, also known as Ae/Be Herbig (HAeBe) stars have effective temperatures in the range 10 000 K – 25 000 K and emit the bulk of their radiation in the UV domain. They are also significantly more luminous than solar-type PMS stars. High resolution and high dynamics images in the UV domain are likely to help understanding the structure and evolution of such objects.

In this article, we address some questions related to the observability of such stellar environments with space borne FDAI's. To be more specific, we present numerical simulations on how various FDAI configurations would render the structure of a protostellar disk. For this sake, we use a standard stellar dust environment model, and compute the light intensity distribution which would result from stellar light diffusion within this dust (Sect. 2). Then, we compute the focal image a "small" 4 m FDAI or a "large" 20 m FDAI would produce from this light distribution (Section 3). Finally, conclusions are drawn about the observability of protostellar disks with UV space borne FDAI's (Section **??**).

2 Disk Model

Protostellar disks are angular momentum reservoirs generated during star formation to store the angular momentum excess associated with gravitational collapse of rotating

clouds (see *e.g.* Yorke & Bodenheimer 1998). Disks are heated by the release of gravitational energy in the accretion process and also by stellar irradiation. The gravitational energy is mainly released in the disk midplane while the stellar radiation is absorbed through the atmosphere; this gives rise to a vertical temperature inversion over most of the disk and an "overheated" dusty atmosphere (D'Alessio *et al* 1999). UV photons are absorbed in the dusty atmosphere (see van Zadelhoff *et al* 2003). Thus for this modelling we should only consider the UV radiation produced by the scattering of UV photons in the disk atmosphere, i.e., above one scale height in the disk.

We assume an inner and outer disk radius of 0.2 AU and 800 AU respectively, and a stellar mass $M = 5$ M$_\odot$ as in Hayashi (1981). The intensity of the UV radiation field is $540 \times G_0$ at the stellar surface, where G_0 is the intensity of the UV background (Draine 1978). The dust is assumed to have uniform properties all over the disk : same optical properties and constant size $a = 0.5$ μm. Grains are assumed to be spherical and to have a mass of 0.5 10^{-12}g. The local number density of dust grains is derived from the standard accretion disks mass distribution assuming a gas-to-dust mass ratio of 100.

2.1 Vertical density distribution in accretion disks

Following the standard model for α-accretion disk (Lynden-Bell & Pringle 1974), the vertical distribution of matter is given by :

$$\rho(r,z) = \rho_0(r) \exp\left(-\frac{z}{H(r)}\right)^2 \quad \left[\mathrm{g/cm^3}\right] \tag{3}$$

where r and z are the cylindrical coordinates of any given point in the disk, $\rho_0(r)$ is the matter density in the mid-plane at distance r from the star and $H(r)$ is the vertical scale height. If the gravitational field is dominated by the star, the disk thickness can be readily derived as $H(r) = c_s(r)/\Omega(r)$ where $\Omega(r)$ is the Keplerian angular velocity of the material orbiting in the disk at a radius r :

$$\Omega(r) = (GM)^{\frac{1}{2}}\, r^{-\frac{3}{2}} = 2\pi \left(\frac{M}{M_\odot}\right)^{\frac{1}{2}} \left(\frac{r}{1\,\mathrm{AU}}\right)^{-\frac{3}{2}} \quad \left[yr^{-1}\right], \tag{4}$$

and $c_s(r)$ is the local sound velocity :

$$c_s(r) = \sqrt{\frac{\gamma k_B T(r)}{\mu\ m_H}}. \tag{5}$$

Here, γ stands for the adiabatic index, μ is the mean molecular weight (2.34 as for a molecular H_2 disk) and m_H is the mass of a hydrogen atom. Consequently, a simple expression can be derived for $H(r)$, in terms of the disk temperature law $T(r)$:

$$H(r) = \left(\frac{\gamma r^3 k_B T(r)}{GM\mu\ m_H}\right)^{\frac{1}{2}} \tag{6}$$

The temperature in the mid-plane of and α-disk is given by :

$$T(r) = 127.8\,\mathrm{K} \times \left(\frac{\dot{M}}{10^{-8} M_\odot/\mathrm{yr}}\right)^{\frac{1}{4}} \left(\frac{M}{M_\odot}\right)^{\frac{1}{4}} \left(\frac{r}{1\mathrm{AU}}\right)^{-\frac{3}{4}} f(r) \tag{7}$$

where $\dot{M}$ is the accretion rate, $M_\odot$ and $R_\odot$ are the solar mass and radius, respectively and $f(r) = \left(1 - \left(\frac{R_*}{r}\right)^{\frac{1}{2}}\right)^{\frac{1}{4}}$ which is $\simeq 1$ for $r > 0.4$ AU, which is the only relevant case for this study. Henceforth :

$$H(r) = 2.26\ 10^{11}\ \mathrm{cm}\ \times\ \left(\frac{\dot{M}}{10^{-8} M_\odot/\mathrm{yr}}\right)^{\frac{1}{8}} \left(\frac{M}{5\,M_\odot}\right)^{-\frac{3}{8}} \left(\frac{r}{1\mathrm{AU}}\right)^{\frac{9}{8}} \tag{8}$$

2.2 Radial distribution of the column density

In steady accretion disks, the radial mass flow is constant and the disk surface density $\Sigma(r)$ is prescribed by the disk viscosity $\nu(r) = \alpha c_s(r)\, H(r)$ as follows :

$$\Sigma(r) = \frac{1}{\nu(r)} \frac{\dot{M}}{3\pi} f(r)^4 \quad \left[\mathrm{g\ cm^{-2}}\right] \tag{9}$$

Thus :

$$\Sigma(r) = 28.32\ \mathrm{g\ cm^{-2}}\ \times\ \left(\frac{\dot{M}}{10^{-8} M_\odot/\mathrm{yr}}\right)^{\frac{3}{4}} \left(\frac{M}{5\,M_\odot}\right)^{\frac{1}{4}} \left(\frac{r}{1\mathrm{AU}}\right)^{-\frac{3}{4}}. \tag{10}$$

The density in the disk midplane can thus be approximated by :

$$\rho_0(r) = \frac{\Sigma(r)}{H(r)} \tag{11}$$

which yields, after some algebra,:

$$\rho_0(r) \simeq 12.5\ 10^{-12}\ \mathrm{g\ cm^{-3}}\ \times\ \left(\frac{\dot{M}}{10^{-8} M_\odot/\mathrm{yr}}\right)^{\frac{5}{8}} \left(\frac{M}{5\,M_\odot}\right)^{\frac{5}{8}} \left(\frac{r}{1\mathrm{AU}}\right)^{-\frac{15}{8}} \tag{12}$$

For a Ae Herbig star, fiducial values are : $\alpha = 0.01$, $M = 5 M_\odot$, $\dot{M} = 10^{-8}\ \mathrm{M_\odot\ yr^{-1}}$.

2.2.1 Fiducial distribution of dust grains

Assuming a gas-to-dust ration of 100 and a The number density of dust grains, $N_d(R, z)$ is directly derived from $\rho(R, z)$ as follows :

$$N_d(R, z) = \frac{\rho(R, z)}{\eta m_d}$$

where η is the gas-to-dust mass ratio, and $m_d = 0.5\, 10^{-12}$ g is the mass of the dust grains. This yields :

$$N_d(r, z) = 0.25\ \mathrm{cm^{-3}}\ \times\ \left(\frac{\dot{M}}{10^{-8} M_\odot/\mathrm{yr}}\right)^{\frac{5}{8}} \left(\frac{M}{5\,M_\odot}\right)^{\frac{5}{8}} \left(\frac{r}{1\mathrm{AU}}\right)^{-\frac{15}{8}} \exp^{-\left(\frac{z}{H(r)}\right)^2} \tag{13}$$

with $H(r)$ given by Equation (8). For more realism, we assume that the dust grain density vanishes for $r < R_{in} = 10$ AU (inner disk radius). Indeed, at the center of the disk is located the protostar (not represented in the images below), the strong radiation of which evaporates the dust grains located at distances smaller than the "inner radius" of the disk. The highest density of dust is found at distances just above the inner radius. Above $r > R_{out} = 100$ AU (outer disk radius), the dust grains have a very low density. They will not be considered in ou light diffusion model.

2.3 Ray tracing

In our simplified model, only single light scattering by dust grains is considered (no multiple diffusion). Thus, all the dust grains receive light from the star only. The disk is discretized into finite elements within a cylindrical coordinate system centered on the star and with reference z axis along the disk axis.

For each finite element, we compute the amount of start light received by each dust grain, assuming that no absorption occurs between the star and the dust grain. The light intensity diffused towards the observer is then computed according to the Henyey-Greenstein (1941) diffusion model :

$$I_{Scat} = \frac{I_0}{r^2}\, \pi a^2\, \phi(\theta)\, N_d(r,z) \tag{14}$$

where

I_{Scat}	=	scattered light intensity (W.sr^{-1}).
I_0	=	incoming light intensity (W.sr^{-1}).
a	=	radius of dust grain.
r	=	distance of dust from central protostar
θ	=	diffusion angle (see Figure 1).
$\phi(\theta)$	=	diffusion factor.
$N_d(r,z)$	=	dust density.

In this model, the diffusion factor (or scattering phase function) $\phi(\theta)$ is :

$$\phi(\theta) = \frac{1-g^2}{4\pi \times (1+g^2-2gcos\theta)^{3/2}} \tag{15}$$

where g is the scattering phase function asymmetry. It varies from -1 to $+1$. When $g = -1$, all the incoming light is scattered back to the star. For $g = 0$, the light is diffused isotropically. For $g = +1$, the light goes forward "through" the dust grain as if it were fully transparent. The anisotropy factor g is wavelength dependent in the most general case. However, we assume it can be considered as constant within the observing bandpass. Finally, the scattered radiation is projected onto a plane perpendicular to the line of sight, so as to construct the 2D luminosity maps, seen by the observer. This luminosity map is used as an input to compute the final image a Fresnel imager would produce, and thus, to study of the expected performances of Fresnel Imagers on protostellar disks.

It is worth noting that not all points in the disk volume need to be considered, since the scattering of UV photons only occurs in the outer layers of the disk atmosphere, namely in the so-called "Photo Dissotiation Region" (PDR).

The UV radiation is absorbed by H_2 molecules, leading to the formation of a photodissotiation front into the disk and leaving a photoevaporative flow behind. We do not attempt to model the dense and optically thick layers of the disk, henceforth a limiting column density is used to define the frontier of the optically dense regions, which is supposed to receive no star light (and thus to diffuse no light). Sabine *et al.* (1999), proposes 50 cm^{2}g^{-1} as a threshold on the column density. In each volume element of our disc model, we compute the local dust density, and from it we get a local absorption factor, that we apply to the light traveling to the observer.

Notice that, this simple model is not intended to give a fully realistic image of protostellar discs, but only to provide test images for a performance assessments.

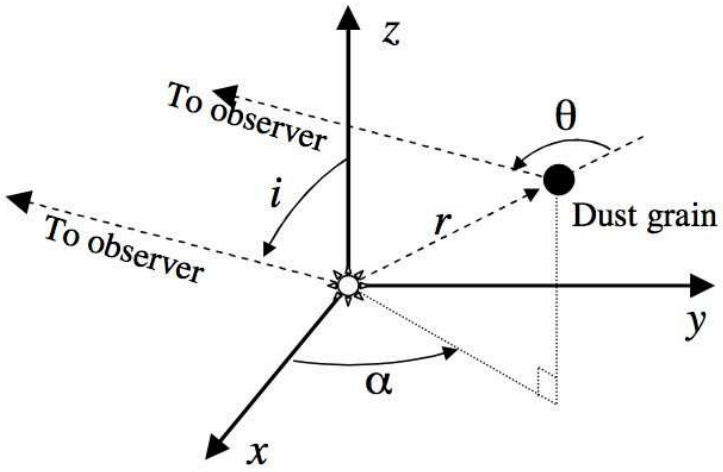

Fig. 1 illustrates the scattering of light by a dust grain at distance r from the star. θ is the diffusion angle. The observing direction lies in the (x, z) plane.

Figures **??** and **??** show various aspects of an accretion disk depending on the optical properties of the dust grains it contains. These properties are characterized by the value of the anisotropy parameter g in the Henyey-Greenstein equation. The different images show how the scattering parameter g influences the projected image of the disk.

To summarize, the following parameters control this step of the process:

- the inner and outer radii of the disk R_{in} and R_{out},
- the scale height of the disk H,
- the dust density as a function of z and r_{xy},
- the inclination of the disk plane with respect to the line of sight.
- the diffusion anisotropy parameter g.

3 Convolution and model perspective

The disk simulation code used here produces 2D "raw images" of the accretion disks. To assess the performances of the Fresnel imager, we convolve these 2D maps with the point spread function (PSF) of the instrument. The following parameters control this step of the process :

- angular resolution of the instrument (obtained from aperture size and wavelength),
- distance of the protostar system.

The PSF used is given by an independent numerical propagation software, dedicated to the Fresnel imager and developed by Serre (2010), published elsewhere in this special issue. This software performs an end-to-end Fresnel propagation of light from a point source at infinity, passing through all the diffractive and refractive optical elements encountered on its way to the final image.

The convolution of a 2D disk map by this PSF yields the simulated image of an accretion disk, as it would be seen with a Fresnel imager.

Parameter	Value	Unit
Stellar mass	0.5	$M_\odot$
Luminosity	1	$L_\odot$
Mass loss	10^{-8}	$M_\odot$/ year
Distances from observer	1 to 10	kiloparsecs
Disk inner radius	0.2	A.U.
Disk outer radius	300	A.U.
Henyey-Greenstein param. for dust	0.6	
Main Fresnel array aperture	4×4	m
Observation wavelength	121	nm
angular resolution	7	milliseconds of arc

Table 1 Disk model parameters and specifications of simulated object and image in figures 2 and **??**.

Specifications	Proposed Fresnel Imager	Future large project
Array size	4 m	20 m
Fresnel zones	700	3000
Field optics diameter	0.68 m	3 m
Bandpasses	$120-150$nm and $200-260$nm	$120-150$nm and $200-260$nm
Resolution at 121 nm	$0.0062''$	$0.0012''$
Field at 121 nm	$5.9''$	$4.5''$

Table 2 specifications for two possible Fresnel Space Imagers. The 4 m configuration is proposed for the ESA "Cosmic Vision" call for 2020-2022 as a class "M" mission.

The Fresnel Diffractive Array Imager can be built in various configurations according to the science cases, hence with various angular resolutions, dynamic ranges, and wavebands. As an example, the specifications in the left column of table 2 are proposed for a mission to be launched around 2025 : A 4 m Fresnel array at 121 nm, having an angular resolution of 7 milli arc seconds (mas). On the right column, we present an ambitious project for a possible further space mission, that could also operate in the visible and IR bands.

In figs.2 and **??**, we show the images that could be obtained with the dust disk parameters shown in table 1, and the 4 m configuration of table 2. We have built the dust disk object from the code described in the above sections, developed by ourselves and based on an irradiated α-disk model and the parameters in table 1.

For fig. **??**, the raw disk objects have been created with the same parameters as above, except for stellar masses and luminosities : a 1 $L_\odot$ central star to account for a solar type T-Tauri, and a 10 $L_\odot$ for a Herbig type central star, still using a numerical model based on Yorke & Bodenheimer (1999). The dust disks of this latter figure are processed with a commercial ray tracing software. Here the disk flaring produces the illumination of the most external rings. The dramatic external ring is caused by the ray tracing discretization (it is not smooth enough in the outer parts of the disk).

In all cases, the illuminated dust disk projected on the sky plane is fed to the convolution code, developed by ourselves, to yield the final image that would be obtained with a Fresnel imager.

4 Conclusion

Although these models could be developed to take into account more complex mechanisms and more precise ray tracing, to better handle details of disks and jets, they are useful for assessing the observation of protostellar disks at different distances.

This study shows that with a 4m aperture Fresnel array operating at 121 nm, protostellar discs up to distances of 10 kiloparsecs can be imaged with enough detail to show the extension and orientation of the disk (but a 20 m Fresnel array would be required to show the inner radius, even at small distances). This 10 kpc limit allows to study in detail the Gould's Belt at $140 - 160$ pc, where prominent star forming regions such as Taurus, Lupus, and Ophiuchus are located.

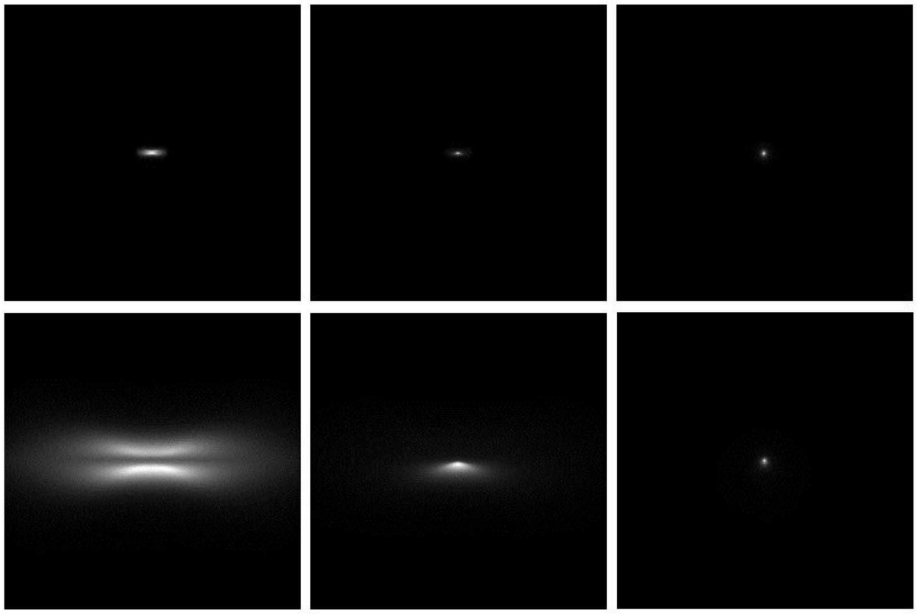

Fig. 2 Simulated accretion disk images based on an irradiated α-disk model with : 0.5 $M_\odot$ star, Henyey-Greenstein factor $g = 0.6$, inclination angles $i = 80°,\ i = 60°,\ i = 30°$, from sky plane, distance 10 kiloparsec (top) , and 1 kiloparsec (bottom). The images shown are obtained by convolution of the projected disk models with the PSF of a 4 m aperture Fresnel array operating at 121 nm, having an angular resolution of 7 milli arc seconds.

Acknowledgments

This work has been funded by Thales Alenia Space, Université de Toulouse, and CNRS, AIG research is supported by the Ministry of Education and Science of Spain through grant: AYA2008-6423-c03. We specially thank Denis Serre for letting us use the propagation code that he has developed and used for his Ph.D. work and his publications.

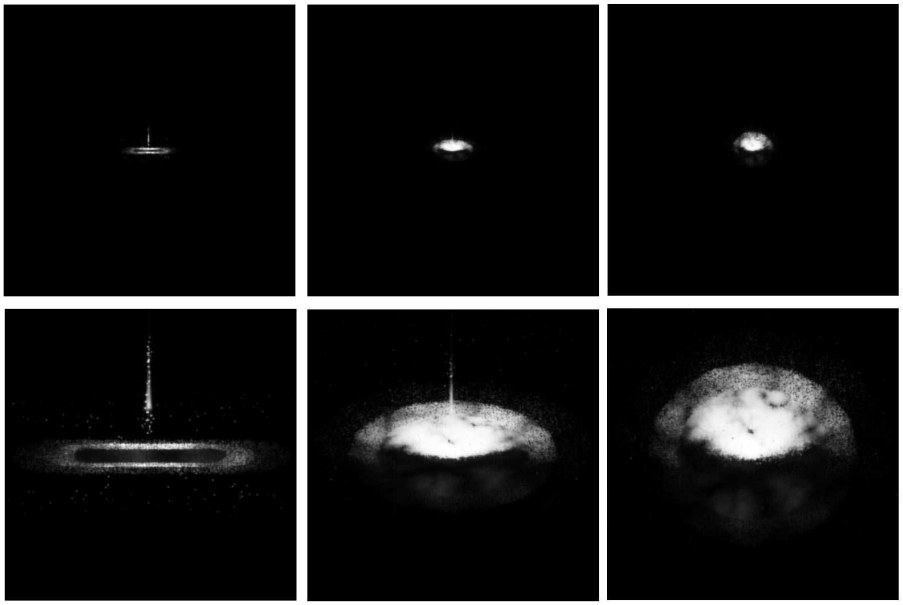

Fig. 3 Simulated accretion disk images based on the same parameters as fig. 2, inclination angles $i = 90°$, $i = 60°$, $i = 30°$, from sky plane, distance 10 kiloparsec (top) , and 1 kiloparsec (bottom). The images shown are obtained by convolution of a ray-tracing software output with the PSF of a 4 m aperture Fresnel array operating at 121 nm, having an angular resolution of 7 milli arc seconds.

References

1. D'Alessio P., Calvet N., Hartmann L., Lizano S., Cant J. : Accretion Disks around Young Objects. II. Tests of Well-mixed Models with ISM Dust, *Astrophysical Journal*, **527**(2), pp. 893–909, (1999).
2. Deba P. : The Fresnel Imager : Preparing the way to space borne Fresnel Imagers, *Experimental Astronomy*, to appear in this special issue, (2010).
3. Draine B.T., : Photoelectric heating of interstellar gas, *Astroph. J. Suppl*, **36**, pp. 595–619 (1978).
4. Hayashi C. : Structure of the Solar Nebula, Growth and Decay of Magnetic Fields and Effects of Magnetic and Turbulent Viscosities on the Nebula, *Prog. Theor. Phys. Suppl.*, **70**, pp. 35–53, (1981).
5. Henyey L. G. and Greenstein J. L.. : Diffuse Radiation in the Galaxy. *Astrophysical Journal*, **93**, pp. 70–83, (1941).
6. Koechlin L., Serre D., Duchon P. : High resolution imaging with fresnel interferometric arrays : suitability for exoplanet detection, *Astronomy & Astrophysics* **443**, pp. 709–720, (2005).
7. Koechlin L., Serre, D., Deba P., Pelló R., Peillon C., Duchon P., Gomez de Castro A. I., Karovska M., Désert J.-M., Ehrenreich D., Hebrard G., Lecavelier Des Etangs A., Ferlet R., Sing, D., Vidal-Madjar, A. : The fresnel interferometric imager, *Experimental Astronomy* **23**, p. 379, (2009).
8. Koechlin L., Rivet J.P., Deba, Raksasataya T., Gharsa T., Gili R. : Fresnel Imager tetbeds : setting up, evolution, and first images, *Experimental Astronomy*, to appear in this special issue, (2010).
9. Lynden-Bell D. & Pringle J. E. : The evolution of viscous discs and the origin of the nebular variables, *Mon. Not. R. Astron. Soc.*, **168**, pp. 603–637, (1974).

10. Richling S. Yorke H.W. : Photoevaporation of Protostellar Disks V. Circumstellar Disks under the Influence of Both Extreme-Ultraviolet and Far-Ultraviolet Radiation, *Nature*, **186**, p. 958, June 1960.
11. Rivet J.P. Koechlin L., Deba P., Raksasataya T., Gili R. : Generation 2 testbed of Fresnel Imager : first results on the sky, *Experimental Astronomy*, to appear in this special issue, (2010).
12. Serre, D. : LImageur Interférométrique de Fresnel : un instrument spatial pour lobservation à haute résolution angulaire, PhD thesis, Université Paul Sabatier, Toulouse (France), (2007).
13. Serre, D., Deba, P. Koechlin, L. : Fresnel Interferometric Imager : ground-based prototype, *Applied Optics* **48**(15), pp. 2811–2820, (2009).
14. Serre, D. : The Fresnel Imager : Instrument Numerical Model, *Experimental Astronomy*, to appear in this special issue, (2010).
15. Soret, J.-L. : Sur les phénomènes de diffraction produits par les réseaux circulaires, *Archives des Sciences Physiques et Naturelles*, **52**, pp. 320-337, (1875).
16. van Zadelhoff G.J., Aikawa Y., Hogerheijde M.R., & van Dishoeck E.F. : Axi-symmetric models of ultraviolet radiative transfer with applications to circumstellar disk chemistry, *Astron & Astroph*, **397**, p. 789, (2003).
17. Yorke H. W., and Bodenheimer P. : The Formation of Protostellar Disks. III. The Influence of Gravitationally Induced Angular Momentum Transport on Disk Structure and Appearance, *Astrophysical Journal*, **525**, pp. 330–342, (1999).

210 A space Fresnel Imager for Ultra-Violet Astrophysics: example on accretion disks

List of Figures

List of Tables

Bibliography

[1] Gary L. Brian D. Mason, *The washington double star catalog*, `http://ad.usno.navy.mil/wds/`, October 2008.

[2] Kennent C., *The age of procyon*, Cambridge University Press, 2005.

[3] Serre Denis, *L'imageur interrférométrique de fresnel: un instrument spatial pour l'observation á haute résolution angulaire*, Ph.D. thesis, Université Paul Sabatiere, 2007.

[4] C. P. Dullemond, M. E. van den Ancker, B. Acke, and R. van Boekel, *Explaining UX Orionis Star Variability with Self-shadowed Disks*, The Astrophysical Journal **594** (2003), L47–L50.

[5] Dean Faklis and George Michael Morris, *Broadband imaging with holographic lenses*, Optical Engineering **28** (1989), no. 6, 592–598.

[6] C. Hayashi, *Equilibria and dynamics of isothermal clouds*, Star Forming Regions (M. Peimbert & J. Jugaku, ed.), IAU Symposium, vol. 115, 1987, pp. 403–416.

[7] Chushiro Hayashi, *Structure of the solar neb 'ula, growth and decay of magnetic fields and effects of magnetic and turbulent viscosities on the nebula*, in IAU Symp. 93: Fundamental Problems in the Theory of Stellar Evolution **70** (1981), 35–53.

[8] Henyey and Greenstein, *Diffuse radiation in the galaxy*, The Astrophysical Journal,The American Astronomical Society **93** (1941), 70–83.

[9] F. Hersant, B. Dubrulle, and J.-M. Huré, *Turbulence in circumstellar disks*, Astronomy & Astrophysics **429** (2005), 531–542.

[10] D. Koechlin, L. Serre and P. Duchon, *High resolution imaging with fresnel interferometric arrays: suitability for exoplanet detection*, Astronomy & Astrophysics **443** (2005), 709–720.

[11] Laurent Koechlin, Jean-Pierre Rivet, Paul Deba, and Truswin Raksasataya, *Generation 2 testbed of fresnel imager: First results on the sky*, Experimental Astronomy: Special Issue (2010), 0–0.

[12] I.V. Minin and O.V Minin, *Fresnel zone plate lens and antennas for millimeter waves: history and evolutions of developments and applications*, Infrared and Millimeter Waves, 2000. Conference Digest. 2000 25th International Conference, 2000, pp. 409–410.

[13] F. Bouchy P. Eggenberger, F.Carrier and A. Blecha, *Solar-like oscillations in procyon a*, Astronomy & Astrophysics **1** (2005), no. 2, 247–252.

[14] José-Philippe Pérez, *Optique: fondements et applications*, Sciences Sup, Dunod, 2004.

[15] S. Richling and H. W. Yorke, *Photoevaporation of Protostellar Disks. V. Circumstellar Disks under the Influence of Both Extreme-Ultraviolet and Far-Ultraviolet Radiation*, The Astrophysical Journal **539** (2000), 258–272.

[16] Jr Robert Burnham, *Chandra x-ray observatory: Orbit of sirius a and b*, `http://chandra.harvard.edu/photo/2000/0065/more.html`, January 2000.

[17] M. Sekiya, *Quasi-Equilibrium Density Distributions of Small Dust Aggregations in the Solar Nebula*, Icarus, International Journal of Solar System Studies **133** (1998), 298–309.

[18] D. Serre, P. Deba, and L. Koechlin, *Fresnel interferometric arrays for space-based imaging: testbed results*, UV/Optical/IR Space Telescopes: Innovative Technologies and Concepts III, in Proceedings of the SPIE. (Howard A. MacEwen and James B. Breckinridge, eds.), Presented at the Society of Photo-Optical Instrumentation Engineers (SPIE) Conference, vol. 6687, September 2007, p. 66870I.

[19] D. Serre, P. Deba, and L. Koechlin, *Fresnel interferometric imager: ground-based prototype*, Applied Optics **48** (2009), 2811–2820.

[20] Denis Serre, *Design and numerical tests of a blazed diverging fresnel zone lens for an interferometric imager: optimal surface and optical efficiency*, Experimental Astronomy **submitted** (2007), ??

[21] Denis Serre and Laurent Koechlin, *Fresnel interferometric arrays: principle and exploitation*, EAS Publications Series, EAS Publications Series, vol. 22, 2006, pp. 253–260.

[22] J. L. Soret, *Sur les phénomènes de diffraction produits par les réseaux circulaires*, Archives des Sciences physiques et naturelles **52** (1875), 320–337.

[23] Henry B. Throop, *Evidence for dust grain growth in young circumstellar disks*, Science **292** (2001), no. 2, 1686–1989.

[24] Isaac W. Ward, *Satellite of procyon*, Nature **55** (1896), 153–153.

AUTHOR : Truswin RAKSASATAYA

TITLE : The Fresnel Diffractive Array Imager : Ground-based Validation and Space Applications

SUPERVISOR : Laurent KOECHLIN

DEFENDED : 20 December 2010, at the Observatoire Midi-Pyrénées, France

---

Abstract

The Fresnel Array is a diffractive focalization instrument developed to be applied for space observation in astrophysics. It implies long-focal length focusing, thus, formation flying in space. During my thesis, the concept has been tested with ground-based prototypes and validated by measuring the image quality and instruments functionalities.

Since 2007, a second generation Fresnel Diffractive imager prototype has been built, and operates on a 18 meter long refractor tube. 200x200 mm square Fresnel arrays have been constructed, tested with ground-based observation of astrophysical targets, and upgraded to demonstrate that they meet the quality for space applications at large array size : 4m. Observations are made in Nice since June 2009. They prove that the concept is working in real conditions, The collected data and the consequent images demonstrate the functionality and quality of Fresnel diffractive Imager.

The first part of this thesis introduces the principle of Fresnel diffractive Imaging and its design. The specifications of the components in the system present the nominal performance. The second part describes the tests made to validate the instrument concept and demonstrate the high dynamic range imaging, the observation results, and the optimization of the ground-based prototype. The last part proposes a space mission, providing the space observations configurations. A target such as an accretion disc around a young star is shown as a study case for a Fresnel space mission with 20x20 meter arrays, opening new domains of astrophysics in the ultra violet.

KEYWORDS : High angular resolution, high contrast imaging, ground-based, interferometric device, diffractive focusing, wavefront propagation, achromatism, Fresnel zones, Point Spread Function, accretion disc detection, IV observation.

Laboratoire d'Astrophysique de Toulouse et Tarbes - UMR 5572
Observatoire Midi-Pyrénées
14 Avenue Edouard Belin
31400 Toulouse - FRANCE

AUTEUR : Truswin RAKSASATAYA

TITRE : L'Imageur diffractif de Fresnel : Validation le ciel depuis le sol et l'observation spatial pour à Haute Résolution Angulaire

DIRECTEUR DE THESE : Laurent KOECHLIN

DATE ET LIEU DE SOUTENANCE : 20 Decembre 2010, à l'Observatoire Midi-Pyrénées (France)

Résumé

L'imageur de Fresnel est un instrument focalisation diffractive qui est développé pour l'observation astrophysique depuis l'espace. Il est a longue focale, et de ce fait requiert le vol en formation. Pendant ma thèse, le concept a été étudié avec des prototypes au sol et validé en mesurant la qualité des images obtenues et les fonctionnalités de l'instrument. Depuis 2007, un prototype diffractif d'imageur de Fresnel de génération 2 a été conu, il a été mis au point en 2009, et fonctionne en parallèle sur un tube de lunette long de 18 mètres. Plusieurs grilles de Fresnel carrées de 200x200 mm ont été construites, testées au sol par l'observation de cibles astrophysiques, et améliorées pour tendre vers la qualité requise pour des applications depuis l'espace avec des grilles grande taille 4m ou plus. Des observations sont faites à Nice depuis juin 2009 avec un prototype de 200x200 mm d'ouverture, et 18 m de focale. Elles montrent que le concept fonctionne en conditions réelles. Les données acquises et les images obtenues démontrent la fonctionnalité et la qualité de cet imageur de Fresnel.

La première partie de la thèse présente le principe de focalisation diffractive utilisé dans l'imageur de Fresnel, la formation des images, et le détail de sa conception : les caractéristiques des différents composants optiques du système et leurs performances nominales. La deuxième partie décrit les essais faits pour valider le concept et pour démontrer la formation des images à haute dynamique, les résultats d'observations, et l'optimisation du prototype au sol. La troisième et dernière partie propose une mission spatiale, et sa configuration pour l'observation depuis l'espace. Une cible telle qu'un disque d'accrétion autour d'une étoile jeune est prise comme cas d'étude pour la mission spatiale d'un imageur de Fresnel avec une ouverture de 20×20 m, ouvrant de nouveaux domaines de l'astrophysique dans l'ultraviolet.

MOTS-CLEFS : Haute résolution angulaire, haute dynamique, , interférométrie, , achromatisation, zones de Fresnel, prototype sol, fonction d'étalement du point, détection d'exoplanètes.

DISCIPLINE ADMINISTRATIVE : Astrophysique - Instrumentation

Laboratoire d'Astrophysique de Toulouse et Tarbes - UMR 5572
Observatoire Midi-Pyrénées
14 Avenue Edouard Belin
31400 Toulouse - FRANCE